Coupled Spins in Diamond: From Quantum Control to Metrology and Many-Body Physics

A dissertation presented

by

Georg Kucsko

to

The Department of Physics

in partial fulfillment of the requirements

for the degree of

Doctor of Philosophy

in the subject of

Physics

Harvard University

Cambridge, Massachusetts

April 2016

Dissertation Advisor: Author

Professor Mikhail D. Lukin **Georg Kucsko**

Coupled Spins in Diamond:
From Quantum Control to Metrology and Many-Body Physics

Abstract

The study of quantum mechanics, together with the ability to coherently control and manipulate quantum systems in the lab has led to a myriad of discoveries and real world applications. In this thesis we present experiments demonstrating precise control of an individual long-lived spin qubit as well as sensing applications for biology and investigation of quantum many-body dynamics.

Stable quantum bits, capable both of storing quantum information for macroscopic time scales and of integration inside small portable devices, are an essential building block for an array of potential applications. In the second chapter of this thesis we demonstrate high-fidelity control of a solid-state qubit, which preserves its polarization for several minutes and features coherence lifetimes exceeding 1 second at room temperature.

Sensitive probing of temperature variations on nanometer scales is an outstanding challenge in many areas of modern science and technology. In chapter three we show how nitrogen vacancy centers in diamond can be used as a robust, high sensitivity temperature probe. We furthermore demonstrate biological compatibility by introducing nano-sized diamonds into living cells and measuring externally induced sub-cellular temperature gradients.

Abstract

Understanding the dynamics of interacting many-body quantum systems with on-site potential disorder has proven one of the biggest challenges in quantum physics to investigate both in theory and experiment. In chapter four we demonstrate how coherent control techniques can be utilized to probe the many-body dynamics of a strongly interacting NV spin ensemble. Specifically, we show how a long-range interacting dipolar spin system exhibits characteristically slow thermalization in the presence of tunable disorder.

The presented works offer up many new areas to investigate, including complex quantum many-body effects of large, disordered spin systems, as well as applications of NV centers as bio-compatible nano-scale temperature probes.

Contents

Citations to Previously Published Work

With minor modifications Chapter 2 and Appendix B have been published in the main text and the supplementary information of

> P. C. Maurer*, G. Kucsko*, C. Latta, L. Jiang, N. Yao, S. Bennett, F. Pastawski, D. Hunger, N. Chisholm, M. Markham, D. Twitchen, I. Cirac, M. D. Lukin, *Room-temperature quantum bit memory exceeding one second*, Science **336**, 1283 to 1286 (2012)

With minor modifications Chapter 3 and Appendix C have been published in the main text and the supplementary information of

> G. Kucsko*, P. C. Maurer*, N. Yao, M. Kubo, H. J. Noh, P. Lo, H. Park, M. D. Lukin, *Nanometre-scale thermometry in a living cell*, Nature **500**, 54 to 58 (2013)

* These authors contributed equally to this work.

Acknowledgments

First and foremost I would like to thank my advisor Mikhail Lukin. I first met Misha at a conference in Switzerland while working on a master's degree from ETH zurich. My professor at the time, Atac Imamoglu was kind enough to introduce me to his colleague Misha. I approached Misha with the intent of conducting my thesis research under his guidance in the growing and exciting field of NV centers. Misha quickly agreed and soon after, I started working in his group. After a few months of promising results he suggested applying for graduate school at Harvard. Knowing what would await me in Misha's group it was an easy decision to make. During my years in graduate school, Misha's constant guidance, great scientific intuition and innovative ideas are the reason for some of the best years of my life.

I would also like to thank many of Misha's colleagues for all the years of successful collaboration. Specifially the contributions of Ronald Walsworth, Hongkun Park, Amir Yacoby, Aravinthan Samuel, Fedor Jelezko, Ignacio Cirac, Eugene Demler, Dirk Englund and Paola Cappellaro. I would also like to thank my dissertation committee consisting of Mikhail Lukin, Hongkun Park and Amir Yacoby who provided guidance and encouragement along the way.

During my research work, Misha paired me with some of the brightest and most capable scientists I ever had the pleasure of collaborating with. Peter Maurer, my closest colleague for the first 5 years of my PHD, not only taught me most things I know about NV centers, but was also a great source of scientific inspiration. His numerous ideas and broad scientific knowledge led to work that was not only scientifically strong, but also highly instructive and a lot of fun.

I was later able to pass on much of that knowledge to junior graduate student Joonhee

Choi. We spent countless hours on measurements as well as intriguing discussions about physics and animal photography.

Soonwon Choi tirelessly worked on the background theory for our thermalization experiment and taught me more about quantum mechanics within a year than i was ever able to teach myself.

I would also like to note long time theory collaborator Norman Yao, and thank him for many long nights of paper crafting and legacy software management.

My thanks also extends to all past and present members of the Lukin group for many productive and fun years in our lab. Specifically I would like to point out the experimental and theoretical contributions of Steven Bennett, Jeronimo Maze, Alexander Zibrov, Nathalie de Leon, Peter Rabl, Brendan Shields, Alp Sipahigil, Michael Goldman, Ruffin Evans, Igor Lovchinsky, Alexander Sushkov, Kristiaan De Greve, Emre Togan, Yiwen Chu, Shimon Kolkowitz, Jeff Thompson, Alexander Kubanek, Tobias Tiecke, Hannes Bernien, Manuel Endres, Arthur Safira, Quirin Unterreithmeier, Elana Urbach, Alexei Bylinskii, Alexander Keesling-Contreras, Bo Dwyer, Aaron Kabcenell, Jan Gieseler, Peter Komar, Janos Perczel, Manuel Endres, Christian Nguyen, Denis Sukachev, Crystal Senko, Dominik Wild, Leo Zhou, Polnop Samutraphoot, Mihir Bhaskar, Harry Levine, David Levonian, Trond Andersen and Javier Sanchez-Yamagishi.

Moreover I gained a lot of help and experimental assistance from my colleagues Nicholas Chisholm, Christian Latta and David Hunger as well as theoretical help from Sarang Gopalakrishnan and Michael Knap.

Particularly important to the success of this thesis were also Mikey Shulman and Shannon Harvey from the Yacoby group for their restless ninja wirebonding and high end coffee

making skills.

I would also like to mention Erik Bauch, Linh Pham and all other members of the Walsworth group, who over the years not only contributed to countless discussions but were also a reliable and helpful source for equipment sharing.

During our work on the thermometry project, we were heavily dependent on the skillfull and reliable sample preparation and nanodiamond injection skills of Minako Kubo and Peggy Lo from Hongkun Park's group. Currently, a similar role is filled by Ni Ji from Aravinthan Samuel's lab, whose meticulous preparation of C. elegans samples, and nanodiamond injection skills are unparalleled.

For our work on the high density thermalization experiment I would like to point out the contributions of long time collaborator Fedor Jelezko for countless discussions as well as Junichi Isoya for producing one of the most interesting pieces of diamond in the world.

I would also like to thank our collaborators from Element Six for providing us with the best and cleanest diamond samples in existence, specifically the efforts of Matthew Markham and Daniel Twitchen.

Over my years at Harvard I also had the pleasure of working with a highly skillful and always friendly and helpful body of staff. Specifically life would have been impossible without the engineering prowess of Jim MacArthur, the technical expertise of Michele Waters, the enduring patience of Silke Exner, the kindness of Lisa Cacciabaudo, the efficiency of Adam Ackerman and the incredible cappuccinos from Robert Amaral.

Most of our experiments would also not have been possible without the organizational skills and help provided by our group admins over the years; Joan Hamilton, Karl Coleman and Clare Ploucha.

My immense gratitude also extends to all of my friends and the residents of castle 354, whose constant support and encouragement spurred me on throughout my degree. In particular I would like to mention my girlfriend Camille who taught me more about biology than I could have ever hoped to learn and without whom I would still struggle with the proper use of a pipette.

Last and most importantly I would like to thank my mother Gabriele, my father Guido and my sister Stefanie, who not only encouraged my interest in science since I was a little boy, but also supported and motivated me during all my years of graduate school.

To my Family

Gabriele, Guido & Stefanie Kucsko

"I think I can safely say that nobody understands quantum mechanics."

Richard Feynman

Chapter 1

Introduction

1.1 Background

Over the last century the study of quantum mechanics has led to a myriad of new discoveries and important innovations. The fundamental notion that nature operates in discrete quanta of energy that can exhibit both particle and wave-like behavior was first introduced around 1900 [1]. Famously, the correct explanation of black body radiation as well as the description of the photoelectric effect, spurred increased interest in this novel theory. By the 1920s, the ground breaking scientific work of Max Planck, Werner Heisenberg, Albert Einstein, Erwin Schrdinger, Louis de Broglie and many others led to a wide adoption of quantum physics as an integral part of our understanding of nature. Due to the fragile nature of quantum mechanical wavefunctions however, controlling quantum systems of large size still remains highly challenging to this day. To leverage the power of high sensitivity quantum sensing or solve exponentially hard problem through quantum computation, it is therefore necessary to engineer a well isolated quantum system, and gain a high de-

gree of coherent control. Over the years, many promising approaches have been developed to fulfill these criteria, such as trapped ions, cold atoms in a lattice and solid-state spin defects [2, 3, 4]. Each of which with their own set of advantages and disadvantages.

1.1.1 Isolated Quantum Systems

The main challenge to obtaining a long-lived, coherent quantum bit is posed by an ever present incoherent environment, consisting of fluctuating magnetic and electric fields, optical photons or temperature fluctuations. To achieve a high degree of isolation from such an environment, scientists are forced to build intricate experimental setups meant to provide interaction free environments. By utilizing technical innovations such as high vacuum and laser-cooling, trapped ions achieve a remarkable degree of isolation, while retaining good addressability and controllability [5]. Similarly, artificial atoms, such as superconducting qubits in combination with cooling close to absolute zero have demonstrated our ability to engineer powerful quantum systems [6]. Another particularly fascinating approach is presented by atomic defects in a solid state environment. Due to their natural isolation from the environment within the lattice, defects such as phosphorus in silicon or nitrogen-vacancy centers in diamond can exhibit long coherence times and a high degree of control even at room temperature, without a vacuum environment [7, 8, 9].

1.1.2 Controlled Environment Coupling: Quantum Sensing

While usually we aim to suppress the coupling of a well controlled quantum system to an incoherent environment, it can sometimes be exploited. In certain solid-state spin qubits for example, the environment mainly consists of magnetic noise due to other spin

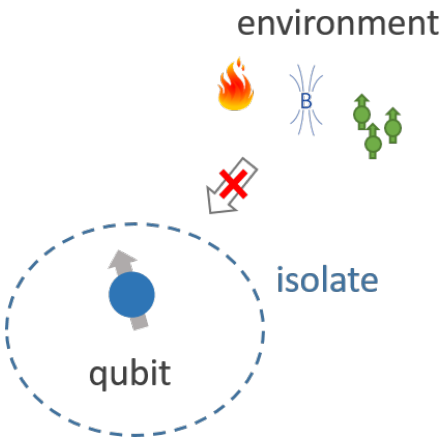

Figure 1.1: To observe the quantum dynamics of a single qubit, it is necessary to isolate it from all environmental influences such as temperature and magnetic field fluctuations.

impurities, the effects of lattice strain and temperature induced lattice expansion. Through the use of coherent control techniques it is possible to engineer the Hamiltonian of the system to selectively couple to a single quantity of interest, such as temperature induced energy shift, while retaining a high degree of isolation from the rest of the environment. Such thermometry techniques strongly benefit from the high sensitivity of quantum based measurment techniques [10]. Over the past decades quantum assisted metrology has moved from proof of principle experiments to actively used techniques that strongly outperform their classical counterparts [11, 12, 13, 14].

1.1.3 Many-Body Quantum Dynamics

Over the past decades our increased capabilities in isolating quantum systems has enabled us to study coherent interactions among qubits. By eliminating environmentally induced decoherence but retaining interactions among qubits, coherent entangled states can be created. Applications for large entangled quantum states range from powerful compu-

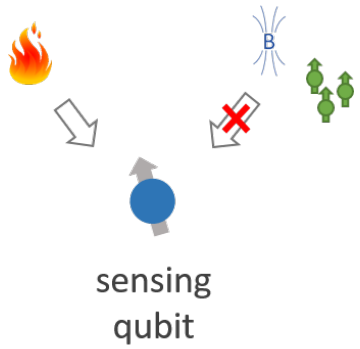

Figure 1.2: By utilizing a carefully chosen set of basis states or particular dynamical decoupling techniques it is possible to probe environmental effects such as temperature while still remaining insensitive to others such as magnetic field fluctuations.

tation and quantum simulation to high sensitivity squeezed states for metrology. Realizing large quantum systems however is highly challenging. Significant progress in scaling system size has been demonstrated by ion-traps as well as superconducting qubits. While these systems are well controlled, they so far remain limited to $\leq$20 qubits. Due to the exponential growth in Hilbert space however, even larger systems ($>10^2$) are not only hard to achieve experimentally, but it is also difficult to predict their dynamics. Their description is particularly challenging in the presence of on-site energy disorder and long-range interactions. Recent efforts have utilized large ensembles of spins in nuclear magnetic resonance (NMR) experiments to study such long-range many-body dynamics in 3-d [15]. While nuclear spins can be well controlled and exhibit long lifetime, they lack a method of efficient state preparation. Other solid-state systems, such as nitrogen-vacancy centers in diamond, not only offer a similar degree of control but additionally provide the ability to locally polarize as well as read out the spin state by optical means. This could make such solid-systems an attractive platform to study many-body dynamics in a disordered, long-range interacting, 3-d spin system.

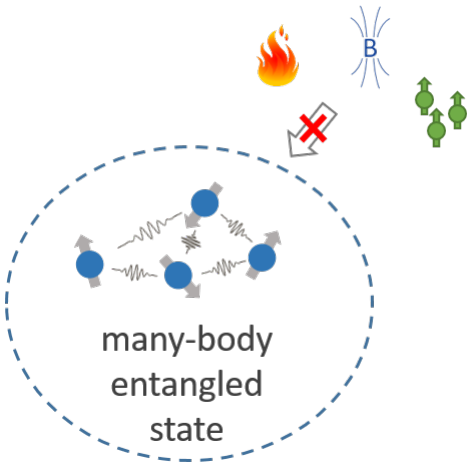

Figure 1.3: In order to study quantum many-body dynamics it is necessary that interactions between qubits dominate over environmentally induced decoherence. To that effect, coherent decoupling techniques can be utilized to suppress decoherence, but leave the interaction Hamiltonian intact.

1.2 Nitrogen Vacancy Centers in Diamond

Over recent years, diamond has established itself as one of the front runners for probing quantum phenomena and realizing real world applications. Due to its large band gap it provides an ideal host material for several point defects with numerous optical as well as spin degrees of freedom. In this thesis we will focus on one of the most successful candidates for quantum information and sensing, the nitrogen vacancy color center in diamond.

1.2.1 Optical Properties

The NV center is a solid state spin defect in diamond, consisting of a substitutional nitrogen atom as well as an adjacent vacant lattice site (Fig. 1.4). It possesses many advantageous properties such ease of addressability and initialization via an optical degree of freedom as well as long spin lifetime and room temperature operation.

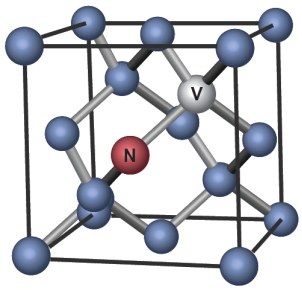

Figure 1.4: The nitrogen vacancy center in diamond consists of a substitutional nitrogen atom and an adjacent vacant lattice site.

In general, NV centers can occur in either a neutral (NV^0) or negatively charged (NV^-) electronic state [16]. Unless otherwise noted, most of the physics presented in this dissertation focuses on the NV^- charge state. Its electronic ground state and its first excited state both lie within the band gap of diamond, allowing optical addessability. The transition between these two states is dipole allowed and can be excited under green illumination, with subsequent emission between 637 nm and 800 nm [17, 18]. Confocal fluorescence microscopy therefore allows detecting and addressing individual NVs within a bulk piece of diamond.

1.2.2 Spin Structure

The optical ground state of NV^- consists of a spin triplet with the $|m_s = 0\rangle$ and $|m_s = \pm 1\rangle$ spin projections split by a zero-field splitting, $\Delta = (2\pi) \times 2.87$ GHz created by spin-spin interactions [17, 18]. The $|m_s = \pm 1\rangle$ states can further be Zeeman-split by applying an external magnetic field to provide effective two-level systems.

While optical excitation from the $|m_s = 0\rangle$ state is mostly spin preserving, excitation from $|m_s = \pm 1\rangle$ has a finite branching ratio into a metastable singlet state with a lifetime of

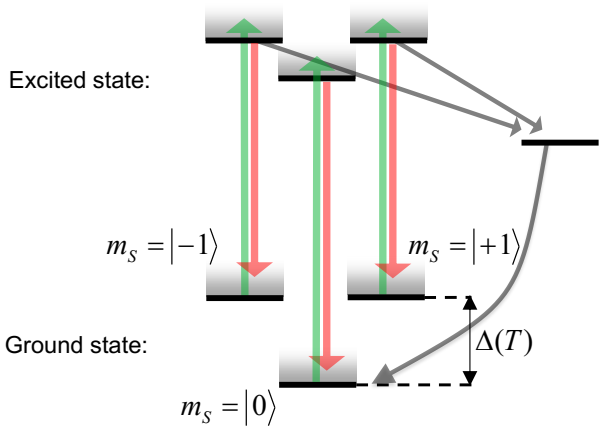

Figure 1.5: Simplified level scheme for the NV^- defect. Green arrows indicate optical excitation via a 532 nm laser. Red arrows represent spin conserving fluorescence, while the grey arrows depict (non-radiative) shelving into the metastable singlet state as well as decay back down to $|m_s = 0\rangle$.

$\approx$ 300 ns. This singlet state decays non-radiatively into $|m_s = 0\rangle$ allowing for an efficient initialization of the electronic spin. The long lifetime of the singlet state also enables optical readout of the spin state since the $|m_s = \pm 1\rangle$ states are prevented from scattering photons while residing in the singlet state and will therfore appear darker [17, 18]. The coherent manipulation of all electronic spin states can be achieved via resonant microwave radiation. At room temperature, the typical lifetime is limited by phonon relaxation to $\sim$4 ms [19] For diamond samples with a low concentration of paramagnetic impurities, the coherence times of the electronic spin can be up to a few milli-seconds long [7].

1.2.3 Historical Overview

Historically, nitrogen vacancy centers in diamond were first discovered in the 1970s [20]. It wasn't until much later however that EPR as well as optical techniques led to the proper

definition of the energy levels, allowing for coherent manipulation and establishing the NV as a powerful candidate to probe quantum phenomena. Due to the fragile nature of quantum bits, most realizations such as trapped ions or superconducting qubits require complex and expensive equipment to observe quantum behavior. The NV center in diamond however is naturally protected by the surrounding lattice, can be observed and controlled trough well established and widely used laser and microwave equipment and allows the observation of quantum phenomena even at room temperature.

Studying the NV center in diamond has resulted in many important achievements in the field of quantum information, such as room-temperature single-shot readout [21], coupling of an NV to multiple long-lived nuclear spins to form a local spin register [22, 23] as well as spin photon entanglement [24] leading to long range entanglement between two NV centers separated by over a kilometer [25, 26]. Additionally, NV centers are finding applications in quantum metrology, demonstrating high sensitivity magnetic field sensing [27], nanoscale NMR spectroscopy [28, 29], electric field sensing [30] and nanoscale temperature sensing [14].

1.3 Overview of Thesis

Following the introductory chapter, this dissertation is organized into three main parts covering three scientific projects; achieving a long-lived memory, building a nanoscale temperature sensor and studying thermalization of interacting spins in the presence of tunable disorder. Chapter 5 then summarizes the achieved results and provides an outlook on currently ongoing experiments. Additional supporting information can be found in the appendix. All experiments in this thesis unless otherwise noted were performed at room

temperature.

1.3.1 Building a Quantum Memory Bit

The first project in this thesis, discussed in Chapter 2 focuses on the room temperature implementation of a long lived single spin quantum memory. By utilizing the NV as a well-understood control qubit, it is possible to initialize and control a single, weakly coupled ^{13}C nuclear spin. Such a system provides a robust and high fidelity solid-state quantum memory for over a second.

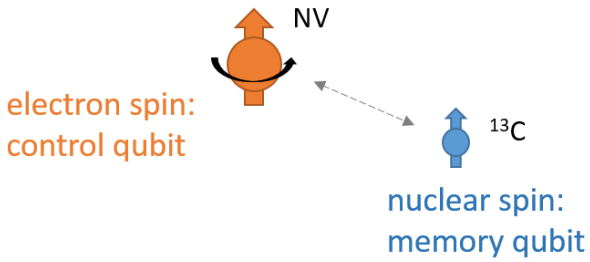

Figure 1.6: Single NV center coupled to a close-by nuclear spin. The NV acts as a highly controllable interface to utilize the otherwise hard to manipulate, long lived nuclear spin.

1.3.2 Temperature Sensing with Diamond Impurities

In the second part (Chapter 3) we demonstrate how NV centers can be used as a high sensitivity nanoscale temperature sensor. Through careful calibration and the use of coherent decoupling techniques it becomes possible to sensitively detect changes in local temperature, while decoupling from external sources of noise, such as magnetic field fluctuations produced by nearby spin impurities. By utilizing bio-compatible nano-sized diamonds and introducing them into living biological cells, we measure externally induced sub cellular

temperature gradients with high sensitivity and robustness, providing a tool for studying heat dependent biological processes on the nanoscale.

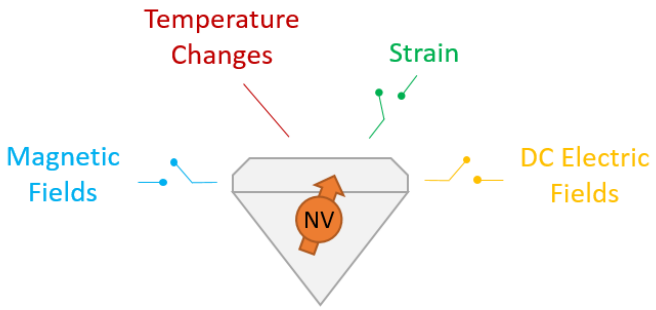

Figure 1.7: NV centers in diamond can be manipulated in a way that they are decoupled from influences such magnetic fields or strain, while remaining sensitive to temperature changes.

1.3.3 Slow Thermalization Spin Dynamics

In Chapter 4 we present how the coherent control techniques we have developed to manipulate NV centers lead us to the study of a strongly interacting ensemble of spins. Specifically we study the thermalization behavior of two long-range interacting, oppositely polarized ensembles of NVs in the presence of disorder. We demonstrate how the system exhibits characteristically slow thermalization, with a strong dependence on tunable effective on-site energy disorder.

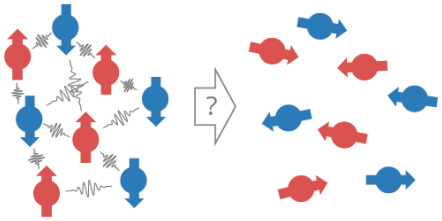

Figure 1.8: Two groups of oppositely polarized spins, subject to random on-site potential shifts are coupled via long-range dipolar interaction. Due to disorder such a system exhibits sub-diffusive, slow relaxation to reach thermal equilibrium.

"My job is to protect you."

Batman

Chapter 2

Room-Temperature Quantum Bit Memory Exceeding One Second

2.1 Motivation

Stable quantum bits, capable of both storing quantum information for macroscopic timescales and of integration inside small, portable devices, represent an essential building block for an array of potential applications. We demonstrate high fidelity readout of a solid-state qubit, which preserves its polarization for several minutes and features coherence lifetimes exceeding one second at room temperature. The qubit consists of a single ^{13}C nuclear spin in the vicinity of a Nitrogen-Vacancy (NV) color center within an isotopically purified diamond crystal. The long qubit memory time is achieved via a novel technique involving dissipative decoupling of the single nuclear spin from its local environment. The versatility, robustness and potential scalability of this system may allow for new applications in quantum information science.

2.2 Background

Many applications in quantum communication [31] and quantum computation [4] rely upon the ability to maintain qubit coherence for extended periods of time. Furthermore, integrating such quantum mechanical systems in compact, mobile devices remains an outstanding experimental task. While trapped ions and atoms [32] can exhibit coherence times as long as minutes, they typically require a complex infrastructure involving laser-cooling and ultra-high vacuum. Other systems, most notably ensembles of electronic and nuclear spins, have also achieved long coherence times in bulk ESR and NMR experiments [33, 34, 8]; however, owing to their exceptional isolation, individual preparation, addressing and high fidelity measurement remains challenging, even at cryogenic temperatures [35].

2.3 Method

Our approach is based upon an individual nuclear spin in at room-temperature solid. A nearby electronic spin is used to initialize the nuclear spin [22, 36, 21] in a well defined state and to read it out in a single shot [21] with high fidelity. A combination of laser illumination and RF decoupling pulse sequences [33, 37] enables the extension of our qubit memory lifetime by nearly three orders of magnitude. This approach decouples the nuclear qubit from both the nearby electronic spin and other nuclear spins, demonstrating that dissipative decoupling can be a robust and effective tool for protecting coherence in various quantum information systems [4, 38, 39].

2.4 Experimental System

Our experiments utilize an individual NV center and a single ^{13}C ($I = 1/2$) nuclear spin (Fig. 2.1) in a diamond crystal. We work with an isotopically pure diamond sample, grown using Chemical Vapor Deposition from isotopically enriched carbon consisting of 99.99% spinless ^{12}C isotope. In such a sample, the optically detected electron spin resonance (ESR) associated with a single NV center is only weakly perturbed by ^{13}C nuclear spins, resulting in long electronic spin coherence times [7]. This allows us to make use of a Ramsey pulse sequence to detect a weakly coupled single nuclear spin, separated from the NV by 1-2 nanometers. The coupling strength at such a distance is sufficient to prepare and measure the nuclear spin qubit with high fidelity. For the present concentration of ^{13}C nuclei, about 10% of all NV centers exhibit a coupled nuclear spin with a separation of this order.

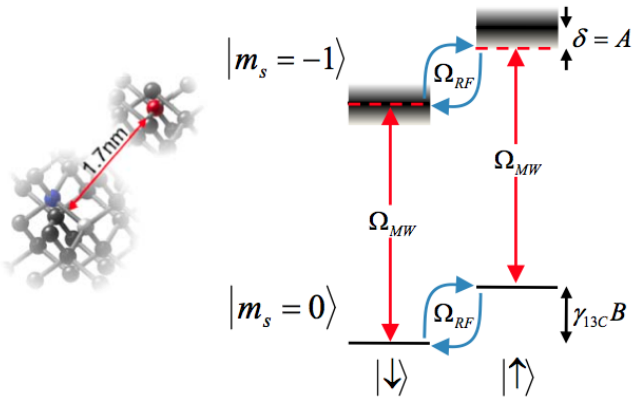

Figure 2.1: The NV center with a proximal ^{13}C spin can be modeled as a simple four-level system to understand readout dynamics. Nuclear spin sublevels $|\uparrow\rangle$ and $|\downarrow\rangle$ are split by a Zeeman shift ($\gamma_{13C}B$) and addressed via RF radiation with Rabi frequency Ω_{RF}. The electronic transition $|0\rangle \rightarrow |-1\rangle$ (red arrows) can be simultaneously driven by a microwave field with relative detuning given by the hyperfine coupling strength, $A = \sqrt{A_{\parallel}^2 + A_{\perp}^2}$.

2.5 Detecting individual Nuclear Spins

In our experimental setup, the diamond sample is magnetically shielded from external perturbations, and a static magnetic field $B = (244.42 \pm 0.02)$ G is applied along the NV symmetry axis. The spin transition between the $|0\rangle \rightarrow |-1\rangle$ electronic spin states is addressed via microwave radiation (see Appendix B). Figure 2.2 shows the free electron precession of an individual NV center, measured via a Ramsey sequence. The signal dephases on a time scale of $T_{2e}^{*} = (470 \pm 100)\mu s$ consistent with the given isotopic purity of the sample [7]. The characteristic collapses and revivals of the Ramsey signal correspond to the signature of a single weakly coupled ^{13}C nuclear spin. This coupling strength, originating from a hyperfine interaction, corresponds to an electron-nuclear separation of roughly 1.7 nm (see Appendix B).

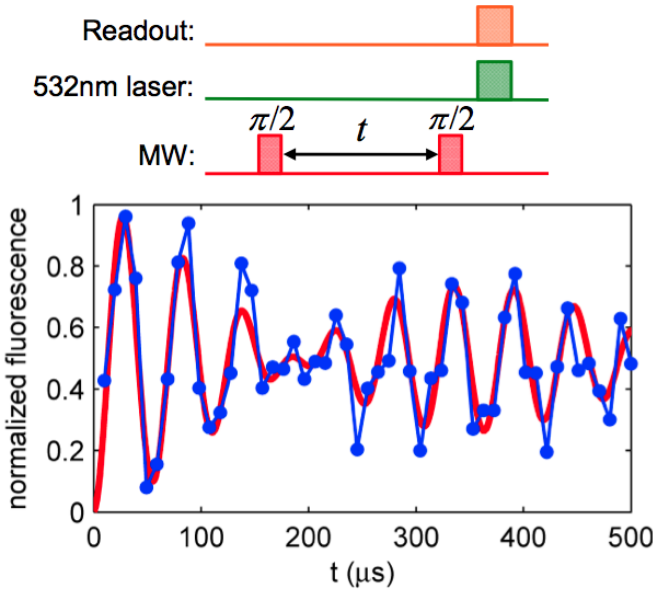

Figure 2.2: An electron Ramsey measurement as a function of free evolution time (t), depicts beating due to the different hyperfine transitions and a $T_{2e}^{*} = (470 \pm 100)$ μs.

To confirm that the signal originates from a ^{13}C nuclear spin, we measure the probability of a RF-induced nuclear spin-flip as a function of carrier frequency, ω. As described below, we prepare the nuclear spin in either the $|\downarrow\rangle$ or $|\uparrow\rangle$-state by performing a projective measurement. After preparation of the nuclear spin via projection a 1.25 ms Gaussian shaped RF π-pulse is applied. A second step of nuclear measurement then allows the nuclear spin-flip to be determined. Figure 2.3 shows that this probability is characterized by three resonances located at $\omega/(2\pi) = 258.86, 261.52, 264.18$ kHz, corresponding to the NV electronic spin being in $m_s = 1, 0, -1$ respectively; this indicates a projected hyperfine interaction, $A_{\|} = (2\pi)\,(2.66 \pm 0.08)$ kHz.

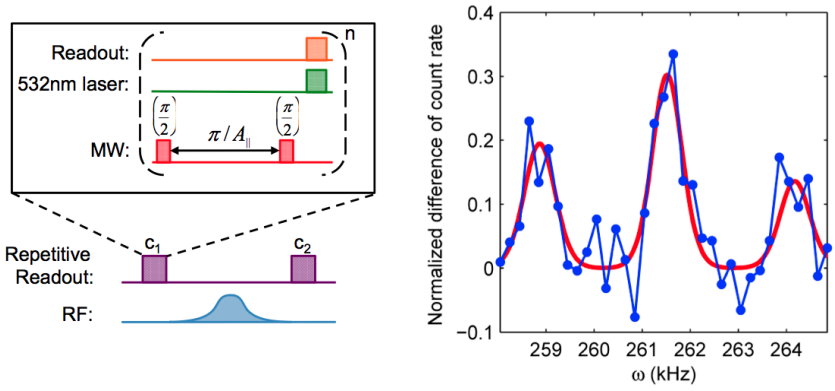

Figure 2.3: NMR spectra of ^{13}C, obtained via the depicted pulse sequence, demonstrate three different nuclear transitions corresponding to electronic spin states $m_s = 0, \pm 1$. The pulse sequence contains a blue Gaussian RF pulse and two repetitive readouts (purple), c_1 and c_2.

2.6 Memory Spin Initialization and Readout

An important facet of quantum control involves the ability to perform high fidelity initialization and readout. We use repetitive readout to achieve single shot detection of

the nuclear spin state. In this approach (Fig. 2.4) the electronic spin is first polarized into the $|0\rangle$ state. Next, a $C_n NOT_e$ logic gate (electronic spin-flip conditioned on the nuclear spin) is performed and the resulting state of the electronic spin is optically detected; this sequence is repeated multiple times to improve the readout fidelity. The required quantum logic is achieved via a Ramsey sequence on the electronic spin, where the free precession time is chosen to be $\tau = \pi/A_{\|}$.

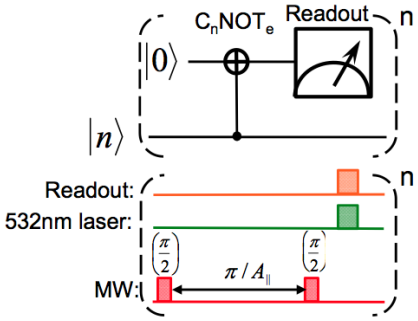

Figure 2.4: Circuit diagram of repetitive readout of the nuclear spin $|n\rangle$. The readout uses a $C_n NOT_e$ gate consisting of multiple repetitions of an electronic spin Ramsey and subsequent repolarization.

Figure 2.5 depicts an example trace of the accumulated fluorescence of 20000 readout repetitions per data point. The resulting signal clearly switches between two distinct values, which correspond to the two states of the spin-$\frac{1}{2}$ ^{13}C nuclear spin. We associate high (low) count rates with the $|\uparrow(\downarrow)\rangle$ states of the nuclear spin, noting that these do not necessarily correspond to alignment/anti-alignment with the external field (see Appendix B). This time trace indicates that the nuclear spin preserves its orientation, on average, for about half a minute.

To achieve high fidelity initialization of the nuclear spin, we post-select repetitive readout measurements that are below (above) a threshold corresponding to 147 (195) counts

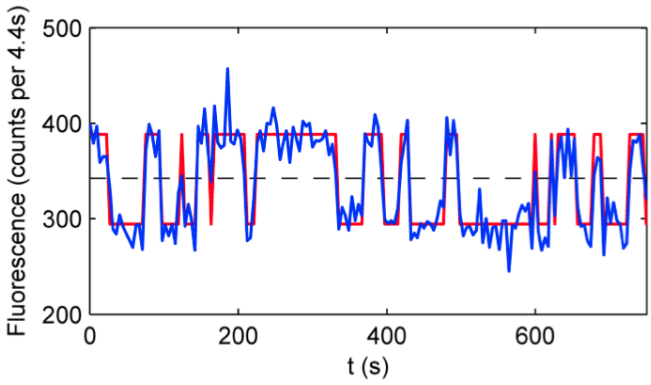

Figure 2.5: Fluorescence time trace showing single shot readout of the nuclear spin and corresponding quantum jumps. The integration time for a single point is 4.4 s.

per 2.2 s. This allows us to prepare the nuclear spin state with > 97 % fidelity (see Appendix B). After successful initialization via projection, a second repetitive readout measurement is performed. This allows us to extract readout count statistics dependent on the nuclear spin state. As shown in Fig. 2.6, the two distributions for the count rates of $|\uparrow\rangle$ and $|\downarrow\rangle$ are clearly resolved and their medians match the high and low levels of the fluorescence trace in Fig. 2.5. From the overlap between the two distributions, we obtain a projective readout fidelity of (91.9 ± 2.5) % [40].

2.7 Nuclear Depolatization Dynamics

The long spin orientation lifetime, extracted from Fig. 2.5, implies that our ^{13}C nuclear spin is an exceptionally robust degree of freedom. To quantify the nuclear depolarization rate, the T_{1n} time was measured as a function of laser intensity. In the dark, no decay was observed on a timescale of 200 s (see Appendix B). However, consistent with predictions from a spin-fluctuator model[41, 42], when illuminated with a weak optical field, T_{1n} drops

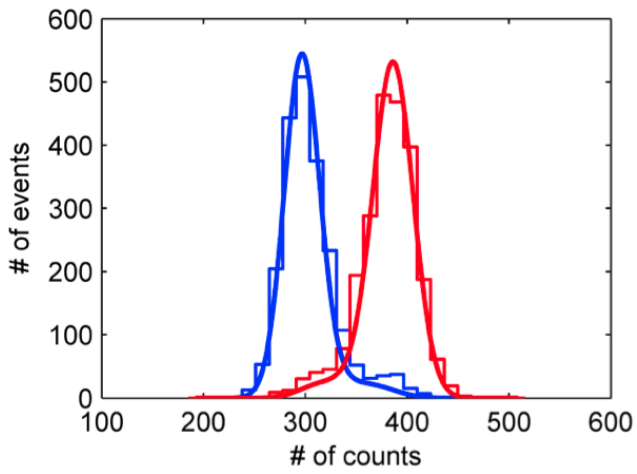

Figure 2.6: Histogram of continuous repetitive readouts (per 4.4 s) showing two overlapping distributions of nuclear spin states: $|\downarrow\rangle$ (blue) and $|\uparrow\rangle$ (red), see Appendix B.

to (1.7 ± 0.5) s and increases linearly for higher laser intensities (Fig. 2.7).

2.8 Quantum Memory Coherence Extension

To probe the qubit's coherence time, our nuclear spin is again prepared via a projective measurement, after which, an NMR Ramsey pulse sequence is applied. The final state of the nuclear spin is then detected via repetitive readout. The results (Fig. 2.8) demonstrate that, in the dark, the nuclear coherence time T_{2n}^{*} is limited to about (8.2 ± 1.3) ms. The origin of this relatively fast dephasing time can be understood by noting its direct correspondence with the population lifetime of the electronic spin $T_{1e} = (7.5 \pm 0.8)$ ms (blue curve Fig. 2.8) [43]. Because the electron-nuclear coupling $A_{\parallel}$ exceeds $1/T_{1e}$, a single (random) flip of the electronic spin (from $|0\rangle$ to $|\pm 1\rangle$) is sufficient to dephase the nuclear spin.

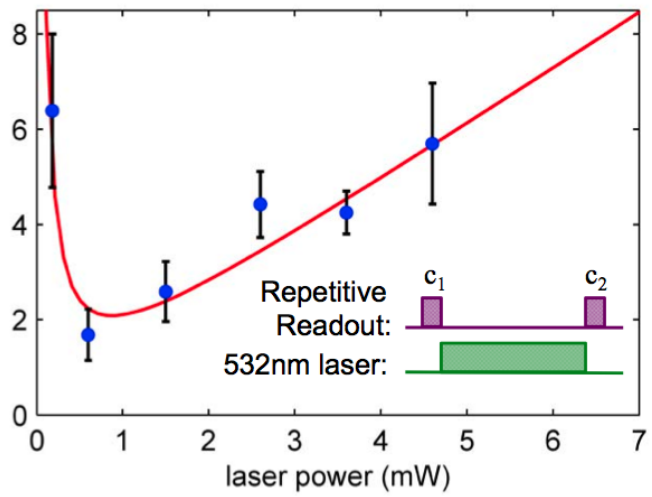

Figure 2.7: Nuclear spin orientation lifetime, T_{1n} (error bars are one standard deviation), as a function of laser power in the presence of illumination by a 532 nm laser. As shown in the inset, each data point is extracted from a series of two repetitive readout sequences. The solid red curve represents the theoretical prediction from the simple model of nuclear depolarization induced by the off-axis dipolar hyperfine field.

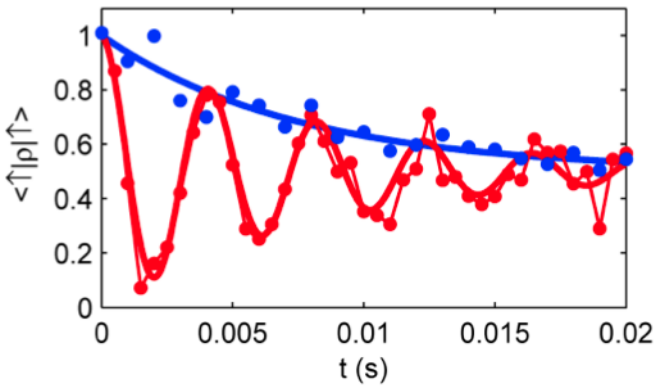

Figure 2.8: Nuclear Ramsey experiment (red curve) depicting a dephasing time $T_{2n}^{*} = (8.2 \pm 1.3)$ ms. The origin of this dephasing is the depolarization of the electronic spin (blue curve), with $T_{1e} = (7.5 \pm 0.8)$ ms.

To extend the nuclear memory time, we must effectively decouple the electronic and nuclear spin during the storage interval. This is achieved by subjecting the electronic spin to controlled dissipation. Specifically, the NV center is excited by a focused green laser beam, resulting in optical pumping of the NV center out of the magnetic states ($|\pm 1\rangle$). In addition, the NV center also undergoes rapid ionization and deionization at a rate γ, proportional to the laser intensity. When these transition rates exceed the hyperfine coupling strength, the interaction between the nuclear and electronic spin is strongly suppressed owing to a phenomenon analogous to motional averaging [42].

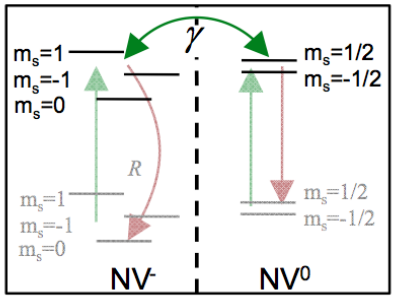

Figure 2.9: Model for repolarization and ionization dynamics. In the NV^- charge state, the electronic spin can be pumped via green illumination to $m_s = 0$ at a rate R.

Using this decoupling scheme, we show in Fig. 2.10 that the nuclear coherence time can be enhanced by simply applying green laser light; in particular, 10 mW of green laser excitation, yield an extended nuclear coherence time of $T_{2n}^* = (0.53 \pm 0.14)$ s. An improvement of T_{2n}^* by almost two orders of magnitude compared with measurements in the dark. The dependence of T_{2n}^* on green laser intensity shows a linear increase for low intensities and saturates around one second (Fig. 2.12, red points).

The observed limitation of coherence enhancement arises from dipole-dipole interactions of the nuclear qubit with other ^{13}C nuclei in the environment. In our sample, we

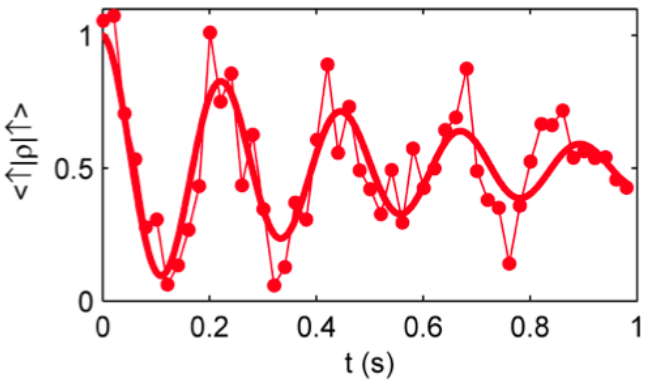

Figure 2.10: Nuclear Ramsey experiment with concurrent green illumination, showing $T_{2n}^{*} = (0.53 \pm 0.14)$ s.

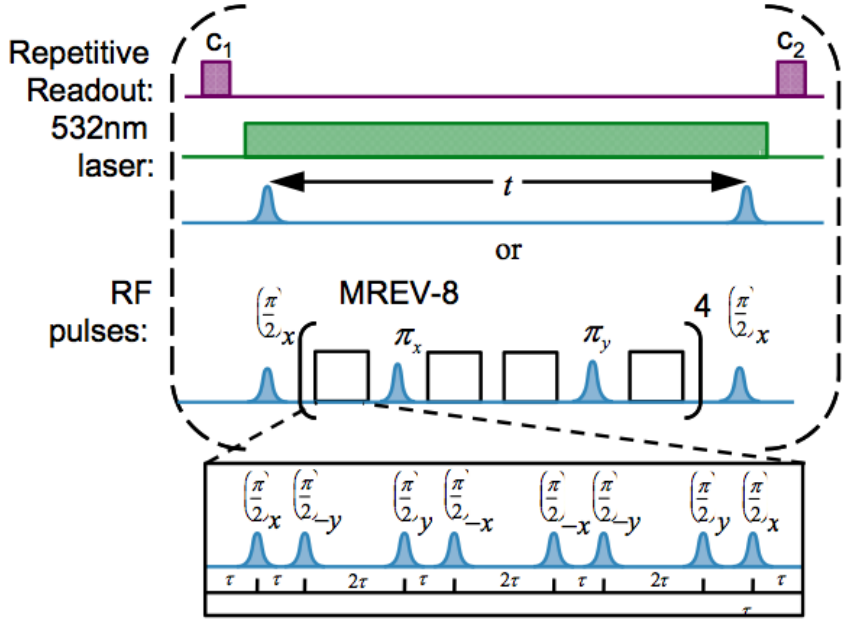

Figure 2.11: Experimental sequence used to measure the nuclear coherence time. A modified Mansfield Rhim Elleman Vaughan (MREV) decoupling sequence [33] is utilized. It consists of 16 MREV-8 pulse trains interwoven with 8 phase-refocusing π-pulses. Each MREV-8 pulse sequence can be achieved through $\pi/2$ rotations around four different axes.

estimate this average dipole-dipole interaction to be ~ 1 Hz, consistent with the observed coherence time. Further improvement of the nuclear coherence is achieved via a homonuclear RF-decoupling sequence. The composite sequence (Fig. 2.11) is designed to both average out the inter-nuclear dipole-dipole interactions (to first order) and to compensate for magnetic field drifts. Applying this decoupling sequence in combination with green excitation can further extend the coherence time to beyond one second (Fig. 2.12, blue points).

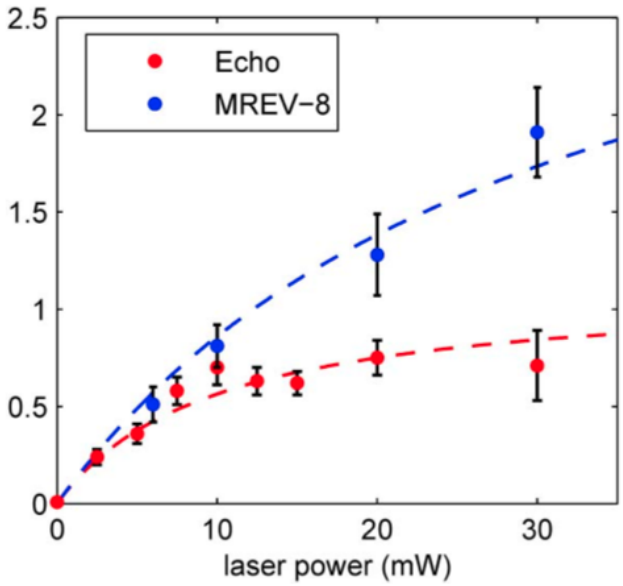

Figure 2.12: Nuclear coherence as a function of green laser power. Red data constitute a measurement of T_{2n} using a nuclear spin echo; blue data T_{2n} contain the additional MREV sequence. The dashed fits are calculated from the spin-fluctuator model (see Appendix B).

2.9 Fidelity and Tomography Results

These measurements demonstrate that individual nuclear spins in isotopically pure diamond represent an exceptional candidate for long-lived memory qubits. The qubit memory performance is fully quantified by two additional measurements. First, the average fidelity is determined by preparing and measuring the qubit along three orthogonal directions. This fidelity, $\bar{F} = \frac{1}{2}(1 + \langle C \rangle)$, is extracted from the observed contrast (C) of the Ramsey signal and is presented in Fig. 2.13 for two cases (with and without homonuclear decoupling) [22]. Even for memory times up to (2.11 ± 0.3) s, the fidelity remains above the classical limit of $^2/_3$.

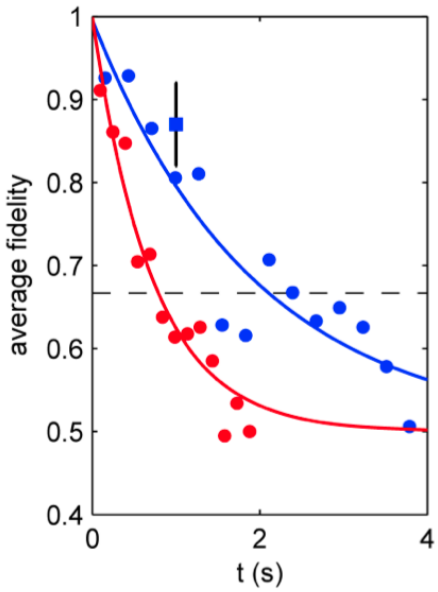

Figure 2.13: Average fidelity as a function of time obtained from states prepared along $|x\rangle = \frac{1}{\sqrt{2}}(|\downarrow\rangle + |\uparrow\rangle)$, $|y\rangle = \frac{1}{\sqrt{2}}(|\downarrow\rangle + i|\uparrow\rangle)$ and $|z\rangle = |\downarrow\rangle$. The nuclear echo (red curve) is obtained at 10 mW of green power while the MREV sequence (blue curve) is obtained at 30 mW of green power. The square data point represents the fidelity extracted from process tomography.

Finally, a full characterization of our memory (at one second of storage time) is obtained via quantum process tomography. The corresponding χ-matrix (Fig. 2.14) reveals an average fidelity of $\bar{F} = (87 \pm 5)$ % (see Appendix B).

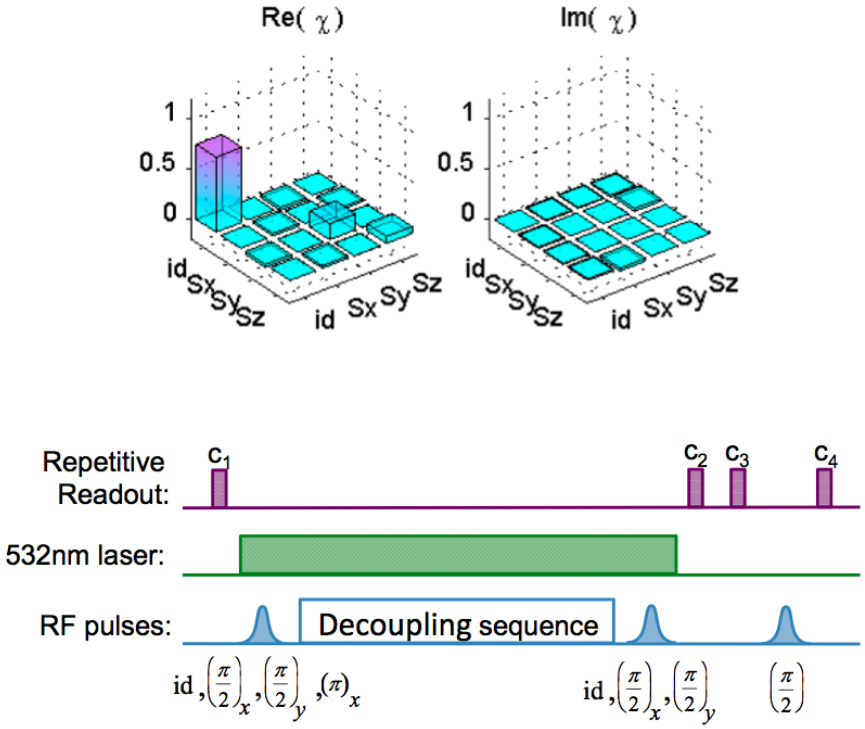

Figure 2.14: The χ matrix of the full quantum process tomography at one second of storage time with 30 mW of continuous green illumination (see Appendix B) and pulse sequence depicting the initialization of four different nuclear states and three subsequent rotations.

To quantitatively understand the coherence extension under green illumination, we consider depolarization and dephasing of the nuclear spin due to optical illumination and interaction with the nuclear spin environment. Excitation with 532 nm (de)ionizes the NV center with a rate proportional to the laser intensity[44]. Adding up the peak probabilities (Fig. 2.3) for the nuclear RF transitions reveals a total transition probability of (63 ± 5) %.

This is consistent with recent observations, where, under strong green illumination, the NV center is found to spend 30 % of its time in an ionized state [44]. In this state, RF induced nuclear transitions are suppressed since the depolarization rate of the electronic spin is much faster than the nuclear Rabi frequency [44]. Because the hyperfine interaction is much smaller than the electronic Zeemann splitting, flip-flop interactions between the electronic and nuclear spin can be neglected. However, in the presence of an off-axis dipolar hyperfine field $A_\perp$, nuclear depolarization still occurs at a rate ${}^1/_{T_{1n}} \sim \frac{A_\perp^2}{(\gamma_{13_C}B/2)^2+(\gamma)^2}\gamma$ (see Appendix B). While this simple analysis is already in good agreement with our observations (Fig. 2.7), further insight is provided by a detailed 11-level model of NV dynamics (see Appendix B). As T_{1n} limits our readout, a careful alignment of the external field (i.e. choosing $A_\perp \to 0$) and enhanced collection efficiency should enable readout fidelities greater than 99%.

For (de)ionization rates γ much larger than the hyperfine interaction, the dephasing rate depends on the parallel component of the dipole field, ${}^1/_{T_{2n}^*} = \Gamma_{opt} + \Gamma_{dd}$, where Γ_{dd} is the spin-bath induced dephasing rate and $\Gamma_{opt} \sim \frac{A_\parallel^2}{\gamma}$ is the optically induced decoherence. The dashed red line in Figure 2.12 demonstrates that this model is in good agreement with our data. Application of our decoupling sequence also allows us to suppress nuclear-nuclear dephasing. We find that the main imperfection in this decoupling procedure originates from a finite RF detuning (see Appendix B). Accounting for this imperfection, we find excellent agreement with our data, as shown by the dashed blue line in Figure 2.12. Moreover, this model indicates that the coherence time increases almost linearly as a function of applied laser intensity, suggesting a large potential for improvement.

2.10 Outlook and Conclusion

The use of even higher laser intensities is limited by heating of the diamond sample, which causes drifts in the ESR transition [45]. However, this can be overcome via a combination of temperature control and careful transition-frequency tracking, yielding an order of magnitude improvement in the coherence time to approximately one minute. Further improvement can be achieved by decreasing the hyperfine and the nuclear-nuclear interaction strength through a reduction of the ^{13}C concentration, potentially resulting in hour-long storage times (see Appendix B). Finally, it is possible to use coherent decoupling sequences and techniques based upon optimal control theory [46], which scale more favorably than our current dissipation-based method. With such techniques, we estimate that the memory lifetime can approach the timescale of phonon-induced nuclear depolarization, measured to exceed $T_{1n}^{max} \sim 36$ h [47].

As a future application of our techniques the realization of fraud resistant quantum tokens can be considered. Here, secure bits of information are encoded into long-lived quantum memories. Along with a classical serial number, an array of such memories, may possible constitutes a unique unforgeable token [48, 49]. With a further enhancement of storage times, such tokens may potentially be used as quantum-protected credit cards or as quantum identification cards [49] with absolute security. Furthermore, NV-based quantum registers can take advantage of the nuclear spin for storage, while utilizing the electronic spin for quantum gates and readout [22, 36]. In particular, recent progress in the deterministic creation of arrays of NV centers [50] and NV-C pairs [51], enables the exploration of scalable architectures [52, 53]. Finally, recent experiments have also demonstrated the entanglement of a photon with the electronic spin-state of an NV center [24]. Combining

the advantages of an ultra-long nuclear quantum memory with the possibility of photonic entanglement opens up novel routes to long-distance quantum communication and solid state quantum repeaters [31].

"Rising temperatures are a planetary emergency

and a threat to the survival of our civilization."

Al Gore

Chapter 3

Nanometer Scale Thermometry in a Living Cell

3.1 Introduction

Sensitive probing of temperature variations on nanometer scales represents an outstanding challenge in many areas of modern science and technology [54]. In particular, a thermometer capable of sub-degree temperature resolution as well as integration within a living system could provide a powerful new tool for many areas of biological research, including temperature-induced control of gene expression [55, 56, 57, 58] and cell-selective treatment of disease [59, 60, 61]. Here, we demonstrate a new approach to nanoscale thermometry that utilizes coherent manipulation of the electronic spin associated with nitrogen-vacancy (NV) color centers in diamond. We show the ability to detect temperature variations down to 1.8 mK (sensitivity of 9 mK$/\sqrt{\text{Hz}}$) in an ultra-pure bulk diamond sample. Using NV centers in diamond nanocrystals (nanodiamonds), we directly measure the local thermal en-

vironment at length scales down to 200 nm. Finally, by introducing both nanodiamonds and gold nanoparticles into a single human embryonic fibroblast, we demonstrate temperature-gradient control and mapping at the sub-cellular level, enabling unique potential applications in life sciences.

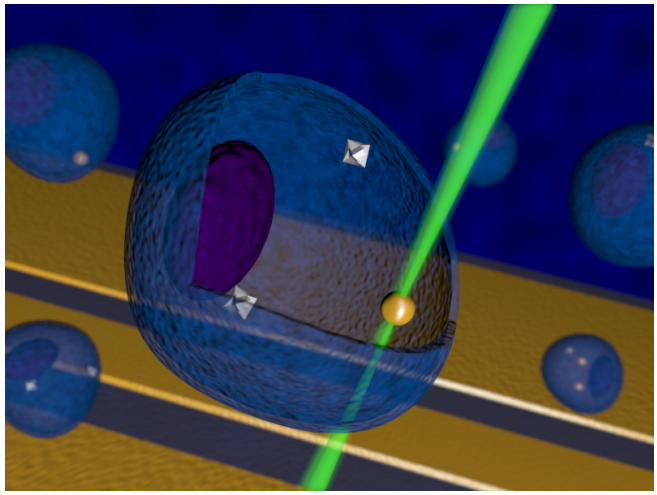

Figure 3.1: Schematic image depicting nanodiamonds and gold nanoparticles (Au NPs) within a living cell. The controlled application of local heat is achieved via laser illumination of the Au NP, while nanoscale thermometry is achieved via precision spectroscopy of the NV spins in nanodiamonds.

3.2 Motivation

The ability to monitor sub-kelvin variations over a large range of temperatures can provide insight into both organic and inorganic systems, shedding light on questions ranging from tumor metabolism [62] to heat dissipation in integrated circuits [54]. Moreover, by combining local light-induced heat sources with sensitive nanoscale thermometry, it may be possible to engineer biological processes at the sub-cellular level. Many promising

approaches are currently being explored for this purpose, including scanning probe microscopy [54, 63], Raman spectroscopy [64], and fluorescence-based measurements using nanoparticles [65, 66] and organic dyes [67, 68]. These methods, however, are often limited by a combination of low sensitivity, bio-incompatibility, or systematic errors owing to changes in the local chemical environment (Fig. 3.2).

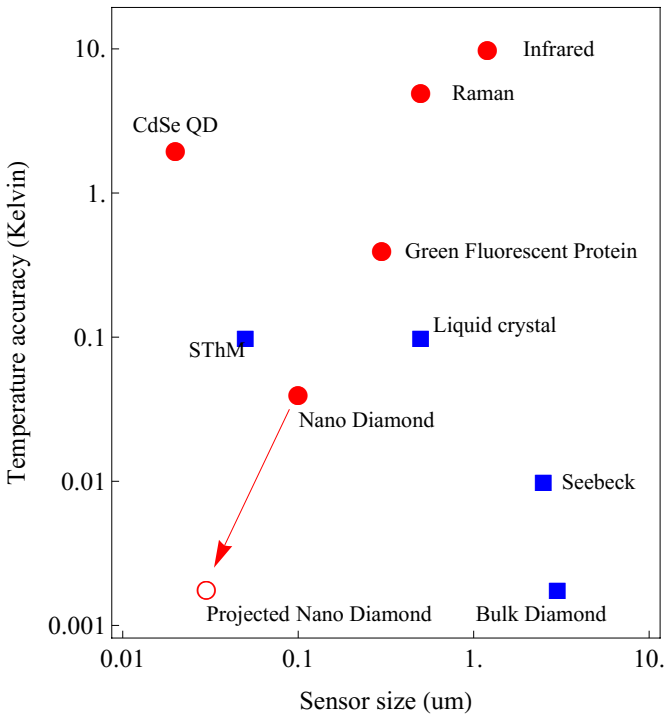

Figure 3.2: Comparison between the NV quantum thermometer and other reported techniques as a function of sensor size and temperature accuracy. Red circles indicate methods that are biologically compatible. The red open circle indicates the ultimate expected accuracy for our measurement technique in solution (see Appendix C).

3.3 Experimental Approach

Our new approach to nanoscale thermometry utilizes the quantum mechanical spin associated with nitrogen vacancy (NV) color centers in diamond. The operational principle of NV-based thermometry relies upon the temperature dependent lattice strain of diamond [69]; changes in the lattice are directly reflected as changes in the spin properties of the NV, which are then optically detected with high spatial resolution.

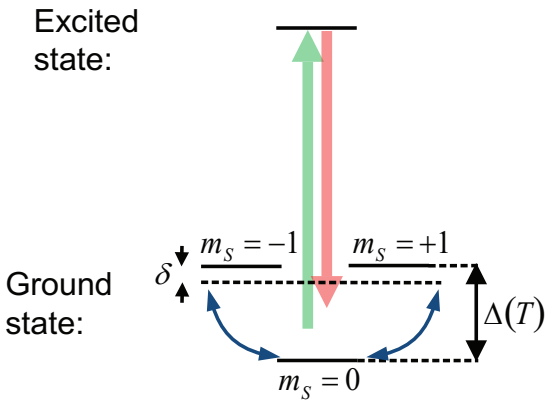

Figure 3.3: Simplified NV level diagram showing a ground state spin triplet and an excited state. At zero magnetic field, the $|\pm 1\rangle$ sub-levels are split from the $|0\rangle$ state by a temperature-dependent zero field splitting $\Delta(T)$. Pulsed microwave radiation is applied (detuning δ) to perform Ramsey-type spectroscopy.

As illustrated in Fig. 3.3, each NV center constitutes a spin-1 degree of freedom with a zero-field splitting Δ between the $|m_s = 0\rangle$ and the $|m_s = \pm 1\rangle$ levels. This zero-field splitting exhibits a strong temperature dependence ($d\Delta/dT = -(2\pi)77$ kHz/K at 300 K), enabling fluorescence-based thermometry via precision electron spin resonance (ESR) spectroscopy [69, 70, 71]. For a sensor containing N color centers, the temperature

sensitivity is given by

$$\eta = \frac{C}{d\Delta/dT}\frac{1}{\sqrt{T_{\text{coh}}Nt}}, \tag{3.1}$$

where T_{coh} is the NV spin coherence time and t is the integration time. Here, we also introduce a factor C to account for imperfect readout and initialization [72]. Assuming T_{coh} on the order of few milliseconds and $C \approx 0.03$ [72], a single NV can potentially exhibit a sensitivity better than 1 mK$/\sqrt{\text{Hz}}$.

Beyond high sensitivity, NV-based thermometry offers several distinct advantages over existing methods in biological and chemical temperature sensing. First, owing to diamond's chemical inertness, it is generally robust to changes in the local chemical environment. Second, our method can be applied over a wide range of temperatures, $200-600$ K [70, 71].

3.4 Bulk Diamond Thermometry

As a first benchmarking experiment, we demonstrate the high temperature sensitivity of NV-based thermometry in a bulk diamond sample. While the NV's magnetic sensitivity has rendered it a competitive magnetometer [27, 73], to accurately determine the temperature, it is necessary to decouple the NV electronic spin from fluctuating external magnetic fields. This is achieved via a modified spin-echo sequence that makes use of the spin-1 nature of the NV defect [74], allowing us to eliminate the effects of an external, slowly varying, magnetic field. Specifically, we apply microwave pulse at frequency ω (Fig. 3.3) to create a coherent superposition, $\frac{1}{\sqrt{2}}(|0\rangle + |B\rangle)$, where $|B\rangle = \frac{1}{\sqrt{2}}(|+1\rangle + |-1\rangle)$. After half the total evolution time, τ, we apply a 2π echo-pulse that swaps the $|+1\rangle$ and $|-1\rangle$ states. Following another period of τ evolution, quasi-static (e.g. magnetic-field-induced) shifts of these $|\pm 1\rangle$ levels are eliminated, allowing for accurate temperature sensing.

In the experiment, we use a CVD-grown, isotopically pure diamond (99.99 % spinless ^{12}C isotope) sample [7] to further reduce magnetic-field fluctuations originating from the intrinsic ^{13}C nuclear spin bath. As shown in Fig. 3.4, this allows us to observe coherence fringes approaching 0.5 ms.

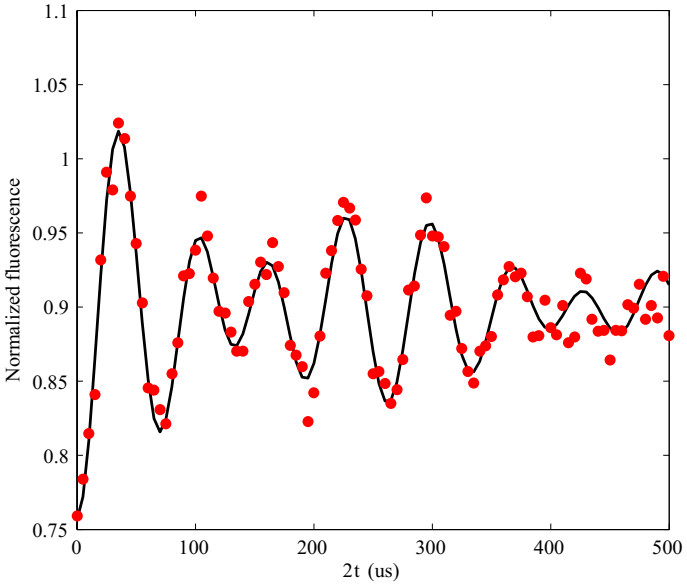

Figure 3.4: Measured fluorescence as a function of echo evolution time 2τ (red points); the black solid line indicates a fit corresponding to a damped cosine function with two distinct frequencies. The characteristic beating can be explained by fluctuating proximal charge traps located at distances of about 50 nm. The inset depicts the microwave 2π-echo-pulse sequence used to cancel unwanted external magnetic field fluctuations [74].

Interestingly, for all NVs tested, we observe a characteristic low-frequency beating of the fluorescence signal that varies from NV to NV, which is most likely due to locally fluctuating charge traps [30]. Despite this beating, we observe a temperature sensitivity $\eta = (9 \pm 1.8)$ mK$/\sqrt{\text{Hz}}$ by recording the signal for a fixed evolution time $\tau = 250$ μs (Fig. 3.5). Within 30-second integration, we achieve a measurement accuracy $\delta T = 1.8 \pm 0.3$ mK.

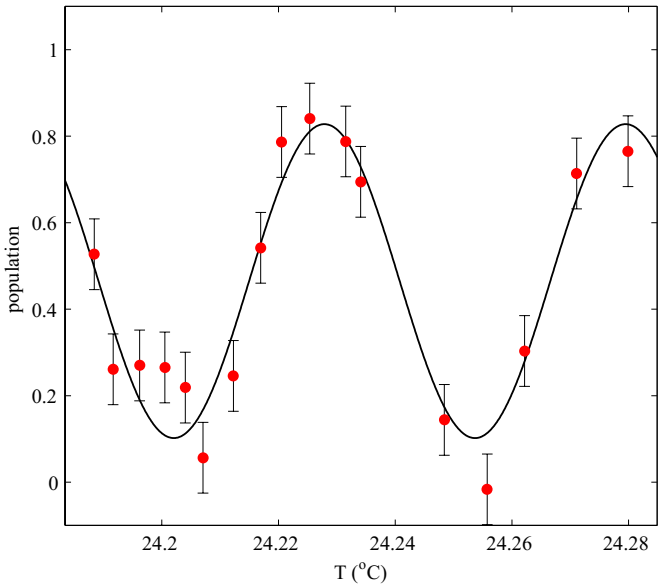

Figure 3.5: Measured fluorescence (red points), corresponding error bars (one standard deviation) and best fit line as function of temperature for an echo time $2\tau = 250$ μs.

3.5 Nanodiamond Thermometry

We now demonstrate the high spatial resolution of NV-based thermometry, which can be achieved by using diamond nanocrystals (nanodiamonds). In most commercially available nanodiamonds, the NV coherence time is limited to approximately 1 μs due to additional paramagnetic impurities. While this shortened coherence time reduces the intrinsic temperature sensitivity for a single defect, this decrease can be offset by using an ensemble of NVs to enhance the signal to noise ratio by a factor of $\sqrt{N}$. Note that unlike NV-based magnetometry, where the proximity to the source (often limited by nanodiamond size) is critical to the maximum sensitivity, NV thermometry is not subject to such a constraint; in fact, the excellent thermal conductivity of diamond ensures that *all* NV centers within a

nanocrystal are in thermal equilibrium with the local heat environment. To maximize the number of NV centers and to minimize the lattice strain, our measurements are performed on single-crystalline nanodiamonds containing approximately 500 NV centers (Adamas Nanotechnologies). The zero-field splitting Δ of the NV ensemble, and thus the temperature, is determined by recording a continuous-wave ESR spectrum. Specifically, we measure changes to the zero-field splitting by recording the fluorescence at four different frequencies centered around $\Delta = 2.87$ GHz (Fig. 3.6). This procedure eliminates unwanted effects from fluctuations in the total fluorescence rate, ESR contrast, Rabi frequency and magnetic field, yielding a robust thermometer (see Appendix C for details).

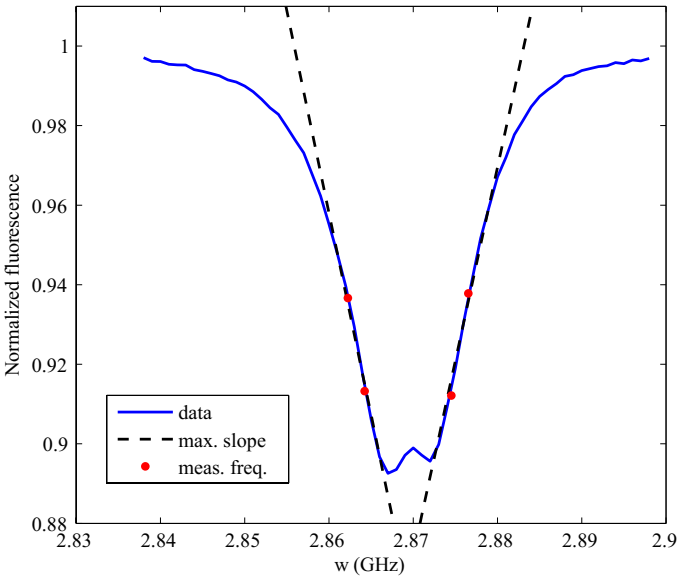

Figure 3.6: Frequency scan of a single nanodiamond containing approximately 500 NV centers. The four red points indicate the measurement frequencies used to extract the temperature as detailed in Appendix C.

Combining our nanodiamond thermometer with the laser heating of a gold nanoparticle

(Au NP) allows us to both control and monitor temperature at nanometer length scales.

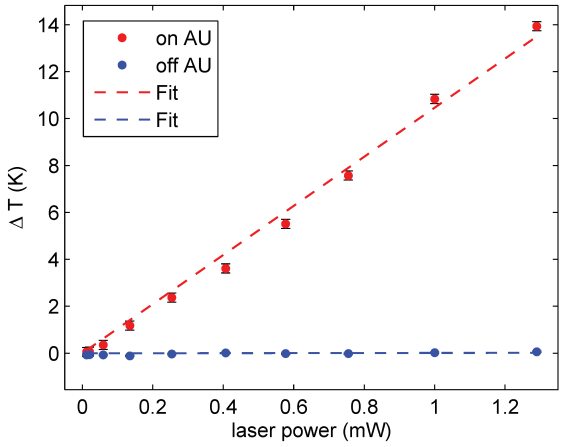

Figure 3.7: Temperature of a single nanodiamond as a function of laser power for two different laser-focus locations. The red data points depict the dramatic heating of a nanodiamond as a result of laser illumination on a nearby Au NP. The blue data points depict the same measurement with the laser focus displaced by 0.8 μm from the Au NP location; this results in the negligible heating of the nanodiamond as a function of laser power.

Both nanodiamonds and Au NPs (nominal diameter 100 nm) are initially spin-coated on a microscope coverslip. Using a home-built confocal microscope with two independent scanning beams, we co-localize an Au NP and a nanodiamond that are separated by 0.8 ± 0.1 μm. While locally heating the Au NP via continuous illumination with a variable-power green laser (focused to a diffraction limited spot), we also simultaneously measure the temperature at the nanodiamond location using ESR spectroscopy.

Figure 3.7 shows the temperature change recorded by the nanodiamond as a function of the green laser power (red points). From a linear fit to the data we estimate the accuracy of our ND sensor to be $\delta T = (44 \pm 10)$ mK (see Appendix C for details). The measured temperature change is in excellent agreement with the theoretically expected temperature

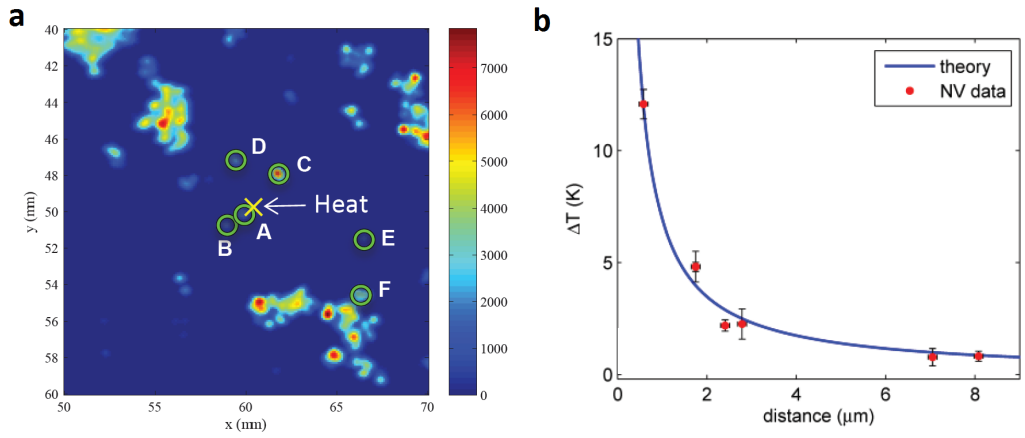

Figure 3.8: **(a)** Two-dimensional confocal scan of nanodiamonds (green circles) and Au NPs (yellow cross) spin-coated onto a glass coverslip. **(b)** Temperature changes measured (red points) at the six nanodiamond locations in (a) as a function of distance from the illuminated Au NP (yellow cross). The blue curve represents the theoretical temperature profile based upon a steady-state solution of the heat equation. All data in this figure are obtained on a glass coverslip, and all error bars correspond to one standard deviation.

profile based upon a steady-state solution of the heat equation, $\Delta T(r) = \frac{\dot{Q}}{4\pi\kappa r}$, where $\dot{Q}$ is the heat dissipation, κ is the thermal conductivity of glass and r is the distance between the nanodiamond and the Au NP. To further verify that the temperature change originates from the local heating of the Au NP, we repeat the measurement with the excitation laser displaced from the NP by 0.8 μm. In this case, the temperature measured by the nanodiamond remained constant as a function of laser power (blue points), thereby confirming the locality of the heat source. As shown in Figure 3.8a, we record the temperature of six nanodiamonds at different distances from the laser-heated Au NP; we find that the measured temperature profile (Fig. 3.8b) as a function of distance is in excellent agreement with the theoretical steady-state prediction (solid line). This allows us to directly estimate the temperature change at the location of the Au NP to be 72 ± 6 K.

3.6 Living Cell Thermometry

To demonstrate that nanodiamond thermometry is compatible inside living cells, we introduce nanodiamonds and Au NPs into human embryonic fibroblast WS1 cells via nanowire-assisted delivery [75, 76]. Just as in the control experiments described above, we probe the temperature at two different locations (NV_1 and NV_2) within a single cell while locally heating an individual Au NP (Fig. 3.9a).

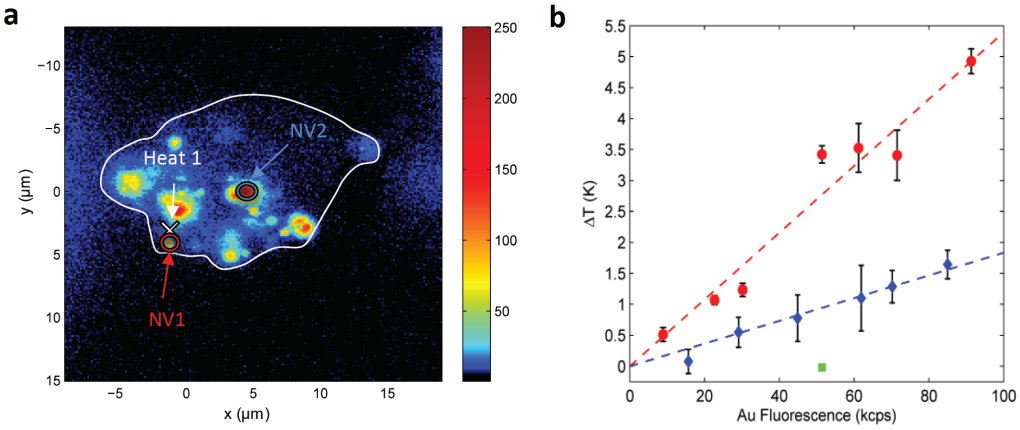

Figure 3.9: **(a)** Confocal scan of a single cell under 532 nm excitation with collection above 638 nm. The white cross corresponds to the position of the Au NP used for heating, while red (NV_1) and blue (NV_2) circles represent the location of nanodiamonds used for thermometry. The dotted white line provides a guide to the eye and outlines the cell membrane. **(b)** Measured change in temperature at the position of NV_1 and NV_2 relative to the incident laser power applied to the Au NP. Dashed lines are linear fits to the data, and error bars represent one standard deviation.

As shown in Fig. 3.9b, NV_1, which is significantly closer to the heat source, exhibits a stronger temperature dependence as a function of laser power than NV_2. Varying the incident power allows us to generate controlled temperature gradients of up to 5 K over distances of approximately 7 μm. To ensure that this temperature gradient is created by the controlled illumination of the NP and does not result from heating of the cellular cyto-

plasm, we displace the laser spot from the Au NP; this then results in a negligible temperature change at the location of NV_1 with $\Delta T = (-20 \pm 50)$ mK (green square, Fig. 3.9b). The increased measurement uncertainty for larger laser powers is the result of heating fluctuations from drift of the Au NP.

The experiments shown in Fig. 3.9b clearly demonstrate the sub-micron measurement of an intra-cellular heat gradient. However, the substantial heating induced by constant illumination for an extended period of time, ultimately leads to the death of the cell, which is confirmed using a standard live/dead assay (Calcein AM/Ethidium Homodimer-1). To demonstrate that our technique can be employed within living cells, we increase the concentration of Au NPs to allow for heat generation at different locations by simply moving the laser focus. Then, we measured the temperature variation at a single nanodiamond (bar plot in Fig. 3.10) while introducing a slight heating of Au NPs in two differing locations (red, yellow crosses). After our measurement, the viability of the cell is confirmed.

Finally, we demonstrate that our method can be used to control cell viability. To start, we heat the cell with 12 μW of laser power and measure a temperature change of 0.5 ± 0.2 K at the nanodiamond location; this corresponds to a change of approximately 10K at the Au NP spot. At this point, the cell is still alive, as confirmed by the absence of ethidium homodimer-1 fluorescence inside the membrane (Fig. 3.11).

By increasing the laser power to 120μW, we induce a temperature change of 3.9 ± 0.1K at the nanodiamond location (approximately 80K at the location of the laser focus); in this case, the cell is flooded with fluorescence from the ethidium homodimer, thus signaling cell death.

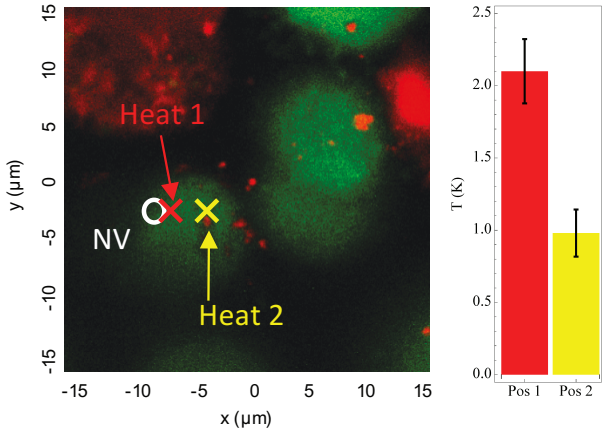

Figure 3.10: Fluorescence scan of stained cells (live/dead assay) with excitation at $494/528$ nm and emission at 515 nm (green - cell alive) and 617 nm (red - cell dead). The bar plot depicts the temperature of a single nanodiamond with local heat applied at two different locations (red/yellow cross).

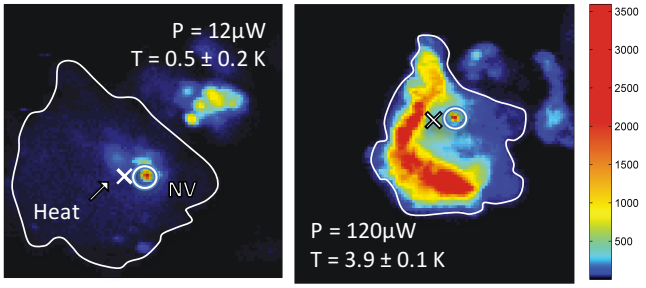

Figure 3.11: Confocal fluorescence scans of an individual cell under varying illumination power. Excitation occurs at 532 nm and collection is above 630 nm. Cell death is indicated by the penetration of ethidium homodimer-1 through the cell membrane, staining the nucleus. At low laser powers, the cell remains alive, while cell-death occurs as laser-induced heating is increased.

3.7 Outlook and Conclusion

This proof-of-principle experiment indicates that nanodiamond thermometry may help enable the optimization of NP-based photothermal therapies [77, 61].

Our experiments demonstrate that the quantum spin of NV centers in diamond can be used as a robust temperature sensor that combines the virtues of sub-micron spatial resolution, sub-degree thermal sensitivity and bio-compatibility. The sensitivity of our current measurement can be enhanced by improving the relevant coherence time and by increasing the number of NV centers within the nanocrystal. Optimizing these factors should allow us to reach sensitivities of $80\ \mu\mathrm{K}/\sqrt{\mathrm{Hz}}$ (see Appendix C), yielding the ability to sense sub-kelvin temperature variations with milli-second time resolution. In solution, the ultimate accuracy of our method will likely be limited by residual heating during the measurement process. As discussed in Appendix C, this limit is in the range of $50\ \mu$K to 5 mK, depending on experimental conditions. Furthermore, the spatial resolution of our method can be improved by using far-field sub-diffraction techniques [78].

NV-based thermometry opens up a number of intriguing potential applications. For instance, the simultaneous real-time measurement and control of a sub-cellular thermal gradient could enable the accurate control of gene expression [79]. The large dynamic range of our quantum thermometer and it's intrinsic robustness may also allow for the direct microscopic monitoring and control of chemical reactions [80]. Moreover, combining our technique with two-photon microscopy [81, 82] may enable *in vivo* identification of local tumor activity by mapping atypical thermogenesis at the single-cell level [83]. Finally the combination of thermoablative therapy with our temperature sensor constitutes a potent tool for the selective identification and killing of malignant cells without damaging surrounding tissue [59, 60, 61].

"One has to resort to the indignity of numerical simulations to settle even the simplest questions about it."

P. W. Anderson

Chapter 4

Slow Thermalization of a disordered dipolar Spin System in Diamond

4.1 Introduction

Nearly six decades ago, Anderson predicted that the interplay between transport and disorder in long-range-interacting quantum systems can lead to a novel regime of slow, sub-diffusive thermalization [84]. This is in stark contrast to the case of short-range interactions, where he showed that disorder can arrest dynamics, resulting in the breakdown of ergodicity. Termed localization, this effect has been observed in systems ranging from acoustic waves to cold atomic gases [85, 86, 87, 88, 89]; more recently, it has been shown that localization can persist even in strongly-interacting, isolated quantum systems, a phenomenon dubbed many-body localization [90, 91, 92, 93, 94]. The addition of long-range coupling tends to facilitate delocalization, leading to a regime where both localization and ergodicity compete [95]. This so-called critical regime is precisely realized by dipolar spins

in 3D, where a combination of power-law transport, dimensionality, and disorder govern the microscopic dynamics. Such criticality has been extensively explored in theory, but, as yet, not observed in experiment [84, 96, 97, 98, 99, 100, 101].

4.2 Experimental Approach

Our approach to the realization and study of critical dynamics makes use of disordered, strongly interacting spin impurities in diamond. In particular, we study cross-relaxation between two independently addressable and oppositely polarized electronic spin ensembles. We directly probe the spin decay dynamics and identify a regime of critical slow relaxation, where the time-dependence is characterized by a disorder dependent power law that is naturally explained by single-particle resonance counting. At late times, we find that relaxation accelerates and provide an explanation based upon a combination of open system dynamics and many-body interactions.

4.3 Sample Characteristics

The experimental system consists of a dense ensemble of nitrogen-vacancy (NV) centers in diamond (Fig. 4.1,4.2) under ambient conditions.

Each NV center constitutes a $S = 1$ electronic spin, which can be initialized, manipulated and optically read out. The spin projections $|m_s = \pm 1\rangle$, are separated from $|m_s = 0\rangle$ by a crystal field splitting, $\Delta_0 = (2\pi)\ 2.87$ GHz (Fig. 4.5).

An external magnetic field, $B_{\|}$, along the NV axis can further split the $|m_s = \pm 1\rangle$ states, isolating an effective two-level system with transition frequency ω_0. The NV con-

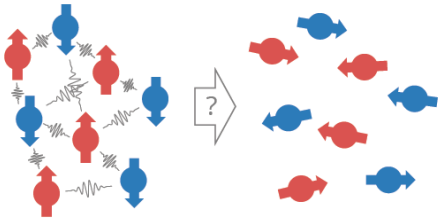

Figure 4.1: Schematic image depicting two groups of oppositely polarized spins with local on-site energy disorder. Due to long-range dipolar interactions, such a system will eventually thermalize to an unpolarized spin state.

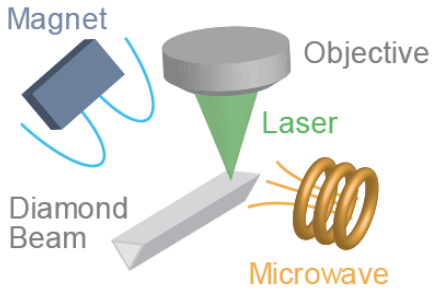

Figure 4.2: Experimental setup diagram showing a beam-shaped piece of diamond containing nitrogen vacancy centers, confocally addressed via a 532 nm laser. External magnetic fields as well as pulsed microwave radiation are used to control the defect's spin degrees of freedom.

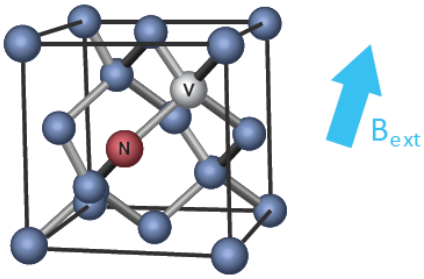

Figure 4.3: The crystallographic structure of diamond contains four possible NV quantization axes, defined by the position of the nitrogen atom and the adjacent vacant lattice site. A NV ensemble in diamond therefore consists of four groups A,B,C,D. An external magnetic field (B_{ext}) is used to split each group's spin degrees of freedom.

centration in our sample is approximately 45 ppm, yielding an average NV-to-NV separation of 5 nm and a corresponding typical dipolar interaction strength $J \sim (2\pi)\ 420$ kHz; crucially, this is significantly faster than typical spin coherence times. Owing to an abundance of other paramagnetic impurities in diamond (consisting mainly of nitrogen electronic spins and ^{13}C nuclear spins), our system is also characterized by strong, on-site disorder. For each NV, this disorder arises from random magnetic fields generated by its local environment. This results in a distribution of transition frequencies ($\omega_0 + \delta_i$, Fig. 4.5) and allows us to extract the effective disorder strength, $\delta_i \in \mathcal{N}(W)$, from the electron spin resonance (ESR) linewidth, $W \approx (2\pi)\ 4.0$ MHz (Fig. 4.4).

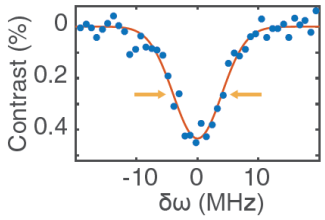

Figure 4.4: ESR scan of a single transition of NV spins (blue points). Red solid line represents a Gaussian fit showing a linewidth corresponding to the average disorder in the sample (orange arrows).

In addition, each NV center can be oriented along any of the four crystallographic axes of the diamond lattice. Different projections of an external magnetic field naturally lead to distinct energy splittings and define four unique NV groups, $\{A, B, C, D\}$, which can be individually addressed and controlled via resonant microwave radiation (Fig. 4.5). By tuning the direction of the magnetic field, one can control the number of spectrally overlapping groups (e.g. groups B,C in Fig. 4.5) and hence the effective density of spins.

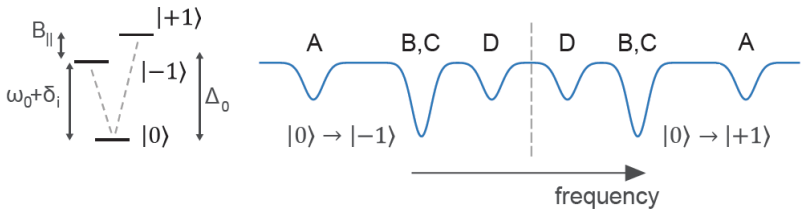

Figure 4.5: Simplified NV level scheme showing the spin degrees of freedom in the optical ground state. A large zero-field splitting Δ_0 in combination with a magnetic field induced Zeeman shift leads to individual addressability of the spin sub-levels. The solid blue line shows a schematic representation of an ESR scan, revealing the spin transitions of all four NV groups. Here, the orientation of the external magnetic field is chosen in such a way that NV group B and C experience the same magnetic field projection ($B_{||}$), leading to spectral degeneracy.

4.4 Interacting NV Ensemble

To directly probe the interaction strength within our system, we perform a double electron-electron resonance (DEER) measurement between two NV groups, A and B (Fig. 4.6, bottom inset). The embedded spin echo protocol decouples group A from slowly varying magnetic noise. The additional π-pulse on group B after half of the total evolution ensures that the interaction-induced dephasing accumulates throughout the entire sequence. Thus, as depicted in Fig. 4.6, by comparing the decay of group A with and without the π-pulse, one can extract the interaction strength $\sim (2\pi)\ 420$ kHz (see appendix D). To further verify that the additional dephasing indeed originates from inter-group interactions, we fix the total evolution time and vary the frequency, ω, of the group B π-pulse, observing a clear resonance when $\omega = \omega_0^B$ (Fig. 4.6 top inset).

By tuning additional NV groups into spectral resonance, we can estimate the bare dephasing rate, γ_b. As a function of the number of resonant groups, ν, we find a total dephasing rate, $\gamma_T = \gamma_b + \nu\gamma_0$, where $\gamma_b \approx 0.9$ MHz and $\gamma_0 \approx 0.4$ MHz. The linear dependence

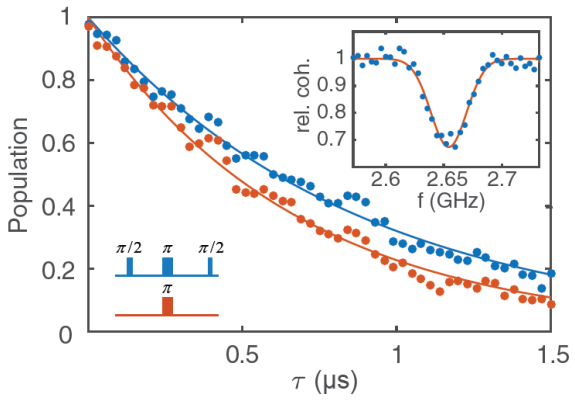

Figure 4.6: Double Electron-Electron Resonance scan (red points) showing faster decay than a spin echo sequence (blue points). Solid lines indicate exponential fits to the data. Inset shows the relative spin-echo coherence time at a fixed time τ as a function of driving frequency of the second group.

of γ_T on ν confirms that the system resides in an interaction limited regime (Fig. 4.7).

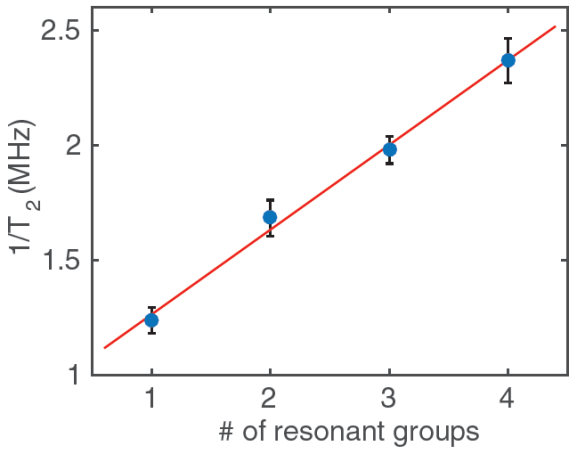

Figure 4.7: Spin echo coherence time as a function of resonant NV groups. (blue points). The red solid line represents a linear fit to the data. Errorbars correspond to 1 σ.

4.5 Coherent Spin Control

Understanding the nature of dipolar thermalization in our system requires the ability to tune both the interaction and disorder strength. To this end, we introduce a toolbox based upon a combination of spin-locking and Hartman-Hahn (HH) resonances, both of which rely upon continuous microwave driving [103, 104, 105]. For excitation with Rabi frequency Ω, this defines a "dressed-state" basis, $|\pm\rangle \approx (|m_s = 0\rangle \pm |m_s = -1\rangle)/\sqrt{2}$, with energy splitting $E_i = \sqrt{\Omega^2 + \delta_i^2}$. In this basis, one can tune the effective disorder, $\tilde{\delta}_i \approx \delta_i^2/(2\Omega)$ with standard deviation W_{eff}, by simply adjusting the Rabi frequency. In the case of spin-locking, we initialize NVs along the $\hat{x}$-axis via a $\pi/2$-pulse, thereby polarizing in the dressed-state basis. Following evolution for time τ, an additional $\pi/2$-pulse measures depolarization in this basis (Fig. 4.8).

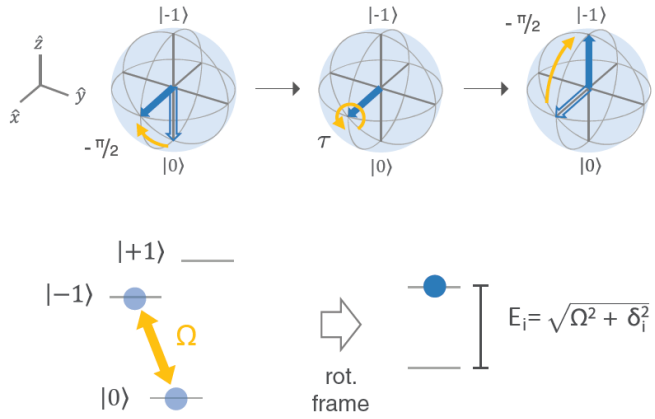

Figure 4.8: Schematic diagram depicting a spin-lock sequence. An initial -π/2 pulse around the y-axis is followed by continuous driving around the x-axis. This creates a dressed spin basis, in which the two eigenstates $(|m_s = 0\rangle + |m_s = -1\rangle)/\sqrt{2}$ and $(|m_s = 0\rangle - |m_s = -1\rangle)/\sqrt{2}$ are separated by E_i. Another -π/2 pulse around the y-axis is subsequently used to convert the acquired phase back into population.

The microscopic origin of this depolarization is related to the presence of short-lived

spins in our system and can be energetically suppressed by increasing Ω [106]. In addition, the interplay between spin-locking and the $S = 1$ nature of NVs leads to a cancellation of the exchange portion of interactions between NVs of the same group (see appendix D). The combined effect of these suppressions is evinced in Fig. 4.9, where one observes the dramatic enhancement of the spin-locking depolarization time, enabling us to prepare a single group of polarized NVs with tunable disorder and long lifetime.

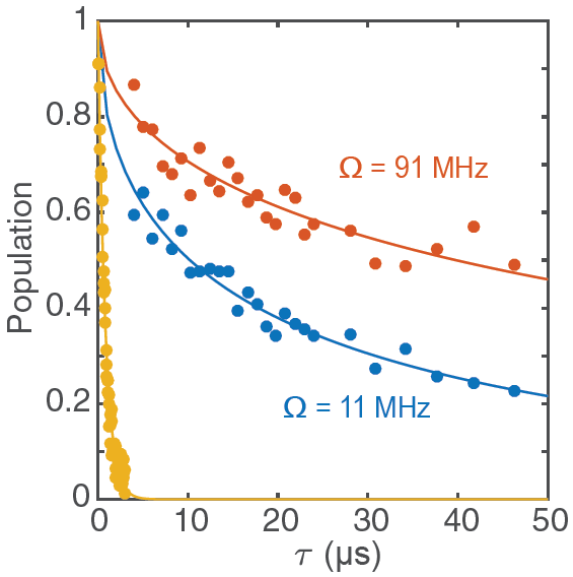

Figure 4.9: Spin-lock coherence decay for low (blue points) and high CW driving power (red points) showing significant extension beyond the spin echo coherence time (orange points).

4.6 Thermalization Dynamics

This provides an ideal starting point to probe dipolar thermalization dynamics. In particular, we utilize Hartmann-Hahn resonances to control the resonant polarization exchange between two groups of NVs and observe the associated dynamics. The two groups are ini-

tialized along $+\hat{x}_A$ (group A) and $-\hat{x}_B$ (group B), and spin-locked with Rabi frequencies Ω_A and Ω_B (Fig. 4.10).

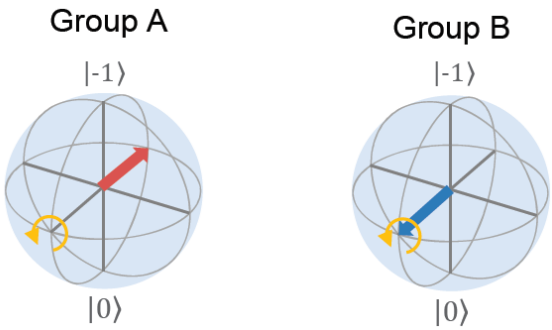

Figure 4.10: Schematic diagram depicting opposite phase spin-lock driving of two separate groups of NVs (A and B) leading to two oppositely polarized groups of spins in the dressed state spin basis. By matching the two driving powers resonant population transfer (Hartmann-Hahn condition) can be achieved.

This results in two oppositely polarized spin ensembles. In the dressed-state basis, the Ising interaction between the groups is transformed to spin exchange and leads to cross-relaxation when $\Omega_A = \Omega_B$ (HH condition) [103, 104, 105]. This is evidenced by the sharp resonance of the blue curve in Fig. 4.11. To extract coherent thermalization dynamics from the HH signal, we normalize using a HH reference at a detuned driving frequency.

As previously discussed, the effective disorder within a single NV group can be tuned by varying the spin-locking Rabi frequency. In the case of HH, the common Rabi frequency, $\Omega = \Omega_A = \Omega_B$ controls the disorder (Fig. 4.12), allowing us to study its impact on the rate of thermalization. Indeed, for larger Rabi frequencies, we observe a decrease in the linewidth of the HH resonance owing to a reduction in the effective disorder (Fig. 4.11 inset).

Leveraging the above toolbox, we investigate the dynamics of spin thermalization be-

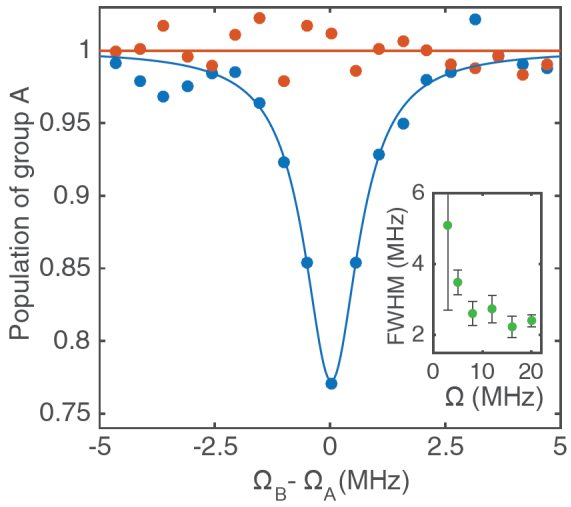

Figure 4.11: Population of group A in a double spin-lock sequence as a function of driving power of group B, showing the Hartmann-Hahn resonance (blue points). Red data shows spin-lock coherence without driving of other groups. The solid blue curve represents a Lorentzian fit to the data. Inset shows the resonance linewidth as a function of applied Rabi frequency. Errorbars correspond to 1 σ.

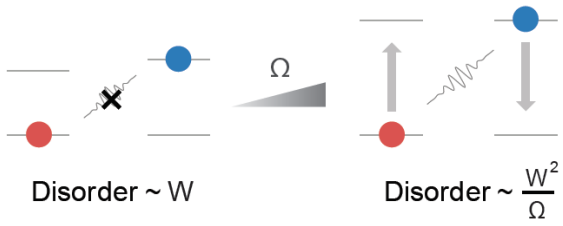

Figure 4.12: Diagram showing that increasing the common Rabi frequency reduces the effective disorder of the system leading to more efficient spin transfer.

tween two NV groups as a function of disorder. Monitoring the polarization of group A reveals slow decay over a time scale much longer than that of nearest neighbor interactions ($\sim$ 3 μs), as shown in Fig. 4.13. Moreover, the functional form of the decay fits neither a simple exponential nor a diffusive power law ($\sim t^{3/2}$).

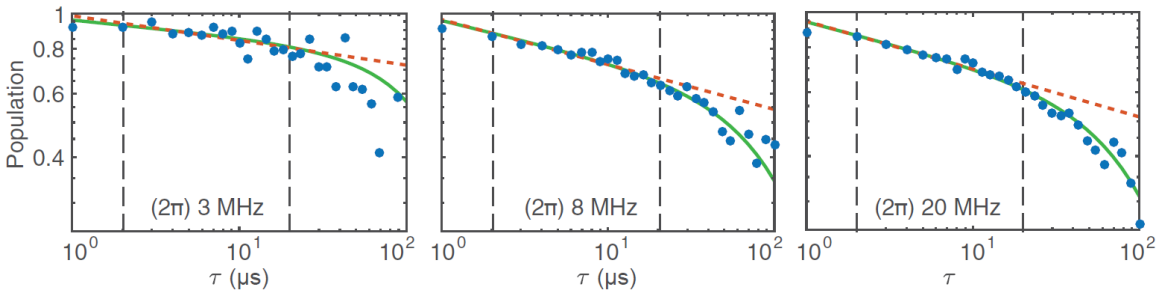

Figure 4.13: NV polarization decay under Hartmann-Hahn conditions for three different driving strengths. Dashed black lines indicate the intermediate regime over which the power law (dashed red line) is fit. Green solid line indicates Monte-Carlo fit of a single particle model including time dependent disorder.

4.7 Discussion

To understand these observations, we turn to a theoretical description of the system. Under continuous microwave excitation, each group of NVs is characterized by an intra-group Hamiltonian,

$$H_A = \sum_{i\in A}(\delta_i\sigma_i^z + \Omega_A\sigma_i^x) + \sum_{i,j\in A}\frac{J_{ij}}{r_{ij}^3}\left(\sigma_i^x\sigma_j^x + \sigma_i^y\sigma_j^y - \sigma_i^z\sigma_j^z\right), \tag{4.1}$$

where $\vec{\sigma}$ are spin-1/2 operators describing the two-level system ($|m_s = 0\rangle$ and $|m_s = -1\rangle$), δ_i is the on-site disorder, Ω_A is the Rabi frequency, r_{ij} is the distance between spins and J_{ij} is the orientation dependent coefficient of the dipolar interaction with typical strength $J_0 = (2\pi)\ 52$ MHz·nm^3. Between different groups, the spins interact via an inter-group Hamiltonian,

$$H_{AB} = -\sum_{i\in A,j\in B}\frac{J_{ij}}{r_{ij}^3}\sigma_i^{z_A}\sigma_j^{z_B}, \tag{4.2}$$

where $\hat{z}_A$ ($\hat{z}_B$) is the NV quantization axis for group A (B). We note that both H_A and H_{AB} are effective Hamiltonians in the rotating frame at the NV transition frequency (ω_0^A, ω_0^B) and that energy non-conserving terms have been eliminated (see appendix D).

A full treatment of many-body thermalization for $H_T = H_A + H_B + H_{AB}$ is both analytically and numerically intractable. However, in the limit of strong disorder, one expects the initial dynamics to be dominated by single spin resonances.

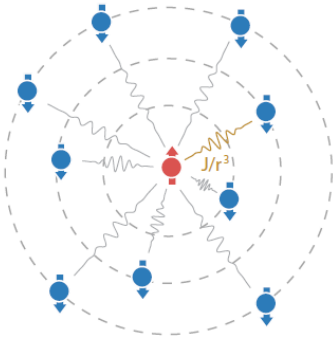

Figure 4.14: Schematic diagram of single particle resonance counting argument predicting a power-law decay profile.

To this end, we consider a single NV excitation at the center of an ensemble of polarized spins (Fig 4.14). The spin-flip dynamics of this NV excitation are captured by an effective Hamiltonian describing the single particle limit of H_T,

$$H_{eff} = \sum_i \tilde{\delta}_i \sigma_i^x - \sum_{ij} \frac{J_{ij}}{r_{ij}^3}(\sigma_i^+ \sigma_j^- + h.c.), \tag{4.3}$$

where $\sigma^{\pm} = \sigma^y \pm i\sigma^z$. Under H_{eff}, the central excitation relaxes via long-range exchange interactions. To characterize these decay dynamics, we calculate the survival probability, $P(t)$, of the NV excitation via a combination of analytic resonance counting and numerical simulations. For a given disorder realization, resonance counting proceeds as follows. Two spins at sites i and j are on resonance at time t if: (1) their energy mismatch is smaller than their dipolar interaction strength, $|\tilde{\delta}_i - \tilde{\delta}_j| < \beta J_{ij}/r_{ij}^3$ (β is a dimensionless constant

of order unity that regulates the resonance condition), and (2) the interaction occurs within the time-scale t, $J_{ij}/r_{ij}^3 > 1/t$. At $t = 0$, there exist no resonances and $P(0) = 1$. As the system evolves, a network of resonances develops and the central excitation becomes delocalized within this network. For simplicity, let us assume that this excitation is equally shared among all spins in the network, wherein $P(t) = \sum_k \frac{1}{k}\text{Pr}(k;t)$ with $\text{Pr}(k;t)$ being the probability that the central spin is a part of a k-resonating cluster. For dipolar spins, the dominant contribution to $P(t)$ comes from $k = 1$ (see appendix D). This implies that once the central spin finds a single resonant partner, it will likely delocalize throughout the entire system. Hence, $P(t)$ is approximately given by the probability of having found no resonances up to time t or equivalently up to distance $R(t) \equiv (J_0 t)^{1/3}$. This probability can be computed as the product of probabilities of having no resonant spins at every distance r,

$$P(t) = \prod_r^{R(t)} \left(1 - 4\pi n r^2 dr \frac{\beta J_0/r^3}{W_{\text{eff}}}\right) \propto t^{\frac{-4\pi n \beta J_0}{3W_{\text{eff}}}}, \tag{4.4}$$

where one finds a power-law decay with a disorder dependent exponent $\eta = 4\pi n \beta J_0/(3W_{\text{eff}})$. We verify these results via numerics of up to $N = 10^4$ spins, where a clear power-law decay is obtained over more than two decades in time (Fig. 4.15). The saturation of $P(t)$ at long times owes to finite size effects.

Comparing the experimentally observed spin relaxation with our single particle analysis reveals multiple dynamical regimes. At short times ($t < 2$ μs), we observe a small but rapid drop in polarization owing to off-resonant nearest neighbor couplings. At intermediate times (2 $\mu\text{s} < t < 20$ μs), relaxation is indeed consistent with a power law, exhibiting a disorder-dependent exponent (Fig. 4.13), whose value is in reasonable agreement (Fig. 4.16) with the single-particle theory (with no free parameters).

We emphasize that such power-law relaxation is also consistent with results obtained

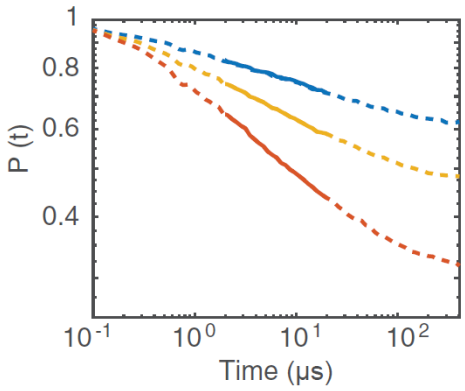

Figure 4.15: Exact diagonalization simulation results for a simplified single excitation model showing power-law decay shape for three different driving strenths, (2π) [3, 8, 20] MHz. Solid lines indicate the intermediate time over which a power-law decay is observed in the experiment data.

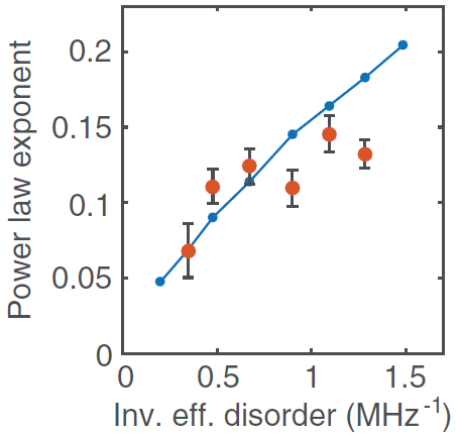

Figure 4.16: Decay rate exponent of the power law as a function of decreased effective disorder (red points). Blue points correspond to simulation results of our theory model (see appendix D).

from random-banded matrix theory [98, 101]. At late times ($t > 20$ μs), the observed decay accelerates and deviates significantly from the intermediate power law. Interestingly, this deviation can be well-captured by the introduction of time-dependence to the on-site disorder, $\tilde{\delta}_i(t)$. In our system, such time-dependence arises naturally from the dynamics of

an external spin bath and from fluctuations of the local magnetic field owing to many-body interactions.

Intuitively, one expects that time-dependent disorder will enhance relaxation: a pair of spins that were previously off-resonant may be brought into resonance as the on-site fields change in time. To quantify this effect, let us consider the situation where $\tilde{\delta}_i$ exhibits uncorrelated jumps at rate Γ. For each time interval t, $\tilde{\delta}_i$ remains static with probability $e^{-\Gamma t}$, while the survival probability undergoes power-law decay, $P(t) \sim (t/t_c)^{-\eta}$. Averaging over intervals then yields $\overline{P(t)} \approx \sum_{k=0}^{\infty} c_k \frac{(\Gamma t)^k}{k!} (t/t_c)^{-(k+1)\eta} e^{-\Gamma t}$ with dimensionless constants c_k, implying that the effective power-law exponent increases on a time scale $1/\Gamma$ (see appendix D). For $1/\Gamma \sim 50$ μs, we find that $\overline{P(t)}$ quantitatively agrees with the experimental relaxation dynamics over all time scales (Fig. 4.13).

To further clarify the possible microscopic origins of our time-dependent disorder, we compare their intrinsic time-scales with the extracted $1/\Gamma \sim 50$ μs. As aforementioned, each NV couples to a bath composed of paramagnetic impurities, including P1 centers (nitrogen) and NV spins from non-participant groups C and D. Depolarization dynamics of these impurities will change the effective on-site fields leading to time-dependent disorder. Both the measured NV depolarization time ~ 50 μs and the spin-diffusion lifetime of P1 centers ~ 70 μs (estimated from a 20 ppm nitrogen density) are indeed consistent with the extracted Γ [106, 107]. Time-dependent disorder may also arise as a consequence of many-body dynamics within the same group of NV centers. In particular, the fraction of depolarized NVs may generate a time-dependent mean-field potential for the remaining polarized NVs via intra-group Ising interactions ($\sigma_i^x \sigma_j^x$). Owing to the random position of NVs, this potential behaves as an additional on-site field, thereby modifying the disorder.

A few remarks are in order. First, one expects that the time-dependence arising from dynamics of the paramagnetic impurity bath and intra-group mean-field potentials will exhibit temporal correlations. Moreover, only a fraction, f, of the total on-site disorder field is expected to be time-varying; indeed, there exist strong local strain fields from lattice defects, long-lived nuclear spins, and trapped charges whose dynamics are significantly slower than the experimental time-scales. A detailed analytic and numeric treatment of such correlated disorder is presented in appendix D. While such correlated disorder yields qualitatively similar results, one extracts a smaller jump rate $\Gamma' \sim 1/60\ \mu\text{s}^{-1}$ and a fraction, $f \sim 10\%$. Second, while the time-dependence of intra-group Ising interactions enhances relaxation at late times, at early times, when the majority of NV spins are polarized, such interactions may contribute to stronger disorder. Third, our microscopic picture suggests the tantalizing possibility to directly control the disorder potential in a time-dependent fashion by driving either P1 centers or NV groups C and D.

4.8 Conclusion and Outlook

We have introduced dense ensembles of dipolar NV centers as a platform for studying quantum many-body dynamics. The natural toolbox associated with spin-locking and Hartmann-Hahn resonances enables the preparation of long-lived initial states and controlled cross-relaxation experiments. Our results demonstrate that even in the presence of long-range interactions, strong disorder can significantly slow the relaxation of local observables beyond typical interaction time scales. The quantitative agreement between observed spin relaxation power laws and single-particle resonance counting suggests that the dynamics are dominated by rare resonances. Looking forward, dynamical decoupling

techniques open the door to engineering a broader class of interaction Hamiltonians, while the fabrication of diamond nanobeams and membranes allow for the exploration of spin dynamics in lower dimensional systems [108].

"Every science has a beginning but no end."

Anton Chekhov

Chapter 5

Conclusion and Outlook

5.1 Diamond Spins as a Platform

In this thesis we demonstrated how a high degree of control over nitrogen vacancy centers in diamond allowed us to find promising applications in the fields of quantum information science and quantum sensing. In the next section of this dissertation we will provide an outlook on one of our currently ongoing projects, demonstrating the power of NV centers as a nanoscale thermometry tool in biological applications. We show how local, subcellular temperature control can be used to study the heat dependent rate of the embryonic development of worms. In Chapter 4 we showed first results of many-body physics with NV centers in diamond. Through the use of coherent control techniques we achieved a well controlled, long-range interacting spin system under the influence of tunable on-site disorder. Together with the ability to locally prepare and read out the spin state as well as its room temperature operation and long spin lifetime, this makes NV centers in diamond an ideal platform to study many-body spin dynamics of a large system.

5.2 In Vivo Diamond Thermometry

In Chapter 3 we have demonstrated how nanodiamonds containing NV centers can be used as accurate temperature sensors for biological systems. These results enable us to study heat dependent biological processes in a wide array of experiments. A particularly interesting process that sensitively depends on temperature is the early embryonic development of the worm *Caenorhabditis elegans*.

5.2.1 Model Organism C. Elegans

Caenorhabditis elegans (*C. elegans*) is a small (≈1 mm) worm that scientists have been fascinated by for over a century [109]. *C. elegans* was not only the first multicellular organism to have its whole genome sequenced, but has over the past decades led to great discoveries and multiple nobel prizes in biology. Specifically, due to its fast reproductive cycle and transparent body, it was one of the first animals used to study developmental biology.

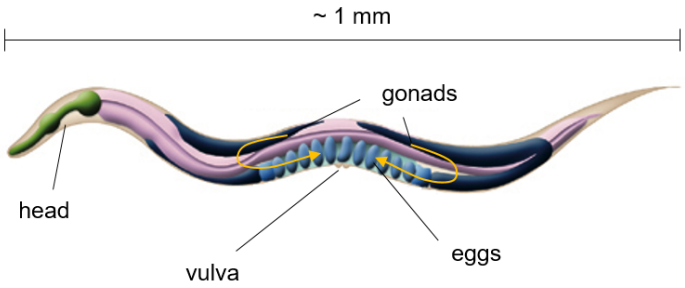

Figure 5.1: Schematic image of an adult *C. elegans* worm (adapted from www.wormatlas.org). Arrows indicate the developmental path inside the gonads, from immature oocytes to fertilised eggs.

Figure 5.1 shows an adult worm containing eggs, which are fertilised in the more distal

regions of the two gonads. As they travel towards the vulva, embryonic development begins, which is characterized by a stereotyped succession of cell divisions. These divisions can be observed via a microscope, and have been mapped out in terms of division time and function of each cell.

5.2.2 Temperature dependent Development

Carefully recording the timing of cell divisions of the *C. elegans* embryo reveals that individual division times are highly reproducible. Furthermore, by changing the external temperature, the global cell division timings within the egg can be sped up or slowed down significantly (Fig. 5.2).

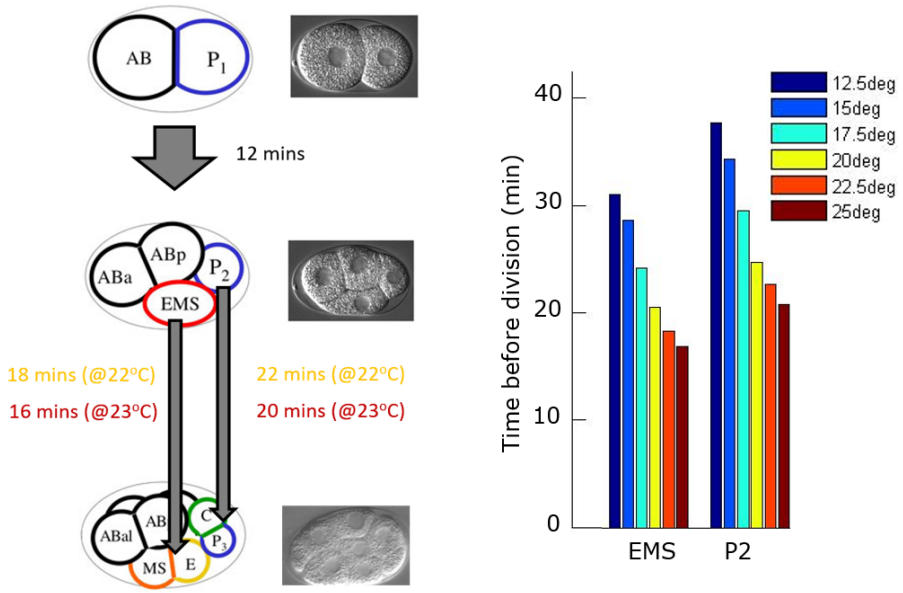

Figure 5.2: Diagram of three early stages of worm embryonic development next to corresponding phase contrast microscopy images (adapted from www.wormbook.org). Individual cell names indicate lineage and eventual cell type (neuron, intestine, etc.). Bar chart indicates division times of P_2 and EMS cells at various external temperatures.

5.2.3 Probing Cell Development

Both the components inside a cell (e.g. intracellular proteins and lipids) as well as the environment outside (e.g. signaling chemicals from neighboring cells) can influence a cells behavior and its fate. Understanding the differential roles of intra- and extracellular factors at individual stages of development is a central objective in developmental biology. The stereotyped cell divisions in the early worm development present an excellent system in which we can employ thermometry to provide insight into this question: By carefully heating an individual cell, while keeping the surrounding cells at a constant temperature, we can test whether the division timings of those neighbouring cells are programmed by internal factors (i.e. remain unaffected by the heated cell), or whether cell division timing is coordinated across the entire embryo (i.e. neighbouring cells follow the division time of the heated cell). This experiment will therefore illustrate whether cell-to-cell communication is important for developmental timing in the early embryo.

To perform such experiments it is necessary to accurately induce and measure a highly localized temperature gradient within a single *C. elegans* egg. By utilizing our nanodiamond thermometry technique together with a focused infrared laser for local heating, we have developed an accurate tool to control and verify the egg's local thermal environment (Fig. 5.3).

To introduce our nanodiamonds into *C. elegans* eggs we inject a biotin modified nanodiamond solution into the gonad of a worm (Fig. 5.4) [110]. This leads to incorporation of diamonds into newly formed eggs (Fig. 5.5 top). To monitor the cell division rate we use a particular strain of *C. elegans* that was genetically modified to express green fluorescence protein (GFP) inside the cell nuclei, making it easy to observe cell divisions (Fig. 5.5

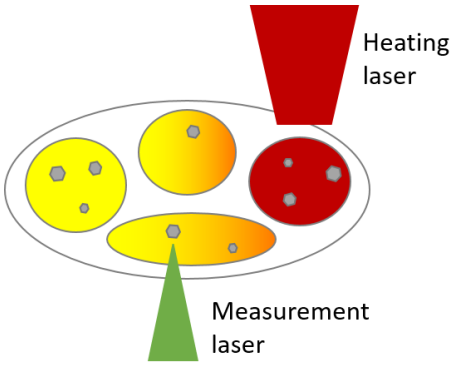

Figure 5.3: Experimental approach visualized in a four cell stage egg. A focused infrared laser is used to heat an individual cell, while a confocal green laser is used to read out local temperature changes at various nanodiamond locations across the egg.

bottom). With this toolbox we will be able to accurately measure the influence of temperature on early embryonic development as well as study the interdependence between cell division timings, giving new insights into the fundamental question of how developmental timing and cell fate are controlled.

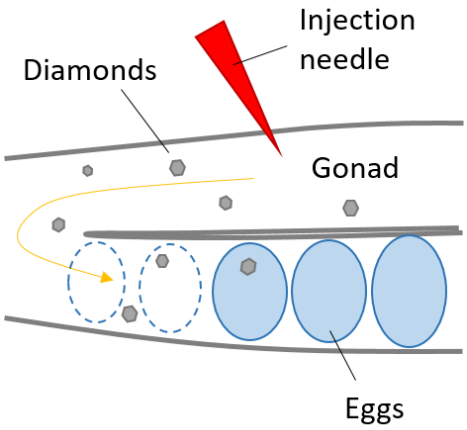

Figure 5.4: Diagram showing nanodiamond injection into the gonads. Over time the introduced diamonds get dispersed and incorporated into newly formed eggs.

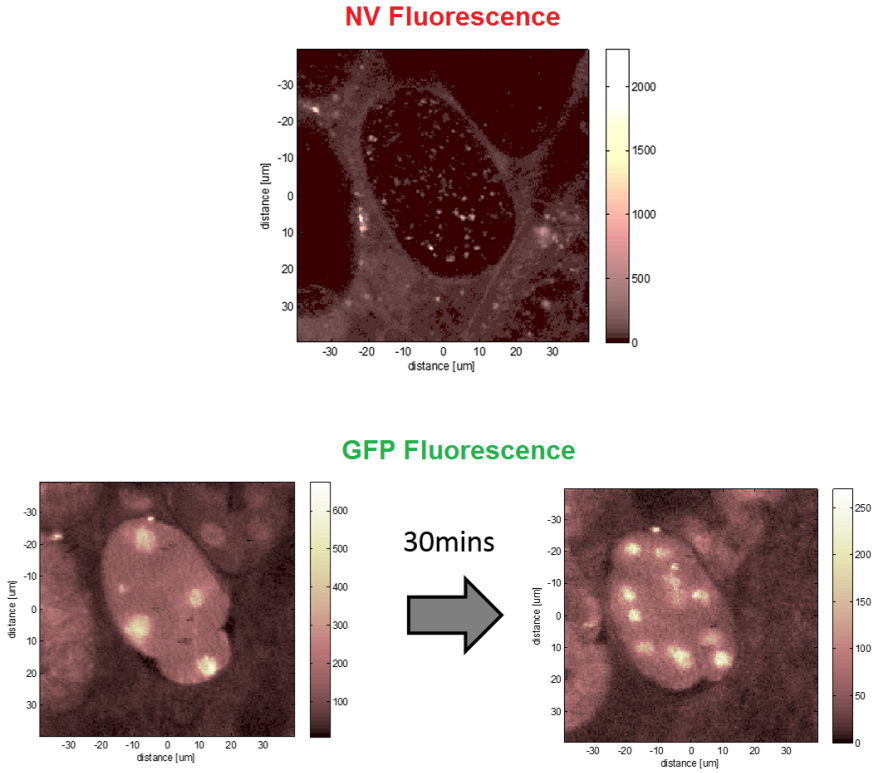

Figure 5.5: Top: Fluorescence scan with 532 nm excitation, showing nanodiamonds containing NV centers dispersed throughout a newly formed *C. elegans* egg. Bottom: GFP fluorescence scan showing an egg transitioning from the 4 to 8 cell stage. Bright spots indicate the location of cell nuclei.

Appendix A

Microwave Transmission Line Fabrication

A.1 Coplanar Waveguides

In order to drive NV centers with high Rabi frequency it is common use to employ a high power (few watts) microwave (MW) amplifier together with an 2-d waveguide structure (see Fig. A.1). In such a geometry the NV center can be located in the nearfield of the microwave structure, allowing for up to GHz spin manipulation [111]. Since common microwave equipment such as SMA cables are impedance specified at 50 Ω it is necessary to impedance match the coplanar waveguide (CPW) to the same value. The impedance is a function of the geometry of the waveguide and can be easily estimated via online tools, or with the help of 2.5-d or 3-d microwave simulators such as Sonnet or CST Studio. Such simulations however are only necessary if the length of the unmatched structure is comparable to or larger than the wavelength in the material. Therefore if operating at a few

GHz, our omega structure of about 2 mm can be neglected. Depending on the aspect ratio requirements there are two common ways of fabricating such CPWs using a lift-off or etch-back technique.

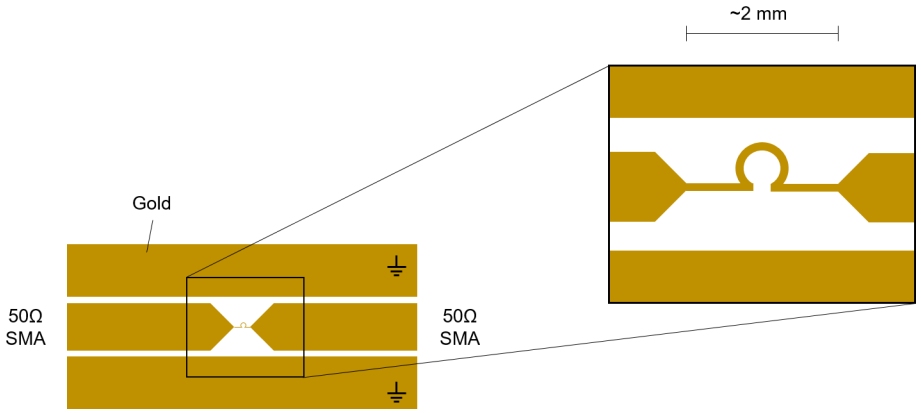

Figure A.1: Coplanar waveguide structure used for microwave excitation of the diamond sample. The metal structure is lithographically fabricated on top of a glass coverslip. The outer ground as well as the center conductor can be wirebonded to a PCB or directly soldered to an SMA connector. The zoom-in shows the central conductor structure. The omega shape is used to achieve high Rabi frequencies at the center.

A.1.1 Lift-off Process

The lift-off process consists of an initial photolithographic resist patterning followed by metal deposition and a subsequent lift-off of the unwanted parts of metal (see Fig. A.2). This process is recommended when the thickness of the structure is less important than the lateral dimensions. Meaning it is recommended for smaller, more delicate metal structures, especially when the thickness can be around 500 nm or less. This comes however at the cost of a relatively long processing time as well as a mediocre success rate (often some of the metal parts that should remain on the sample get ripped off during the fabrication process).

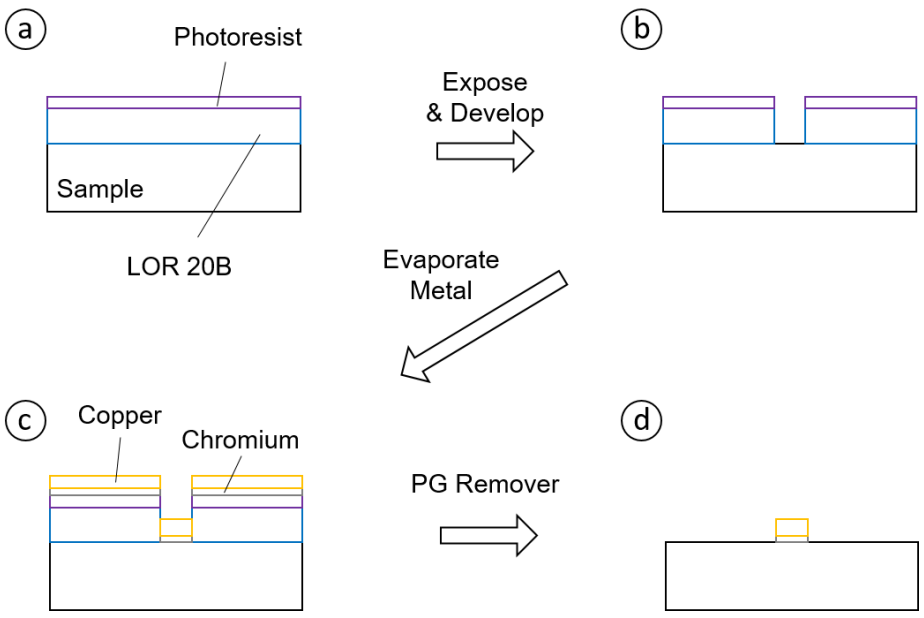

Figure A.2: Schematic diagram depicting fabrication steps for a lift-off procedure. During step (a) the sample is spin coated with a 3 μm layer of LOR 20B as well as a thin layer of photoresist (ie. Shipley 1813). After a masked exposure and development step we obtain a resist structure (b). Next we evaporate an adhesion layer of chromium and a 1 μm layer of copper (c). In a last step the resist as well as the excess metal is removed in a PG Remover bath (d).

A.1.2 Etch-back Process

Using the etch-back procedure is a faster and more robust way of fabricating a CPW (see Fig. A.3). It is usually the recommended procedure, however it comes at the expense of less clean structures. Due to the isotropic metal etching the edges of each trace will be undercut by at least the same amount as the thickness of the traces, leading to less sharp edges. However in common CPW structures the minimum feature size is larger than 10 μm such that an undercut equivalent to the thickness of about 1 μm is negligible.

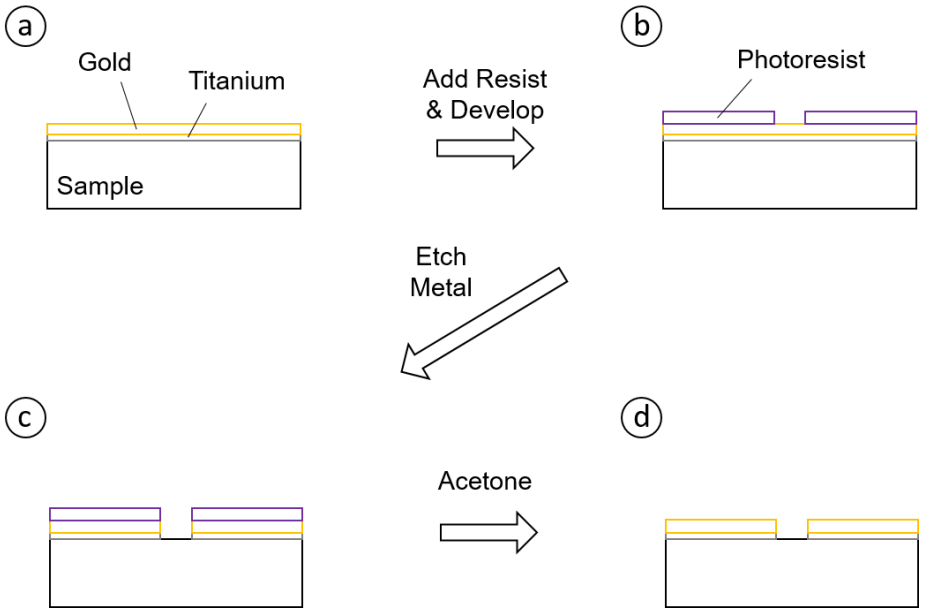

Figure A.3: Schematic diagram depicting fabrication steps for an etch-back procedure. In a first step we evaporate an adhesion layer of titanium as well as a 1 μm layer of gold on top of the sample (a). Next, a thin layer of photoresist (ie. Shipley 1813) is spin coated onto the sample followed by a masked exposure and development step (b). Next we can remove the unwanted metal structures via a few minutes of Au etch followed by a dip into a 10:1 mixture of water and 49% HF to remove the titanium (c). A final wash with acetone and DI water cleans off any excess resist (d).

A.2 RF Coils

Due to the significantly smaller gyromagnetic ratio of nuclear spins, their coherent control is much slowed down compared to NV centers. Especially when performing dynamical decoupling it might therefore be helpful to try to increase the Rabi frequency as much as possible. Due to the lower excitation frequency one can employ amplifiers up to few hundreds of watts. Since such high powers would lead to significant heating and drifts on our CPW it is helpful to create a separate RF structure on a substrate with higher thermal conductivity than glass, such as alumina. Additionally since the resonance frequency of

nuclear spins is much lower (in the MHz range) we can utilize non impedance matched structures that are much longer than the Omega shape in the previous section. By creating a microcoil consisting of ≈20 windings and 40 μm thick copper traces on top of an alumina substrate it is possible to achieve nuclear Rabi frequencies close to 1 MHz (see Fig. A.4). The fabrication process consists of a series of lithography as well as electroplating steps detailed in Figure A.5.

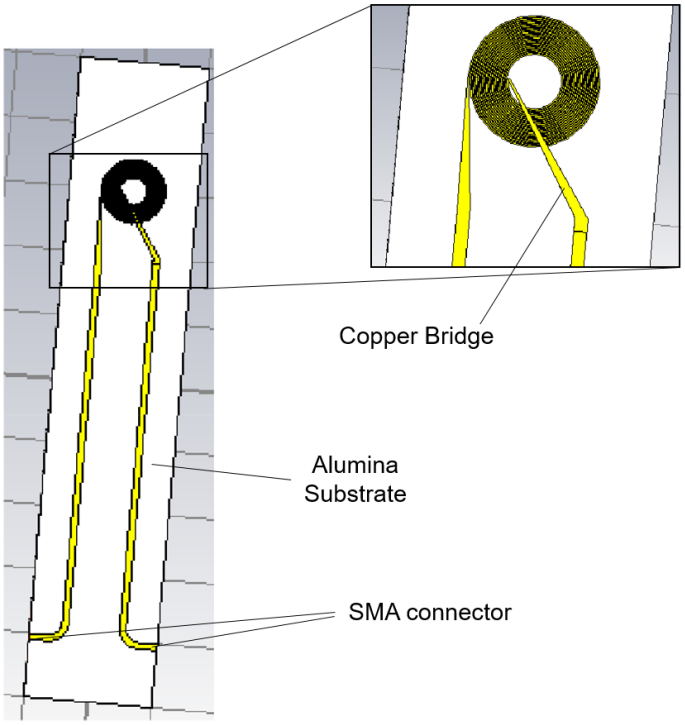

Figure A.4: CAD image showing the RF microcoil structure. The coil consists of 10-50 windings of a copper trace on top of an alumina substrate for good thermal conductivity. To connect the trace at the end of the coil to the outside a bridge is fabricated that crosses the coil windings. SMA connectors can then be glued to the board and soldered to the conductor.

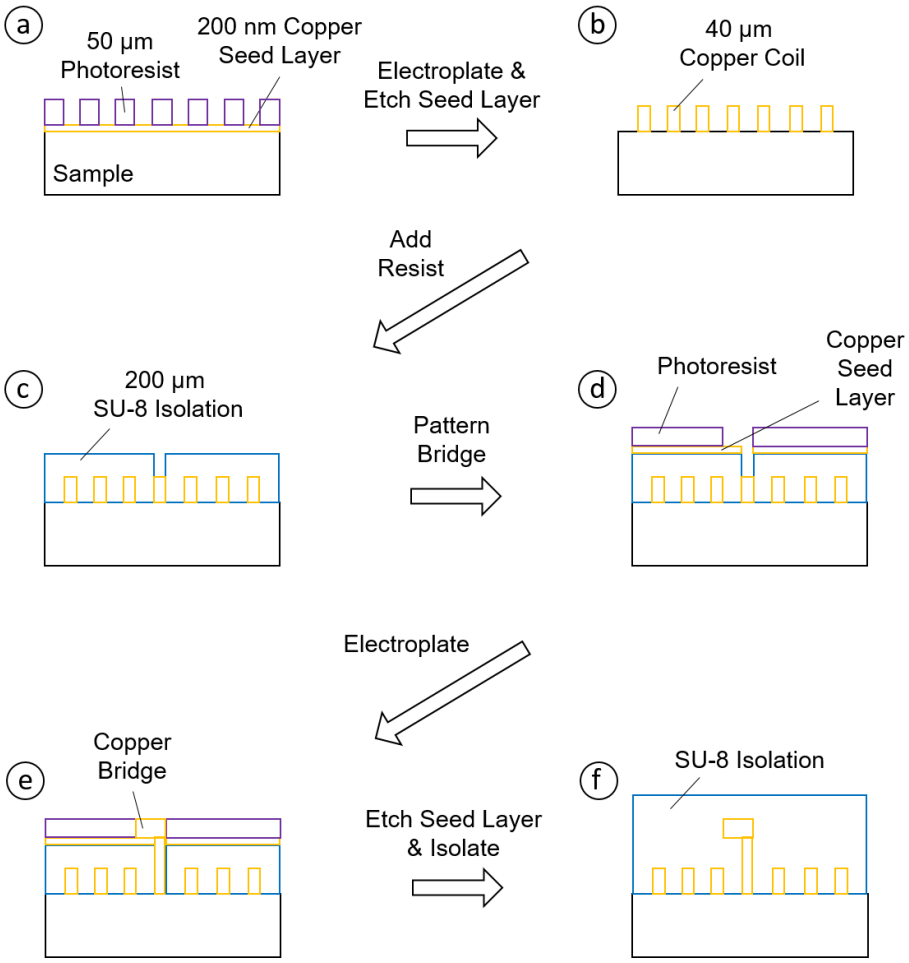

Figure A.5: Schematic diagram depicting fabrication steps to create a microcoil. In a first step we evaporate a thin copper seed layer onto the sample followed by a 50 μm photoresist layer. This resist layer is then exposed via a coil mask structure and developed (a). After a step of copper electroplating at a rate of $\approx$10 μm thickness per hour followed by a quick etch to remove the seed layer we obtain a copper coil structure (b). Next we cover the coil part of the structure with a 200 μm layer of SU-8 photoresist for isolation and develop a small hole at the center reaching down to the most inner loop of the coil (c). Next we add a thin layer of resist (ie. Shipley 1813) to pattern the bridge structure (d) followed by another elctroplating step (e). A final short etch to remove the seed layer is followed by adding a thick layer of SU-8 resist to isolate the whole structure (f).

Appendix B

Supporting Material of Chapter 2

B.1 Materials and Methods

B.1.1 Sample

The sample used in this work is an unpolished ultra-pure diamond grown by chemical vapor deposition. The low substitutional nitrogen concentration of $<$1ppb and high isotopic ^{12}C purity of $99.99\ \%$ leads to electron spin coherence times T_{2e}^{*} long enough to sense a single ^{13}C nuclear spin via a hyperfine interaction of a few kHz.

B.1.2 Optical Setup

The sample is mounted on a xyz-piezoelectric stage in the focal plane of a home-build confocal microscope with a Nikon Plan Fluor 100x oil immersion objective ($N_A = 1.3$). To suppress decoherence of the electronic spin due to external magnetic field fluctuations the microscope is placed inside a μ-metal shield. The magnetic shielding reduces ambient

DC fields by a factor of 80 and suppressed AC fields to better than 40 μG. This allows us to obtain NV electronic spin coherence times of $T_2^* = (470 \pm 100)$ μs. This value agrees well with the linear scaling of T_2^* of the electronic spin as a function of the ^{13}C concentration [7].

Excitation of the NV center is performed by a frequency doubled YAG laser ($\lambda = 532$ nm) using 1.4 mW power corresponding to three times the saturation power. The NV center fluorescence is emitted into the phonon sideband (630-800). The emitted fluorescence beam is separated from the excitation by a dichroic filter and an appropriate long pass filter. The fluorescence beam is then focused onto an avalanche photodiode (APD) after passing a pinhole for confocal microscopy. Short laser pulses are generated by an accusto-optical modulator (AOM) from Isomet in a double pass geometry. The rise time of the AOM is adjusted to be approximately 20 ns. A second, strong (30 mW), green laser beam is coupled into the beam path by a 50/50 polarizing beam splitter cube. To avoid leakage from the shut-off 30 mW beam a mechanical shutter from Thorlabs (switching time ≈ 10 ms) was employed.

B.1.3 Microwave and RF Setup

To coherently drive the electronic spin of the NV center we deliver microwaves to the sample by a transmission line fabricated on a glass coverslip, glued to the diamond sample. To perform pulsed microwave manipulation of the electronic spin we use peak powers of 10 W allowing us to manipulate the electronic spin with a Rabi frequency on the order of $(2\pi)40$ MHz.

To manipulate the ^{13}C nuclear spin using high power radio frequency, a lithographi-

cally patterned micro-coil is fabricated on an alumina substrate [112]. In order to prevent excessive ohmic loss the conductors are then plated with copper in a SU-8 mold to a thickness of around 40 μm allowing peak powers of several hundred watts. To ensure maximal nuclear Rabi frequency the RF-coil is aligned in such a way that the ac RF field of the coil is perpendicular to the external dc magnetic field. This allows us to manipulate our ^{13}C nuclear spin with Rabi frequencies of $\approx (2\pi)100$ kHz.

B.2 Photon Counting Statistics and Readout Fidelity

In this part of the supplementary information we discuss the statistics of detected photons during a repetitive readout of the nuclear spin for a certain integration time. First, we derive an analytical expression for the statistical distribution of the detected photons that is fitted to the data in Fig. 2.6. We then analyze the readout and initialization fidelity derived from these distributions.

B.2.1 Photon Counting Statistics

We start by first pointing out that the probability $p^{(n)}$ for n quantum jumps during the integration window τ is Poissonian-distributed with $p^{(n)} = \frac{\lambda^n}{n!}\exp(-\lambda)$, where $\lambda = \tau/T_{1n}$ and $1/T_{1n}$ is the nuclear depolarization rate. For an integration time of $\tau = 4.4$ s (Fig. 2.6 and Fig. B.2a) and a nuclear spin flip time $T_{1n} = 25$ s, the probability for no quantum jump during readout is $p^{(0)} = 83.8\%$. The probability for one quantum jump is $p^{(1)} = 14.8\%$ and $p^{(n>1)} = 1\%$ for more than one jump. This allows us to restrict the discussion to the case where either zero or one quantum jump takes place during the readout time.

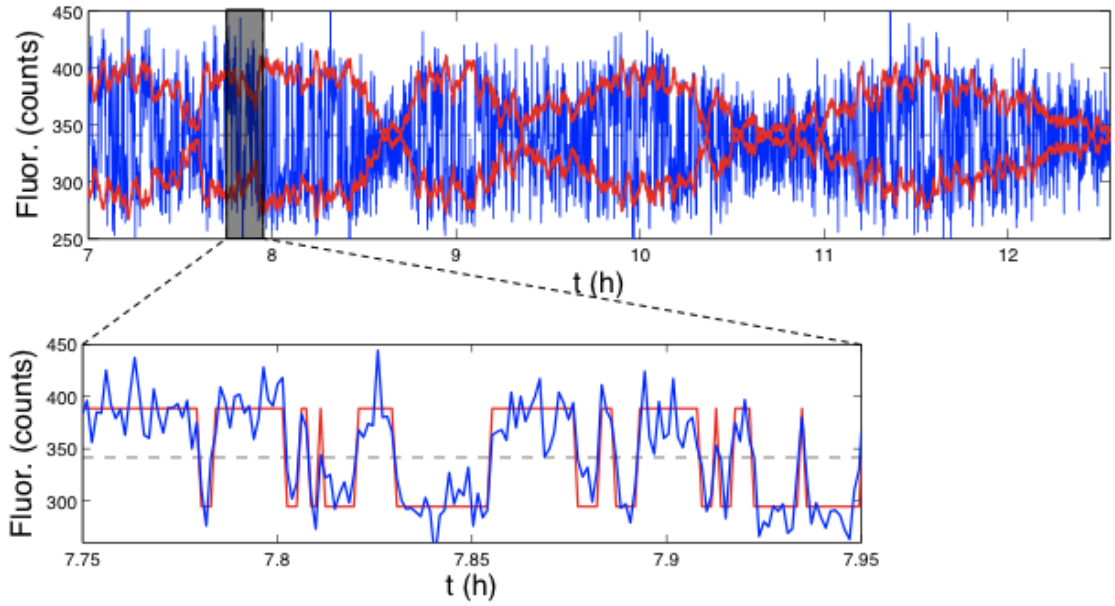

Figure B.1: **—- Fluorescence signal as function of time.** Each point of the blue line is an average of 20,000 repetitive readout. The red line shows the envelope of the fluorescence signal. The zoom in reveals individual quantum jumps.

For no quantum jump event during the readout τ, the photon count statistics $\alpha_s^{(0)}$ is Gaussian:

$$\alpha_s^{(0)}(x) = \frac{1}{\sqrt{2\pi\mu_s}} \exp\left(-\frac{(x-\mu_s)^2}{2\mu_s}\right), \tag{B.1}$$

where μ_s is the average photon count rate for the nuclear spin in the $|s =\downarrow (\uparrow)\rangle$ state and x is the number of detected photons. For the shot-noise limited detection, we take the standard deviation $\sigma_s = \sqrt{\mu_s}$.

In the case of a single quantum jump event, the number of detected photons $\alpha_s^{(1)}$ will no longer be Gaussian distributed. We note that conditioned on one quantum jump occurring during the readout interval τ, the time spent in $|s\rangle$ will be uniformly distributed. Hence the number of counted photons is given by $\mu \sim \mu_\downarrow + (\mu_\uparrow - \mu_\downarrow)Unif$, where $Unif$ denotes the uniform distribution on the interval $(0, 1)$. Taking into account the photon shot noise, we

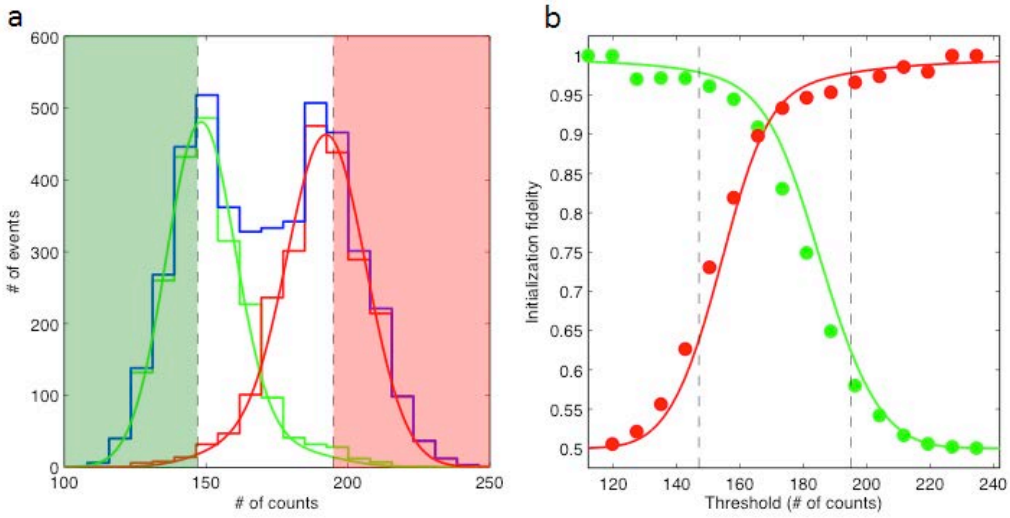

Figure B.2: **—- Photon count statistics and initialization fidelity a,** shows the photon counting statistics after initialization of the nuclear spin to $|\downarrow\rangle$ (green) and $|\uparrow\rangle$ (red). The histograms are measured data and the solid lines are theory fit. The blue histogram is the total distribution. The green(red) area indicates count rates for which the nuclear spin is initialized in $|\downarrow(\uparrow)\rangle$. **b,** shows the initialization fidelity of the nuclear spin in $|\downarrow(\uparrow)\rangle$ green(red) as function of threshold. The points are extracted from the histogram in a, the lines are preparation fidelity extracted from the fits in a.

find the statistics of detected photons conditional on a single nuclear spin flip:

$$\begin{aligned}\alpha^{(1)}(x) &= \frac{1}{\mu_\uparrow - \mu_\downarrow}\int_{\mu_\downarrow}^{\mu_\uparrow} d\mu \frac{1}{\sqrt{2\pi\mu}} \exp\left(-\frac{(x-\mu)^2}{2\mu}\right) \\ &\approx \frac{1}{2(\mu_\uparrow - \mu_\downarrow)}\left(\mathrm{Erf}\left(\frac{\mu_\downarrow - x}{\sqrt{2\mu_\downarrow}}\right) - \mathrm{Erf}\left(\frac{\mu_\uparrow - x}{\sqrt{2\mu_\uparrow}}\right)\right),\end{aligned} \tag{B.2}$$

which is independent of the initial nuclear spin state $|s\rangle$.

Combing eq. (B.1), (B.2) we can find an analytical expression for the photon counting statistics:

$$\alpha_s(x) \approx p^{(0)}\alpha_s^{(0)}(x) + p^{(1)}\alpha^{(1)}(x). \tag{B.3}$$

In Fig. 2.6 we fit this function to the recorded photon counting statistics with $\mu_{\downarrow(\uparrow)}$ being

fit parameters. The measured data is in excellent agreement with our model of Fig. 2.6 and B.2a.

B.2.2 Readout and Initialization Fidelity

As discussed in the main text we define the readout fidelity $\eta_{\downarrow}(n_{thr})$ by the probability of being in nuclear spin $|\downarrow\rangle$ conditional on detecting a photon number smaller than a threshold n_{thr}. The readout fidelity $\eta_{\downarrow}(n_{thr})$ is then defined as

$$\eta_{\downarrow}(n_{thr}) = \frac{P_{\downarrow}(n_{thr})}{P_{\downarrow}(n_{thr}) + P_{\uparrow}(n_{thr})}, \tag{B.4}$$

where $P_{\downarrow(\uparrow)}(n_{thr}) = \int_0^{n_{thr}} \alpha_{\downarrow(\uparrow)}(x)dx$ is the probability that for nuclear spin $\downarrow$ $(\uparrow)$ the number of detected photons is below n_{thr}, and vice versa for $\eta_{\uparrow}(n_{thr})$. For optimal readout fidelity η the threshold n_{thr} is chosen in such a way that $\eta_{\downarrow(\uparrow)}$ is maximized.

The readout fidelity η is determined by initializing the nuclear spin in a known state $\downarrow$ $(\uparrow)$ and consecutively reading it out with our single shot measurement. The readout (20,000 repetitions) allows us then to determine the photon counting distribution depending on the initial state and hence the fidelity η.

This relies on a high initialization fidelity of the nuclear spin to the desired state. To initialize the nuclear spin we perform a repetitive readout. If the recorded counts are smaller than a threshold $n_{thr}^{\downarrow}$ we assign the nuclear spin to $|\downarrow\rangle$ if they are larger than $n_{thr}^{\uparrow}$ we assign $|\uparrow\rangle$. In principle this allows for initialization with fidelity well above 99 $\%$. In Fig. B.2b we plot the initialization fidelity as a function of the threshold $n_{thr}^{\downarrow}$ and $n_{thr}^{\uparrow}$. For a threshold of $147(195)$ counts we can initialize the nuclear spin state with a fidelity of $\approx 97\%$.

B.3 Readout of the ^{13}C Nuclear Spin

This section discusses the details of the ^{13}C readout. We first show that the electron Ramsey fringes can be described by a single sine-function due to dynamical polarization of the ^{14}N nuclear spin. We then discuss the dependence of the fluorescence signal on the detuning from the ESR transition and the implication on the readout fidelity. Finally we give an explanation on how we normalized the results of the repetitive readout.

Throughout this paper we neglect the ^{14}N nuclear spin of the NV center. This is justified since we work at a field of ~ 244 Gauss, which is sufficiently close to the excited state level-anti-crossing at 500 Gauss to dynamically polarize the ^{14}N nuclear spin [113]. As shown in Fig. B.3a the nitrogen nuclear spin is polarized to $71\ \%$ leaving us with nearly sinusoidal Ramsey fringes (Fig. B.3b).

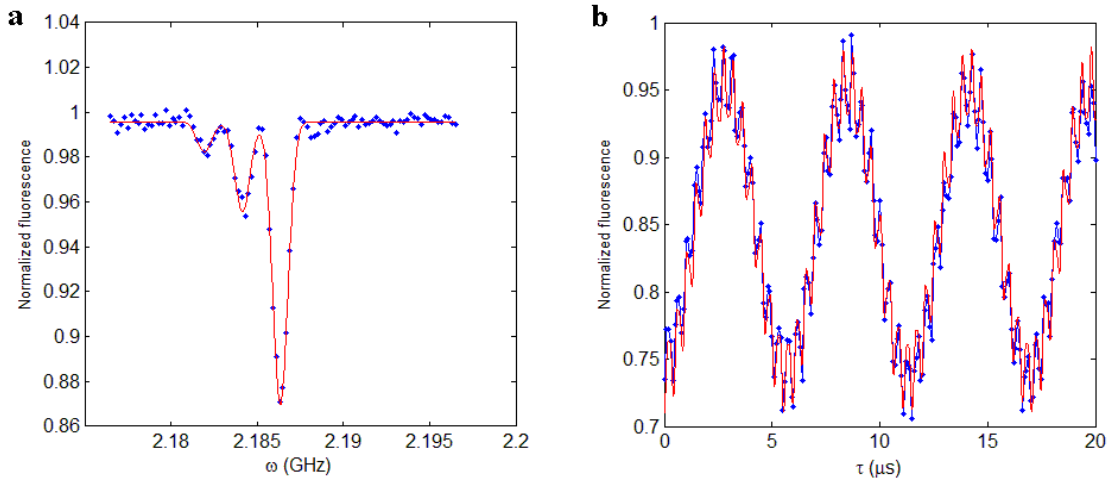

Figure B.3: **—- Dynamic Nuclear Polarization. a,** ESR scan of ^{14}NV^{-} center. **b,** Electron Ramsey experiment showing three beating frequencies of hyperfine transitions with significant polarization.

As discussed in the main text, our readout scheme relies on the acquisition of a phase

difference, depending on the nuclear spin state, in an electron Ramsey experiment over a free precession time τ. The fluorescence rate for this Ramsey experiment is given by

$$F_\tau(m_I, \delta) = f^0 - (f^0 - f^1)\frac{1 + e^{-\tau/T_2^*}\cos\left((\delta + m_I A_\parallel)\tau\right)}{2}, \tag{B.5}$$

where $f^{0(1)}$ denotes the fluorescence rate of the electronic spin of the NV center in the $m_s = 0(1)$ state, $A_\parallel$ the parallel component of the hyperfine interaction, m_I the spin projection of the ^{13}C nuclear spin ($m_I = \pm^1/_2$), δ the detuning of the microwave field from resonance and T_2^* the coherence time of the electronic spin.

In our readout, we set the Ramsey precession time τ to $\tau = \frac{\pi}{A_\parallel}$. The fluorescence rate for the readout then simplifies to

$$F(m_I, \delta) = \frac{f^0 + f^1}{2} + e^{-\tau/T_2^*}(f^0 - f^1)m_I \sin\left(\frac{\delta}{A_\parallel}\pi\right). \tag{B.6}$$

The readout signal of the nuclear spin state is therefore modified by an additional factor of $\sin(\pi\delta/A_\parallel)$. Since in our experiment $A_\parallel = (2\pi)2.7$ kHz, resonance frequency drifts of only a kilohertz are sufficient to affect the readout contrast and hence reduce the readout fidelity. Indeed, we observe fluctuations of the readout contrast on a timescale of $\sim$ 30 min as shown in Fig. B.1. One source for such drifts likely originates from the strong temperature dependence of the zero field splitting of NV$^-$, which has been measured [45] to be around $(2\pi)74\ \frac{kHz}{K}$.

When $\delta(t)$ is unknown it is impossible to uniquely determine the orientation of the nuclear spin with respect to the external magnetic field. Nevertheless if the correlation time of $\delta(t)$ is much lager than the typical duration of an individual experiment we can still use our readout process to define a qubit state. We redefine for each experimental run the basis in which our nuclear spin is measured such that low (high) fluorescence corresponds to $|\downarrow\rangle$ ($|\uparrow\rangle$).

In general, a measurement consists of a repetitive readouts c_1, a pulse sequence and another repetitive readout c_2, where c_1 initializes the nuclear spin in a state $|s\rangle$ and c_2 reads out the nuclear spin after applying a pulse sequence. In Fig. **??**, additional repetitive readouts were performed in order to normalize the signal.

In Fig. 2.3, we measures the nuclear spin flip probability p induced by an RF π-pulse, as a function of frequency ω. In this experiment, we first initialize the nuclear spin to $|\downarrow\rangle$ via a projective measurement c_1 (See Fig. 2.3). After initialization, we apply an RF-pulse with frequency ω before reading it out in c_2. To normalize our data, we measure two additional references (c_3, c_4). The measurement c_3 initializes the nuclear spin to $|\downarrow(\uparrow)\rangle$ and c_4 reads it out. The RF induced transition probability p is then

$$p = \frac{\zeta_2^{\downarrow} - \zeta_4^{\downarrow}}{\zeta_4^{\uparrow} - \zeta_4^{\downarrow}}, \tag{B.7}$$

where ζ_i^s is the number of counted photons during readout c_i conditional on the nuclear spin being in $|s\rangle$.

The data in Fig. **??** are normalized in a similar fashion with an additional RF π-pulse prior to readout c_4. In addition, before reading out the nuclear spin with our single shot readout we incorporated waiting times of 10 s. This is necessary since heating due to dissipation of the laser reduces the readout contrast for measurement c_2 and hence reduces the fidelity.

Fig. 2.8 and Fig. 2.10 show the decay time for a Ramsey signal with (without) simultaneous green excitation. In these experiments, no references are measured. Therefore, we normalize the data such that the fitted curves start with full contrast. This is justified under the assumption that for zero duration of storage time no dephasing/decay occurs.

In Fig. 2.13 we performed a similar normalization by a constant factor. Using this

normalization we can reduce the data acquisition time by more than a factor of two (2 weeks of averaging) by removing the references and reducing the waiting time between laser excitation and readout. The results of this procedure agree well with the fidelity measured from process tomography where no such normalization is performed.

B.4 Nuclear Coherence and Depolarization

In this part of the supplementary information we will use the spin-fluctuator model to obtain the dephasing and depolarization rates of the nuclear spin under green illumination. The spin-fluctuator model consists of the nuclear qubit (spin) and the NV electron environment (fluctuator). The nuclear spin evolves coherently while the fluctuator undergoes incoherent stochastic transitions between different levels. Such evolution of the fluctuator induces decoherence of the spin.

We will first study a simple spin-fluctuator model, for which we can obtain analytic expressions for the nuclear spin dephasing and depolarization rates that qualitatively explain the experimental data. Then, we consider a specific model with 11 levels for fluctuator dynamics, which can be solved using master equations and compared with the experimental data.

B.4.1 Spin-fluctuator model

The Hamiltonian associated with the nuclear spin is

$$H_n = (\gamma_{^{13}C} B)\hat{I}_z + \sum_{\alpha,\beta=x,y,z} A_{\alpha,\beta}\hat{S}_\alpha \hat{I}_\beta \tag{B.8}$$

which consists of the Zeeman splitting due to external magnetic field ($\gamma_{^{13}C}B$) and the dipole interaction with the electronic spin ($A_{\alpha,\beta}$). In this simple model we assume that under strong green illumination the electronic spin fluctuates between the states $m_s = \pm\frac{1}{2}$. We approximate the effective Hamiltonian as

$$H_n = (\gamma_{^{13}C}B)\hat{I}_z + f(t)\sum_{\beta=x,y,z} A_{z,\beta}\hat{I}_\beta, \tag{B.9}$$

where we replaced $\hat{S}_z$ by the time-dependent gaussian stochastic variable $f(t) = \{-\frac{1}{2}, \frac{1}{2}\}$ described by a Bernoulli process and neglected other terms associated with $\hat{S}_x$ and $\hat{S}_y$. For simplicity, we assume that $\langle f(t)\rangle = 0$ and the correlation function is

$$\langle f(t)f(0)\rangle = \left\langle f^2(0)\right\rangle e^{-2\gamma|t|} = \frac{1}{4}e^{-2\gamma|t|}, \tag{B.10}$$

where γ is the forward/backward effective transition rate controlled by the laser intensity.

We may rewrite the Hamiltonian as

$$H_n = (\gamma_{^{13}C}B)\hat{I}_z + f(t)\left(A_{z,z|}\hat{I}_z + A_{z+}\hat{I}_+ + A_{z-}\hat{I}_-\right) \tag{B.11}$$

with $\hat{I}_\pm = (I_x \pm iI_y)$ and $A_{z,\pm}\left(= A^*_{z,\mp}\right) = (A_{z,x} \mp iA_{z,y})/2$.

Dephasing. We can estimate the nuclear spin dephasing rate (T_2 process) induced by the terms $A_{z,z}(t)\,\hat{I}_z$. For time T, the random phase accumulated by the nuclear spin is given by $\Phi_{FID} = \int_0^T A_{z,z}(t)\,dt$. Assuming Gaussian noise we can compute the expectation value of the nuclear coherence, we have

$$\langle e^{i\Phi_{FID}}\rangle = e^{-\frac{1}{2}\langle\Phi^2_{FID}\rangle} \approx e^{-T/T_{FID}}, \tag{B.12}$$

where

$$1/T_{FID} = \frac{A^2_\parallel}{8\gamma}, \tag{B.13}$$

because $\frac{1}{2}\langle\Phi_{FID}^2\rangle = \frac{1}{2}\int_0^T dt \int_0^T dt' A_{z,z}^2 \langle f(t)f(t')\rangle \approx \frac{1}{2}\int_0^T dt \int_{-\infty}^{\infty} d\tau A_{z,z}^2 \langle f(\tau)f(0)\rangle = \frac{A_{z,z}^2}{8\gamma}T$ and $A_{\|} = A_{z,z}$. For our system, γ increases with the laser intensity, and consequently T_{FID} increases with the laser intensity, which is related to the motional averaging effect in NMR.

Depolarization. We can estimate the nuclear spin depolarization rate (T_1 process) induced by the terms $f(t)\left(A_{z,+}\hat{I}_+ + A_{z,-}\hat{I}_-\right)$. Noting that $|A_{z,+}| = |A_{z,-}| \equiv: A_\perp/2$, we can re-express the noise as, $A_\perp f(t) I_x$. First order time-dependent perturbation theory yields the transition rates in the two directions as [114]:

$$\Gamma_\uparrow = \left(\frac{A_\perp}{2}\right)^2 S_q(-\gamma_{^{13}C}B) \quad \text{and} \quad \Gamma_\downarrow = \left(\frac{A_\perp}{2}\right)^2 S_q(\gamma_{^{13}C}B) \tag{B.14}$$

where $S_q(\omega)$ is the noise spectral density. Assuming classical telegraph noise, $\Gamma_\uparrow = \Gamma_\downarrow = \frac{A_\perp^2}{16}\frac{\gamma}{\left(\gamma_{^{13}C}B/2\right)^2+\gamma^2}$, yielding a depolarization rate,

$$1/T_{1n} = \Gamma_\uparrow + \Gamma_\downarrow = \frac{A_\perp^2}{8}\frac{\gamma}{\left(\gamma_{^{13}C}B/2\right)^2+\gamma^2}. \tag{B.15}$$

Depolarization in the dark. Without laser excitation, the nuclear spin lifetime is no longer limited by the optically induced depolarization given in eq. (B.15). Instead, in this regime, the dominant contribution to T_{1n} is expected to be coherent dipole-dipole interactions, $H_{dd} = D_{dd}\left(3(\mathbf{I}\cdot\mathbf{n})(\mathbf{I}'\cdot\mathbf{n}) - \mathbf{I}\cdot\mathbf{I}'\right)$ between the memory spin $\mathbf{I}$ and neighboring ^{13}C nuclear spins $\mathbf{I}'$. In our present experiment D_{dd} is on the order of 1 Hz. However, when the dephasing rate of the nuclear spin is much large than that of coherent interactions (D_{dd}), spin-flips are suppressed. In this case, commonly denoted as the quantum-Zeno effect [115], the nuclear polarization, $n_\uparrow$, is characterized by an exponential decay as a function of time,

$$n_\uparrow(t) = \frac{1}{2}\left(1 + \exp(-\frac{(D_{dd}/(2\pi))^2}{1/T_{1e}}t)\right). \tag{B.16}$$

The measurement in Fig. B.4 depicts the nuclear spin dependent fluorescence rate as a function of waiting time t between initialization and readout. The data indicate that for $t < 3$ min no noticeable decay in the nuclear spin polarization is evinced.

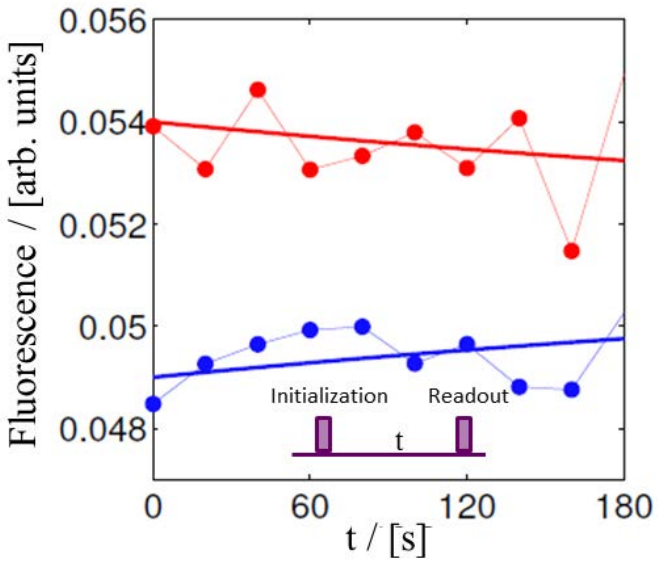

Figure B.4: **—- T_{1n} time of the ^{13}C nuclear spin in the dark** Blue (red) data points correspond to the fluorescence for the nuclear spin initialized to $|\downarrow\rangle(|\uparrow\rangle)$ and waiting time t. The solid lines indicate the nuclear polarization predicted by eq. (B.16) with $D_{dd} = (2\pi)0.5$ Hz.

B.4.2 Detailed Model

While the above simplified model captures the basic idea of the motional averaging in our system the discussed two level scheme is an oversimplification in the case of NV centers. To discuss the effects of an applied optical drive to the full extent we choose a different approach. For this we incorporate 11 levels for the electronic state and the two levels for the ^{13}C nuclear spin as shown in Fig. B.5. Using a master equation we can simulate the nuclear decoherence. For the numerical solution of the master equation we

assumed a secular approximation for the nuclear and electronic spin leaving us with an effective Hamiltonian for the hyperfine interaction $H_{hyp} = \left(A_{\parallel} I_z + A_{\perp} I_x\right) S_z$, which is justified since $A << g_e \mu_B B$. Moreover, we neglect any coherence between electronic states since all our fields are classical.

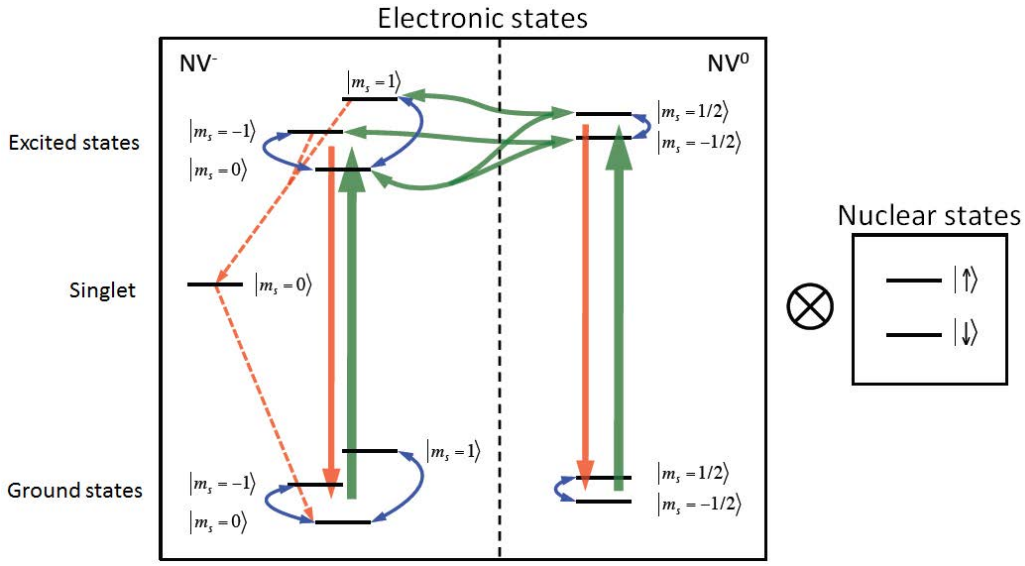

Figure B.5: **—- Schematic level diagram** for an NV center (left box) and a ^{13}C nuclear spin (right box) under illumination with green laser light. The green arrows indicate optical transitions addressed by our green laser pulse, red arrows show electronic decay and blue arrows indicate depolarization of the electronic spin. The transition rates for NV$^-$ employed in our model are taken from ref [116] with the decay rate from the electronic excited state to the ground state $\tilde{\gamma} = \frac{1}{13\ ns}$, the decay rate from the singlet to $m_s = 0$ of the electronic ground state $\Gamma = \frac{1}{300\ ns}$ and the decay rate from the electronic excited state with $m_s = \pm 1$ to the singlet $\tilde{\gamma_b} = 0.3\tilde{\gamma}$. Moreover we assumed the decay rate of the excited state of NV^0 to be on the same order as for NV$^-$. The deionization rate from NV$^-$ to NV^0 is taken to be $\gamma_1 = \frac{I/I_{sat}}{70\ ns}$ and the ionization rate $\gamma_2 = 2\gamma_1$. The depolarization time for the electronic spin for NV$^-$ is taken to be $T_{1e}^{NV-} = 8ms$ and for the case of NV^0 $T_{1e}^{NV0} = 6us$ [44]. All the remaining rates are takes to be zero.

A solution of the master equation for the nuclear coherence time is shown in Fig. B.6a. As expected the coherence time scales linearly as a function of laser intensity when exceeding optical saturation. Furthermore at small laser intensities ($I \sim I_{sat}/1000$, with I_{sat}

the saturation intensity) the coherence time has a local maximum originating from repolarization of the electronic spin without deionizing the NV center. This is possible to a certain extent since the (de)ionization process is a two photon process but the repolarization rate is linear in laser intensities for $I << I_{sat}$.

Even though the simplified two level model is able to qualitatively explain the linear scaling of the coherence as a function of laser intensity it does not quantitatively reproduce the T_2 (dashed-dotted black line). The deviation from the two level model originates from the fact that at large laser intensities other states beside the $m_s = 0$ and $m_s = \pm 1/2$ can be occupied.

Next we compare the solution of the master equation with the slope extracted from the experimental data in Fig. 2.12. The slope is shown in Fig. B.6a by a dashed red line. The experimental data is in excellent agreement with the simulation based on the transition rates given in the caption of Fig. B.5 .

Since we know that this master equation allows us to quantitatively reproduce T_{2n} we can use the master equation to estimate a value for the perpendicular component of the hyperfine interaction $A_\perp$. Optimizing our fit we can find $A_\perp$ to be on the order of $(2\pi)1.8$ kHz as shown in Fig. B.6b. Except for laser intensities $<< I_{sat}$ the simulated T_{1n} times agree well with the measured data. Plugging $A_\perp = (2\pi)1.8$ kHz into the two level model in eq. (B.15) yields a theoretical curve (black dashed-dotted line) showing a significant discrepancy with the measured data. If we neglect the contact term [117] of the hyperfine interaction A and assume only dipolar interaction we can estimate the distance between the electronic spin and the nuclear spin to be approximately 1.7 nm.

Nevertheless, our simplified two level model from eq. (B.13) and (B.15) allows us by

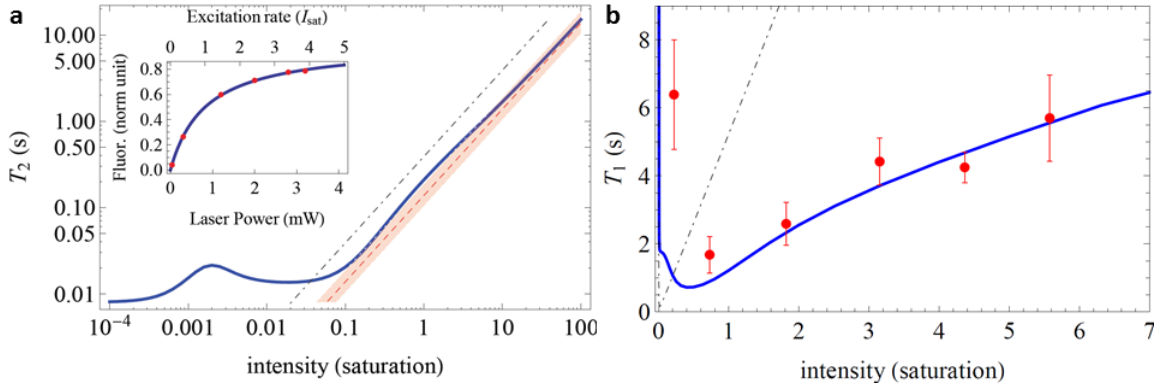

Figure B.6: **—- Coherence and T_{1n} time of the ^{13}C nuclear spin** Solution of a master equation (blue) employing the level scheme and transition rates shown in Fig. B.5. **a** The initial slope extracted from the measured data is represented by the red dashed line with error bars (red area). To convert the measured slope from Fig. 3 of the main text from laser power (mW) to intensity in units of I_{sat} the saturation curve shown in the inset is used. The dahsed-dotted black line is the eq. (B.13) with $A_{\parallel} = (2\pi)2.7$ kHz. **b** The red points show the measured nuclear T_{1n} times. The dashed-dotted black line is the solution of eq. (B.15) with γ same as is the inset of **a** and $A_{\perp} = (2\pi)1.8$ kHz. The simulated blue line uses $A_{\perp}$ as a fitting parameter.

rescaling the hyperfine interaction and the (de)ionization rate γ to find effective rates that quantitatively reproduce the T_{1n} and T_{2n} times. As shown in Fig. 2.7 and Fig. 2.12 using the rates $A_{\parallel}^{\text{eff}} = (2\pi)3.3$ kHz, $A_{\perp}^{\text{eff}} = (2\pi)1.0$ kHz and $\gamma = (2\pi)150 \times P_{\text{Laser}}$ kHz/mW reproduce the measured T_{1n} and T_{2n} as function of the laser power P_{Laser}.

B.5 Nuclear Decoherence under Dynamical Decoupling

Figure 2.12 showed that the nuclear coherence time is significantly extended under the application of MREV-8, which suppresses the nuclear dipole-dipole interaction. Here we provide further details on MREV-8 and identify the sources of residual decoherence.

B.5.1 MREV-8 Dynamical Decoupling

The Waungh, Huber and Haberlen four-pulse sequence (WHH), shown in Fig B.7, decouples nuclear dipole-dipole interactions [118]. In our experiment we use the MREV-8 sequence, shown in Fig B.7, which is an eight-pulse sequence made up of WHH cycles of alternating phase.

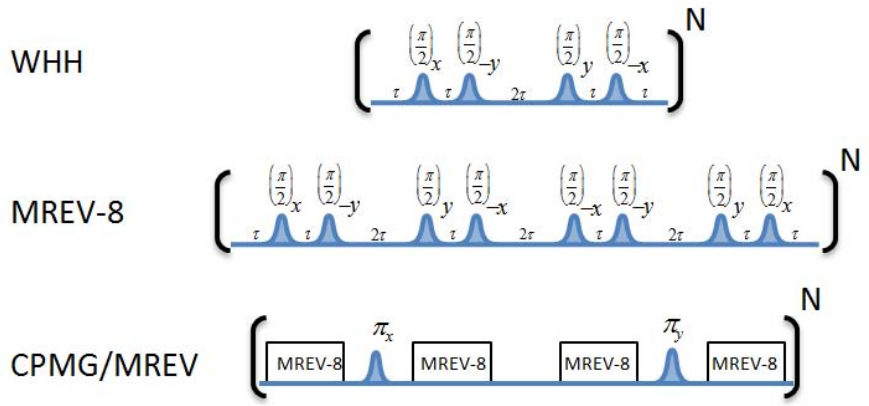

Figure B.7: **—- Pulse sequences for decoupling** WHH sequence, showing four RF pulses around the indicated axes for dipole-dipole decoupling. MREV-8 sequence used for increased robustness against pulse errors in WHH. CPMG/MREV sequence adds decoupling from external magnetic field due to additional π-pulses.

The effect of MREV-8 on the dipole-dipole interaction can be understood using average Hamiltonian theory [118]. We describe the effects of the pulses by moving to an interaction picture (i.e. the toggling frame) with respect to the Hamiltonian defined by the $\pi/2$ rotations. Provided the characteristic frequencies ω of H satisfy $\omega t \ll 1$ we can perform a Magnus expansion, and describe the total time evolution during the cycle is described by an effective Hamiltonian,

$$H_{\text{eff}} = H^{(0)} + H^{(1)} + H^{(2)} + ... \tag{B.17}$$

where the first few terms are

$$H^{(0)} = \sum_{j=1}^{M} H_j, \tag{B.18}$$

$$H^{(1)} = \frac{-i\tau}{2M} \sum_{k>j}^{M} \sum_{j=1}^{M} \left[H_k, H_j\right]. \tag{B.19}$$

Here, M is the total number of time intervals of length τ between pulses as shown in Fig B.7, and H_j is the interaction picture Hamiltonian in the toggling frame in interval j. The zeroth order effective Hamiltonian is just the average over the cycle in the toggling frame, and the nth terms in the expansion consist of nested commutators of order n.

Our goal is to find the effect of MREV-8 on the nuclear dipole-dipole interaction within secular approximation,

$$H_{\mathrm{D}} = \sum_{j>k} D_{jk} \left(3 I_j^z I_k^z - \mathbf{I}_j \cdot \mathbf{I}_k\right), \tag{B.20}$$

where the dipolar coupling frequency is $D_{jk} = \hbar^2 \gamma_n^2 \left[1 - 3\cos^2(\theta_{ij})\right] / r_{ij}^3$, and the memory nuclear spin is indexed by $j = 0$. The effective, average Hamiltonian is obtained in terms of the zeroth order effective spin operators under MREV-8,

$$I_x^{(0)} = \frac{2}{3} I_x \qquad I_y^{(0)} = \frac{1}{3} I_y \qquad I_z^{(0)} = \frac{1}{3} \left(I_x + I_z\right). \tag{B.21}$$

Applying Eq. (B.21) to each nuclear spin, one immediately finds that the average dipole-dipole Hamiltonian is $H_D^{(0)} = 0$. Furthermore, from the first order term in the Magnus expansion of Eq. (B.18) one finds that there is no first order correction, i.e. $H_D^{(1)} = 0$. Thus the leading order correction from the dipolar interaction is$(D\tau)^2 D \sim 10^{-4}$ Hz. Due to this very high suppression we expect that nuclear dipolar coupling alone cannot account for the residual decoherence when MREV-8 is applied. Next we discuss the sources of residual decoherence in the limits of low and high laser power.

B.5.2 Effect of MREV-8 on Decoherence from NV Ionization

At low laser power, nuclear decoherence is dominated by the (de)ionization of the NV electronic spin as described by the fluctuator model in Section B.4. Here we find the effect of MREV-8 on this source of decoherence; for simplicity we consider a simple two-state model. Within this model, the Hamiltonian of the nuclear memory spin is

$$H_A = f(t)\left[A_\parallel I_z + A_\perp \left(I_x \cos\phi + I_y \sin\phi\right)\right], \tag{B.22}$$

where $f(t)$ describes telegraph noise with switching rate γ. In the absence of MREV-8 it is straightforward to calculate the resulting decoherence. A Fermi's golden rule calculation yields the depolarization rate in the limit $\gamma \gg \omega_L$,

$$\Gamma_1 = \frac{1}{8\gamma} A_\perp^2, \tag{B.23}$$

which is set by the coefficients of I_x and I_y. We calculate the dephasing rate within the Gaussian approximation, justified since $A_\parallel \tau \ll 1$, yielding

$$\Gamma_\phi = \frac{1}{8\gamma} A_\parallel^2, \tag{B.24}$$

which is set by the coefficient of I_z.

Next we find how MREV-8 modifies the decoherence from NV ionization. Here we cannot apply average Hamiltonian theory because the Hamiltonian fluctuates rapidly between $\pi/2$ pulses. Nonetheless, we can make use of the fast switching rate, since in the relevant limit $\gamma\tau \gg 1$, the fluctuations $f(t)$ are uncorrelated between one interval and the next. As a result, the total decoherence rate during one cycle is simply the incoherent average of the decoherence rates during each interval. The total dephasing rate is thus $\Gamma_\phi = \frac{1}{M}\sum_j^M \Gamma_{\phi,j}$ and the depolarization rate is $\Gamma_1 = \frac{1}{M}\sum_j^M \Gamma_{1,j}$, where the rates during

each interval j are obtained from the Hamiltonian H_j in the toggling frame, and using the same calculations as described above in the absence of MREV-8. When MREV-8 is applied we obtain

$$\Gamma_\phi = \frac{1}{24\gamma}\left[A_\parallel^2 + 2A_\perp^2 \sin^2\phi\right], \tag{B.25}$$

$$\Gamma_1 = \frac{1}{24\gamma}\left[A_\perp^2 + 2\left(A_\parallel^2 + A_\perp^2 \cos^2\phi\right)\right]. \tag{B.26}$$

The coefficients which previously led to pure dephasing or depolarization become mixed due to the $\pi/2$ rotations of MREV-8.

The total transverse decoherence rate $\Gamma_2 = 1/T_2$ includes contributions from both dephasing and depolarization, and can be approximated by $\Gamma_2 = \frac{1}{2}\Gamma_1 + \Gamma_\phi$. From the above results the total decoherence rates with and without MREV-8 are

$$\Gamma_2 = \frac{1}{8\gamma}\left[A_\parallel^2 + \frac{1}{2}A_\perp^2\right] \qquad \text{(without MREV-8)} \tag{B.27}$$

$$\Gamma_2 = \frac{1}{8\gamma}\left[\frac{2}{3}A_\parallel^2 + \frac{1}{2}A_\perp^2\left(1 + \frac{2}{3}\sin^2\phi\right)\right] \qquad \text{(with MREV-8)} \tag{B.28}$$

From the fit of our T_1 data (see Fig. 2.7) we found $A_\perp/2\pi \sim 1.0$ kHz and $\gamma/2\pi \sim 300$ kHz. Using this value of γ, our T_2 data (see Fig. 2.12) this yields $A_\parallel/2\pi \sim 3.3$ kHz. Inserting these values into Eqs. (B.27) and (B.28) we find that the slope of T_2 versus laser power, at low power, is expected to be a factor $\sim 3/2$ larger when MREV-8 is applied. This simple estimate predicts that the decoherence from NV ionization is only slightly affected by MREV-8, in qualitative agreement with the data (see Fig. 2.12). However, the data shows that the impact of MREV-8 on the decoherence at low power is even smaller than the above prediction. This implies that in practice the total decoherence is slightly larger than obtained by incoherently averaging over each time interval, and as a result MREV-8 has almost no impact on the decoherence at low power.

B.5.3 Residual Decoherence due to finite Detuning

Lastly, we consider the residual decoherence under MREV-8 at high laser power where the ionization-induced decoherence is suppressed by motional averaging. As discussed above, decoherence due solely to the dipolar interaction is strongly suppressed by MREV-8, in particular the terms in the effective Hamiltonian to zeroth and first order in $D\tau$ vanish. However, the presence of small but finite detuning of our RF pulses leads to slightly imperfect dipolar cancelation; for the longest times measured, this small detuning is sufficient to reintroduce the dipolar Hamiltonian through cross terms. This combined effect appears at first and higher orders in the effective Hamiltonian and sets the limit on T_2 in the present experiment.

Before discussing the combined effect of detuning and dipolar coupling, we consider the possibility of decoherence due to the detuning alone, in the absence of the dipolar interaction. The frequency resolution of our RF pulses is $\sim$ 10 Hz, which means that a finite detuning of this order is expected. Constant detuning has no direct consequence since it is echoed out by the CPMG sequence in which MREV-8 is embedded. However, slow drifts in the detuning on the order of this frequency resolution could in principle lead to decoherence. From a measurement of $\delta(t)$ we estimate the rms fluctuation amplitude of $\delta_{\mathrm{rms}}/2\pi \sim 10$ Hz and correlation time of $T_c \sim 350$ s. Estimating the impact of MREV-8 using the zeroth order term in Eq. (B.18), we modify this by $\delta_{\mathrm{rms}} \rightarrow \delta_{\mathrm{rms}}/3$. Using these values and estimating $T_2 \sim \sqrt[3]{12N^{2/3}T_c(2\pi/\delta_{\mathrm{rms}})^2}$ for pure dephasing [72] we find $T_2 \sim 27$ s from the detuning fluctuations. This suggests that slow detuning fluctuations are not directly the cause of the observed residual decoherence.

We now turn to the combined effect of finite detuning and dipolar coupling which ap-

pears to dominate the residual decoherence observed at high laser power. Dipolar coupling is described by Eq. (B.20), and the Hamiltonian due to finite detuning δ is

$$H_\delta = -\delta \sum_j I_z^j \tag{B.29}$$

in the frame rotating at the RF frequency. Applying the Magnus expansion of Eq. (B.18) the nth term in the effective Hamiltonian contains frequencies of order

$$\omega_n = [(\delta + D)\tau]^n (\delta + D). \tag{B.30}$$

For the longest coherence times measured, the interval between $\pi/2$ pulses is $\tau_{\max} \sim 20$ ms, which yields $\delta\tau_{\max} \sim 1$. Accordingly, we can no longer truncate the Magnus expansion to low order; specifically, the terms $(\delta\tau)^n D$ contribute to high order. This is the most important term, because terms involving only δ are echoed out by CPMG. Thus the effective decoherence time is set by the value of τ for which $\delta\tau \sim 1$. We have performed a simple numerical calculation to support this conclusion. In Fig. B.8 we show the signal calculated using parameters provided in the caption. We obtain an effective $T_2 \sim 2$ s, in good agreement with the experiment.

B.5.4 Limits to Coherence Time

The lifetime of our proposed nuclear spin quantum memory is limited by a combination of optically induced dephasing, Γ_{opt} (eq. B.13), and interactions with the remaining spins in the surrounding ^{13}C environment, Γ_{bath}. Since Γ_{opt} is proportional to A^2, a slight reduction in strength of the hyperfine interaction increases the coherence time significantly. Upon reducing the ^{13}C concentration by an order of magnitude, it is possible to initialize

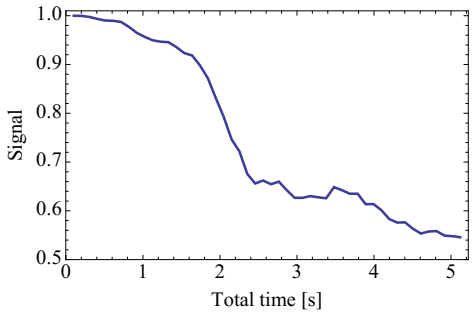

Figure B.8: Signal calculated numerically for 5 bath nuclear spins distributed around the central nuclear spin, assuming 0.01% ^{13}C nuclear spins in the diamond lattice. We assumed constant detuning $\delta/2\pi = 10$ Hz, and averaged over 50 random placements of the surrounding.

and readout a nuclear spin coupled with strength, $A \sim (2\pi)0.5$ kHz. Furthermore, lowering the ^{13}C concentration will also result in a reduction of the nuclear-nuclear induced decoherence, that scales quadratically with the ^{13}C concentration.

As discussed in the maintext, the use of even higher laser intensities in our present setup is limited by heating of the diamond sample, which causes drifts in the ESR transition. However, by increasing the laser intensity while simultaneously cooling the diamond sample, it is possible to further enhance the coherence time. Finally, by decoupling the memory nuclear spin from the environment via composite MREV-8 pulses, we can suppress dipole-dipole interactions with the spin bath by up to three order of magnitudes [4]. The expected coherence time for this process as a function of ^{13}C concentration and laser power is plotted in Fig. B.9, where we have assumed that heating is suppressed by feedback cooling. As shown, coherence times exceeding 1 min are easily achievable, while coherence times in the range of 1 hour are eminently feasible.

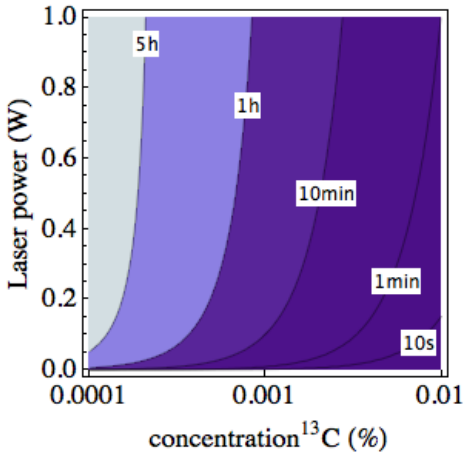

Figure B.9: **—- Estimated nuclear coherence time** as a function of laser power and ^{13}C concentration. The hyperfine interaction is chosen to scale proportionally to the ^{13}C concentration.

B.6 Process Tomography and Fidelity

In this section we will in detail discuss how the performance of our memory is measured. For this we will first explain the way we characterize the system's evolution using process tomography. Finally we will discuss our quantum memory in terms of fidelity.

To analyze the performance of our quantum memory we are interested in the full evolution of the ^{13}C nuclear spin during the storage process. One way to fully characterize the system's evolution $\mathcal{E}(\rho)$ is given by the Kraus map

$$\mathcal{E}(\rho) = \sum_{i,j=0}^{d^2-1} \chi_{i,j}(t) A_i \rho A_j^\dagger, \tag{B.31}$$

with ρ being the density matrix describing our ^{13}C nuclear memory, A_i a basis of operators acting on ρ and $d = 2$ the dimension of our system. The matrix χ is positive hermitian, time dependent and fulfills the trace-preservation relation $\mathbb{1} = \sum_{i,j} \chi_{i,j} A_i A_j^\dagger$.

For $d = 2$ we have to determine 12 parameters which determine χ. Process tomography

is a tool to measure these parameters by preparing the nuclear spin in 4 different basis states ($|\downarrow\rangle$, $|x\rangle$, $|y\rangle$ and $|\uparrow\rangle$, with $|x\rangle = (|\downarrow\rangle + |\uparrow\rangle)/\sqrt{2}$ and $|y\rangle = (|\downarrow\rangle + i|\uparrow\rangle)/\sqrt{2}$) followed by a state tomography after a certain storage time (Fig. B.10)

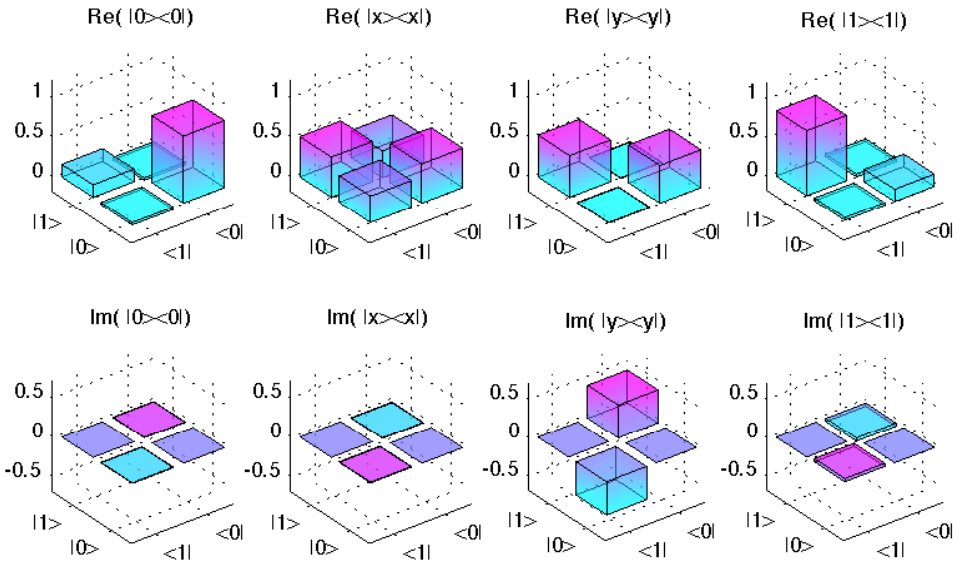

Figure B.10: **—- State tomography** The states shown in the figure are $|\downarrow\rangle$, $|x\rangle$, $|y\rangle$ and $|\uparrow\rangle$ after 1 s of storage time.

For the given states, we can reconstruct a matrix $\tilde{\chi}$ that fulfills the Kraus map from eq. (B.31). In the basis $A_i = \{\mathbb{1}, \sigma_x, \sigma_y, \sigma_z\}$ the matrix $\tilde{\chi}$ can be reconstructed by using the linearity of $\mathcal{E}$ and the identity

$$\begin{aligned}
\rho_1' &= \mathcal{E}(|\downarrow\rangle\langle\downarrow|)\ ;\ \rho_4' = \mathcal{E}(|\uparrow\rangle\langle\uparrow|) \\
\rho_2' &= \mathcal{E}\left(|x\rangle\langle x| - i|y\rangle\langle y|\right) - \frac{(1-i)}{2}(\rho_1' + \rho_4') \\
\rho_3' &= \mathcal{E}\left(|x\rangle\langle x| + i|y\rangle\langle y|\right) - \frac{(1+i)}{2}(\rho_1' + \rho_4') \\
\tilde{\chi} &= \frac{1}{4}\begin{pmatrix} \mathbb{1} & \sigma_x \\ \sigma_x & -\mathbb{1} \end{pmatrix}\begin{pmatrix} \rho_1' & \rho_2' \\ \rho_3' & \rho_4' \end{pmatrix}\begin{pmatrix} \mathbb{1} & \sigma_x \\ \sigma_x & -\mathbb{1} \end{pmatrix},
\end{aligned} \tag{B.32}$$

which are outlined in [119].

However, the $\tilde{\chi}$ matrix derived this way does not necessarily describe a physical process since a noisy signal may produce a $\tilde{\chi}$ that does not satisfy hermiticity and completeness. To find a χ that satisfies these requirements we apply a most likelihood procedure. This allows us to find a χ which is most likely to produce the observed experimental signal p (A description of this procedure is given in [120]). In the most likelihood estimation we parametrized χ by $\chi(\overrightarrow{q})$ to ensure non-negativity and hermiticity[121].

$$\chi(\overrightarrow{q}) = \frac{Q^\dagger Q}{Tr\left[Q^\dagger Q\right]}, \text{ with } Q = \begin{pmatrix} q_1 & 0 & 0 & 0 \\ q_5 + iq_6 & q_2 & 0 & 0 \\ q_{11} + iq_{12} & q_7 + iq_8 & q_3 & 0 \\ q_{15} + iq_{16} & q_{13} + iq_{14} & q_9 + iq_{10} & q_4 \end{pmatrix} \tag{B.33}$$

Using this parametrization for χ we can now minimize the square residual function defined by

$$\begin{aligned} S(\overrightarrow{q}) = \sum_{a=1}^{d^2} \sum_{b=1}^{d^2-1} \left(p_{a,b} - \sum_{n,m=0}^{d^2-1} \chi_{n,m}(\overrightarrow{q}) \langle \varphi_b | A_n | \phi_a \rangle \langle \phi_a | A_m^\dagger | \varphi_b \rangle \right)^2 \\ + \lambda \left(\sum_{m,n,k=0}^{d^2-1} \chi_{n,m}(\overrightarrow{q}) Tr\left(A_m A_k A_n\right) - \delta_{k,0} \right), \end{aligned} \tag{B.34}$$

where $p_{a,b}$ denotes the measurement outcome for a state prepared in $|\phi_a\rangle$ ($|\phi_a\rangle = \{|\downarrow\rangle,\ |\uparrow\rangle,\ |x\rangle,\ |y\rangle\}$) and projected on $|\varphi_b\rangle$ ($|\varphi_b\rangle = \{|\downarrow\rangle,\ |x\rangle,\ |y\rangle\}$). The second part of the formula constrains $\chi(\overrightarrow{q})$ to be completely positive, with λ a parameter to describe the degree of positivity (a way to find a good starting point $\overrightarrow{q}_0$ is described in ref. [121]).

Using this most likelihood procedure we can find a χ matrix

$$\chi = \begin{pmatrix} 0.81 & -.02i & -0.01-0.01i & -0.01i \\ 0.02i & 0.02 & 0 & 0.02+0.01i \\ -0.01+0.01i & 0 & 0.14 & 0 \\ 0.01i & 0.02-0.01i & 0 & 0.03 \end{pmatrix}. \tag{B.35}$$

that is associated with our experimental observations. By using a Monte Carlo simulation we can estimate the error bars associated with the χ matrix found from our most likelihood procedure

$$\delta\chi = \begin{pmatrix} 0.08 & 0.01+0.04i & 0.01+0.01i & 0.01+0.02i \\ 0.01-0.04i & 0.06 & 0.01+0.01i & 0.01+0.01i \\ 0.01-0.01i & 0.01-0.01i & 0.04 & 0.01+0.01i \\ 0.01-0.02i & 0.01-0.01i & 0.01-0.01i & 0.04 \end{pmatrix}. \tag{B.36}$$

For this χ matrix all the off diagonal elements are zero within the error bars indicating that $\{\mathbb{1}, \sigma_x, \sigma_y, \sigma_z\}$ is a eigen-basis. In this form the Kraus operators have the physical interpretation of quantum channels. That the largest contribution in χ with $(81 \pm 8)\%$ is associated with the identity $\mathbb{1}$ as expected for a memory. The error channels are $(14 \pm 4)\%$ for phase-bit flip error σ_y, $(2 \pm 6)\%$ for bit flip σ_x and $(3 \pm 4)\%$ for phase flip σ_z error. In the case of only a depolarization channel one would expect an equal distribution between σ_x, σ_y and σ_z. This mismatch can be explained by taking a finite detuning in the RF transition frequency and the fixed chirality of the MREV-8 sequence into consideration.

As discussed in [122] diagonalizing χ allows us to extract a master equation under the assumption that the noise environment is Markovian. The average fidelity calculated based on the solution of the master equation is shown in B.12. The results of the extracted master equation are in agreement with the recorded data (blue points) within statistical errors.

The process fidelity F_p associated with the Kraus map χ is defined [120] by $F_p = \mathrm{Tr}(\chi \cdot \chi_{id}) = \chi_{00}$, where χ_{id} is the process matrix representing the identity. Using the relationship [123] between process fidelity F_p and average fidelity $\overline{F} = (d \cdot F_p + 1)/(d+1)$ we find $\overline{F} = (87 \pm 5)\ \%$.

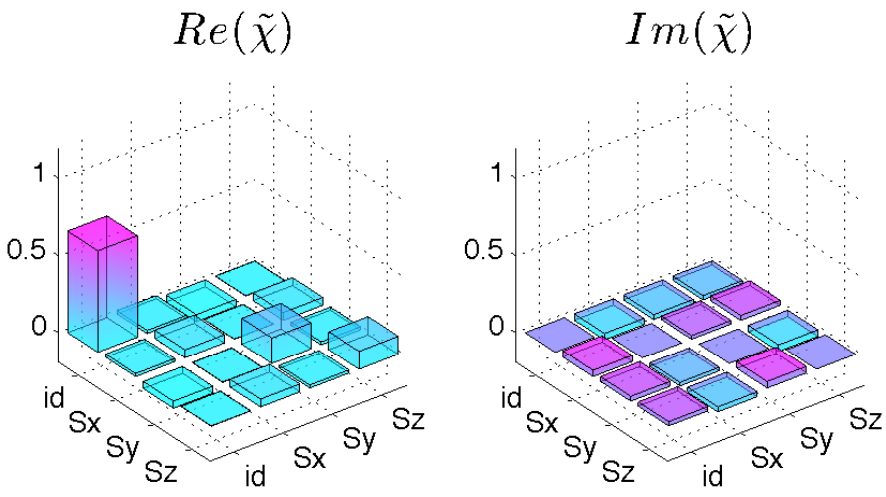

Figure B.11: **—- Estimated $\tilde{\chi}$ matrix** Initial reconstruction of the $\tilde{\chi}$ matrix.

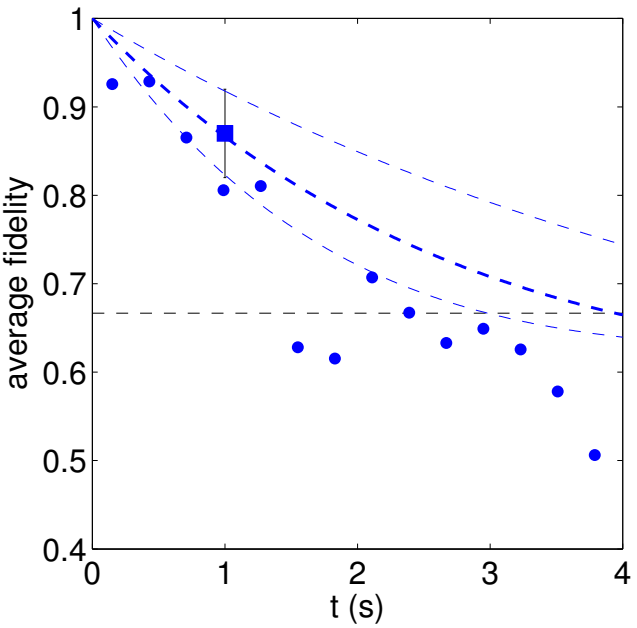

Figure B.12: **—- Solution of master equation** The blue points are the measured average fidelity from Fig. 2.13. The blue square represents the average fidelity calculated from the χ matrix. The blue dashed line is the average fidelity extracted from the master equation corresponding to blue square.

Appendix C

Supporting Material of Chapter 3

C.1 Experimental Apparatus, Sensitivity and Accuracy

Our experimental apparatus consists of a confocal microscope with two independent excitation/collection paths allowing measurement and heating at two independent locations simultaneously. The experiments use either a Nikon Plan Fluor 100x oil immersion, NA = 1.3, (nanodiamonds) or a Nikon Plan Apo 100x air, NA = 0.95, objective (bulk sample), resulting in $C \approx 0.03$, which can be further improved by employing a solid immersion lens or diamond nano patterning. Microwaves are delivered via a lithographically defined coplanar waveguide on top of a glass coverslip. For experiments with nanodiamonds we use neutral density filters in the collection path to avoid saturation of the APD. The temperature accuracy δT for bulk diamond is estimated from the measurement shown in Fig. 2b. Using the standard deviation σ (shown error bars) we evaluate the accuracy as $\delta T = \sigma/(c\,\frac{d\Delta}{dT}\,2\tau)$, where c is the oscillation amplitude and 2τ is the free evolution time. We find that for integration times $t < 30\ s$ (limited by temperature stability) the temperature accuracy

improves as $\sqrt{t}$, giving a sensitivity $\eta = \delta T\sqrt{t}$. A linear dependence of the dissipated heat as a function of laser power (Fig. 3b) is used to determine the measurement accuracy for NDs. A linear function, with slope m, is fitted to the data (red dashed line) and the measurement accuracy is given by $\delta T = \sqrt{\frac{1}{N-1}\Sigma_{i=1}^{N}\left(T_i - m\ P_i\right)^2}$, with T_i the measured temperature and P_i the corresponding laser power. The error bars are evaluated as $\sigma\left(\delta T\right) = \delta T\sqrt{1 - \frac{2}{N-1}\frac{\Gamma^2(n/2)}{\Gamma^2((n-1)/2)}}$, where $\Gamma(\cdot)$ indicates the Gamma distribution.

C.1.1 Ultimate Sensitivity

The ultimate sensitivity of our method is limited by the NV coherence time and the number of defect centers. In our current experiment, we have demonstrated a sensitivity of 9 mK$/\sqrt{\text{Hz}}$ (with a free evolution time of 250 μs). Two natural extensions enable longer NV coherences: 1) decreasing the ^{13}C concentration to suppress the nuclear spin bath and 2) further dynamical decoupling. These methods can, in principle, allow us to extend the evolution time up to $T_1/2 \sim 3$ ms. In combination with a nanocrystal that contains ~ 1000 NV centers, this could yield an ultimate sensitivity limit of 80 μK$/\sqrt{\text{Hz}}$. Further improvement may be possible by employing spin squeezed states. Finally, the determination of absolute temperature is limited by variations of the zero-field splitting due to spatially varying strain. For low strain diamond samples, we find that the variation in the zero-field splitting is less than 60 kHz, allowing for sub-K absolute temperature determination. In addition, the use of an ensemble of NV centers in different NDs with uncorrelated strain values allows for a further increase in absolute sensitivity by a factor $\sqrt{n}$, where n is the number of NDs.

C.1.2 Ultimate Accuracy in Solution

In cases where our method is used to probe a system that is in solution (e.g. cells, chemical reactions), the primary accuracy limit is set by heat dissipation during the measurement process. In particular, the microwave spectroscopy used to detect changes in the NV zero-field splitting also induces heating of the solution. In the present experiment, we utilize a lithographically fabricated microwave loop (diameter 200 μm) to generate an ac-magnetic field, $B \approx 10$ mGauss, for spin manipulations. Estimating the effective dipole field created by the microwave loop shows that the solution (water) absorbs 10^{-6} W of power yielding a temperature increase of 5 mK in the steady state. By using a smaller microwave loop (20 μm) and reducing the duty cycle, it could be possible to decrease the heating of the solution to approximately 50 μK.

C.2 Optical Setup

The optical setup consists of a home-built confocal microscope with two independent scanning beams. Two separate green excitation/collection beams are used for simultaneous excitation of spatially separated nanoparticles [124]. One of the scanning beams is controlled by a galvo-scanner (Thorlabs GVC002); the other beam is controlled by a 3-axis piezoelectric stage (PI P-562.3CD). The collected light is transmitted through a dichroic mirror and filters before being focused onto an avalanche photo diode (APD). The samples measured in Chapter 3 are mounted on a microscope coverslip; in the case of biological samples, the cells are protected by a buffer solution housed in a PDMS ring (Fig. C.1).

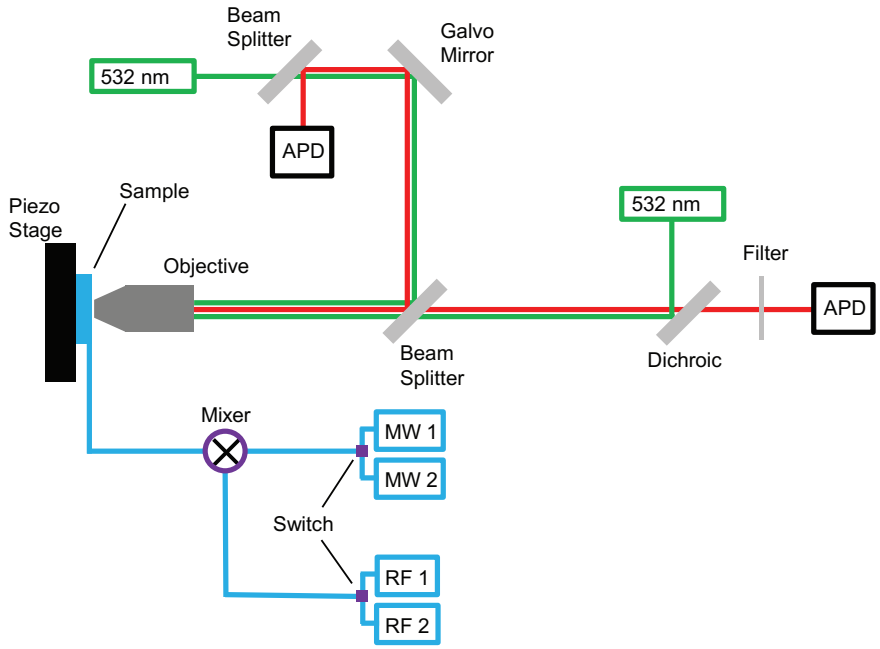

Figure C.1: **— Schematic Setup.** Depicts the optical (excitation: green, collection: red) path and microwave supply (blue). Each of the two excitation (collection) paths can be independently controlled using a combination of a galvo-mirror and a piezo. By controlling the MW switches, it is possible to interchange between four different MW frequencies on sub-microsecond time scale.

C.3 Microwave Setup

The microwave excitation of NV centers is achieved via a coplanar waveguide that is lithographically fabricated on top of the microscope coverslip. In the experiments shown in Chapter 3, CW microwave pulses at four different frequencies are applied in order to probe the fluorescence rate at different microwave frequencies. These microwave frequencies are created by mixing low frequency RF fields (200 and 202 MHz) with two different microwave carrier frequencies around 2.68 GHz. The actual pulse sequence is illustrated in Fig. C.4. To eliminate sensitivity to low frequency noise in the ND's photoluminescence,

the pulse sequence depicted in Fig. S5 is repeated at a 5 kHz sampling rate.

C.3.1 Nanodiamond Measurement Pulse Sequence

As indicated in Fig. 3a, we record the fluorescence at four different frequencies centered around $\Delta = 2.87$ GHz:

$f^{1,2} \approx f\left(\omega_{-}\right) + \frac{\partial f}{\partial \omega}|_{\omega-} \left(\mp\delta\omega + \delta B + \delta T \frac{d\Delta}{dT}\right)$ and $f^{3,4} \approx f\left(\omega_{+}\right) + \frac{\partial f}{\partial \omega}|_{\omega+} \left(\mp\delta\omega - \delta B + \delta T \frac{d\Delta}{dT}\right)$.

This allows us to determine the change in temperature,

$$\delta T = \frac{\delta\omega}{d\Delta/dT} \frac{(f^1 + f^2) - (f^3 + f^4)}{(f^1 - f^2) + (f^3 - f^4)}, \tag{C.1}$$

where $\omega_{\pm} \mp \delta\omega$ are the four microwave carrier frequencies and δB is a unknown static magnetic field. By averaging the fluorescence at these four frequencies as shown in equation (2), we are able to remove errors associated with changes in total fluorescence rate, ESR contrast, Rabi frequency and magnetic field.

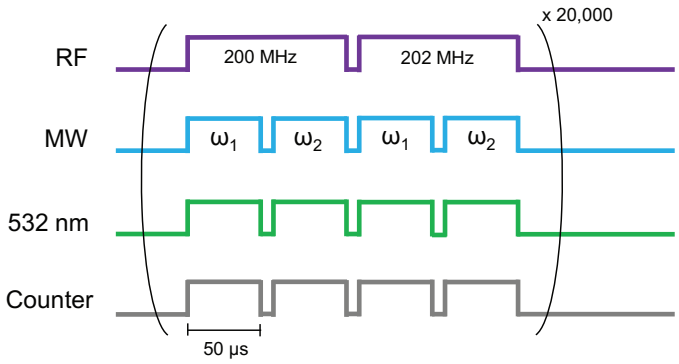

Figure C.2: **— Pulse sequence** used for the measurements of Chapter 3. The microwave (MW) frequencies ω_1 and ω_2 are chosen such that when mixed with 200 MHz and 202 MHz fields, four frequencies $f^1 = \omega_1 + 200$ MHz, $f^2 = \omega_1 + 202$ MHz, $f^3 = \omega_2 + 200$ MHz and $f^4 = \omega_2 + 202$ MHz around 2.87GHz are realized. Each pulse is 50 μs long and the entire sequence is repeated $20,000$ times.

C.4 Nanoparticle Localization

Under green excitation, the gold nanoparticles (Au NPs) used in the present work exhibit an emission spectrum which is slightly blue shifted relative to the NV spectrum (Fig. C.3). This allows us to use a frequency doubled YAG laser (532 nm) for excitation of both NV centers and Au NP. To distinguish the fluorescence of nanoparticles from NV centers, a 560 ± 25 nm band pass filter is used. By comparing scans with and without a band pass filter (Fig. C.4), it is possible to clearly identify the location of Au NPs. To verify the presence of a nanodiamond (ND), we utilize the electron spin resonance (ESR) response of NV centers; in particular, we measure changes to the photoluminescence under microwave excitation.

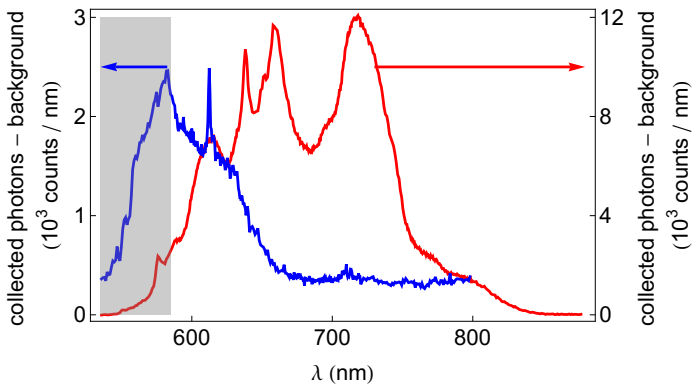

Figure C.3: **— Fluorescence spectrum** under green excitation of gold nanoparticles (blue data) and nanodiamonds (red data). The shaded region indicates the bandpass filter used for detection of gold. The arrows mark the respective y-axis scaling for each curve.

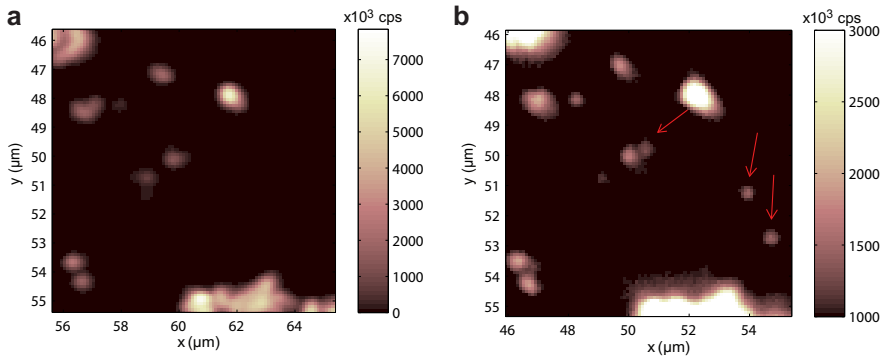

Figure C.4: **— Confocal image of nanoparticles. (a)** Confocal scan of Au NPs and NDs taken with a 633 nm longpass filter. **(b)** Scan of the same area using a 560 ± 25 nm bandpass filter. For visual clarity, a lower bound of 1000 kcps and an upper limit of 3000 kcps is set. The red arrows indicate locations of Au NPs.

C.5 Injection of Nanodiamonds into Cells

Nanodiamonds and Au NPs were introduced into WS1 cells via silicon nanowire-mediated delivery[75]. Silicon nanowires were treated with 3-amino- propyltrimethoxysilane to present NH_2 functionality on the surface, and nanodiamonds / Au NPs were subsequently attached via electrostatic binding. Afterwards, human embryonic fibroblast WS1 cells were plated on the silicon nanowire substrates and cultured overnight. The cells were removed by trypsin treatment and re-plated on a glass slide with lithographically defined strip lines for ESR measurements. The samples were stained with calcein-AM and ethidium homodimer-1 for the live/dead assay.

C.6 Global Temperature Control

To achieve a homogenous heating of the sample in our validation/calibration experiments, the sample mount is fabricated out of solid copper and is thermally isolated from

the rest of the experiment. A Peltier element is attached to the sample mount in order to control the temperature. The data in Fig. 3.5 of the main text was obtained by heating the sample mount (by 1K) and then subsequently cooling down after switching off the Peltier element. Thermal equilibrium is reached after approximately 1 hour. During the process of this equilibration, the measurement shown in Fig. 2 of the main text was recorded. The sample temperature (x-axis of Fig. 3.5) is independently recorded by a thermistor located on the sample mount immediately next to the diamond. Each data point is taken by first stabilizing the temperature of the mount through an attached Peltier element. After stabilization, the shift of the NV zero-field splitting is measured.

Appendix D

Supporting Material of Chapter 4

D.1 Materials and Methods

D.1.1 Sample Fabrication

The diamond sample used in this work is grown by chemical vapor deposition (CVD). During the CVD process, nitrogen is incorporated into the diamond lattice, resulting in a concentration of $\sim$100 ppm. Next the sample is irradiated by a high-energy electron beam over a long period of time ($\sim$6 months) to create a large number of vacancies. At the same time the sample is annealed to form nitrogen-vacancy (NV) centers. This process results in a concentration of $\sim$45 ppm of NV centers within the diamond corresponding to $\sim$5 nm of average separation and $\sim (2\pi)$ 420 kHz dipole-dipole interaction strength. To control the region of optical excitation, we use angle etching to create a beam shaped piece of diamond, of 20 μm length and 250 nm width and transfer it onto our coplanar waveguide [108].

D.1.2 Optical Setup

As shown in Fig. D.1, the optical setup consists of a home-built confocal microscope with a Nikon Plan Fluor 100x oil immersion objective (NA = 1.3). The sample is mounted on a xyz-piezoelectric stage in the focal plane of the microscope. Excitation of the ensemble of NV centers is performed by a continuous green laser ($\lambda = 532$ nm) with average power less than 50 μW. Short laser pulses are generated by an acousto-optic modulator (AOM) from Isomet in a double pass configuration. The lambda-half waveplate at the objective allows control over the polarization direction of excitation light. This can be used to selectively excite individual crystallographic NV orientations more efficiently than others. The NV center fluorescence is emitted into the phonon sideband (630-800 nm), which is separated from the excitation by a dichroic mirror. An additional 650 nm long pass filter further suppresses unwanted emission. After passing a pinhole the collection beam is then focused onto a single photon counting avalanche photodiode (APD) to achieve confocal detection.

D.1.3 Microwave Setup

To coherently control the electronic spin of the NV center we deliver microwaves to the sample through an impedance-matched coplanar waveguide fabricated on a glass coverslip. A small inner diameter (20 μm) of an omega-shaped microstructure at the center of the waveguide allows us to reach Rabi frequencies close to $\sim(2\pi)$ 100 MHz. In Fig. D.1, we illustrate the schematic setup of the microwave control system. Two independent microwave circuits are implemented to have full control over two groups of NV centers having different transition frequencies. The main driving frequencies are generated

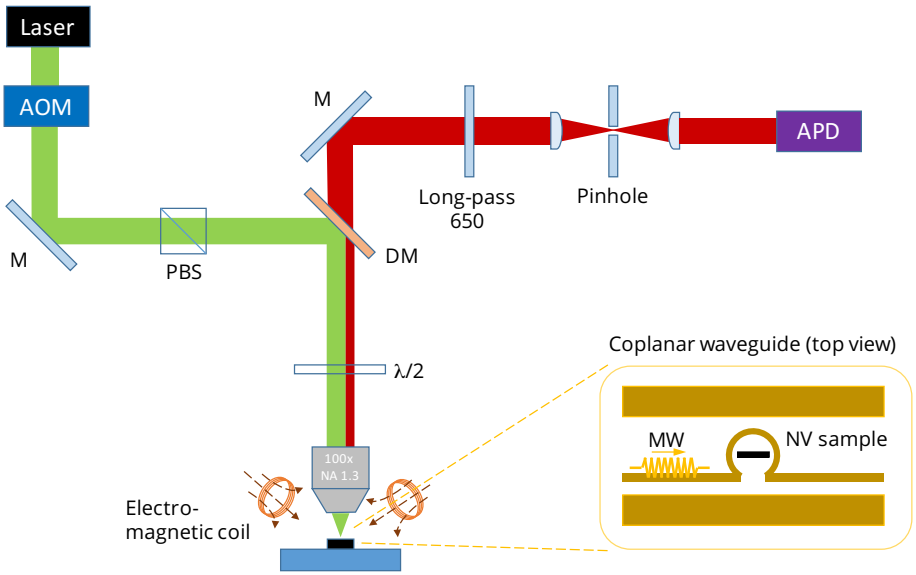

Figure D.1: **Schematic of the optical Setup.** Green and red lines indicate the optical paths (excitation: green, collection: red). An acousto-optic modulator (AOM) is used to control green laser duration. A dichroic mirror (DM) spectrally filters out the fluorescence from NV centers for electronic spin state readout. A 650 nm long pass filter additionally helps to filter fluorescence emission, corresponding to the phonon sideband (PSB) of NV centers. A 5-μm pinhole is used in combination with a single photon counting avalanche photodiode (APD) to achieve confocal detection. A polarizing beam splitter (PBS) is used to polarize the excitation beam. With the addition of a $\lambda/2$ waveplate we get control over the incident green polarization onto the diamond sample. The sample is placed ontop of a coplanar microwave (MW) structure in the shape of an omega (inset). Three electromagnetic coils are used to create a static magnetic field up to $\sim$300 Gauss in an arbitrary direction.

by two RF signal generators (Rohde & Schwarz SMIQ06B). A low-pass microwave filter (Mini-Circuits VLF-3000+) is added to suppress unwanted higher-order harmonics of fundamental frequencies. A DC block (Picosecond 5501a) is additionally used to isolate from low-frequency noise. Two microwave amplifiers (ZHL-16W-43+) used for both channels together with a power combiner (Mini-Circuits ZFRSC-42-S+). An arbitrary waveform generator (The Tektronix AWG7052) in conjunction with an IQ mixer is used to control the duration and phase of MW pulses on a timescale of 1 ns. The inset of Fig. D.2 depicts

the detailed configuration of analog inputs connected to the IQ mixers (Marki IQ1545LMP) used to define short microwave pulses. In order to finely tune the voltage offset of the I and Q port (to achieve high isolation), a DC voltage source is combined with the AWG signal. The addition of an attenuator allows the suppression of unwanted reflections.

D.1.4 Magnetic Field Setup

Three water-cooled electromagnetic (EM) coils provide an external magnetic field with an amplitude up to $\sim$300 Gauss in an arbitrary direction (see Fig. D.1 and D.3A). To calibrate the magnetic field created by the coils, electron spin resonance (ESR) spectra are recorded at several different values of coil currents. Since the Hamiltonian of the NV center in the presence of a B-field is known, the expected transition frequencies for all subensembles of NV centers (four different crystallographic orientations) can be calculated. The different groups A, B, C, and D of NV centers are characterized by their N-V axis orientations, i.e., A = [111], B = $[\bar{1}\bar{1}1]$, C = $[1\bar{1}\bar{1}]$, and D = $[\bar{1}1\bar{1}]$. By comparing ESR simulations to the experimental data, a unique transfer matrix can be calculated which converts coil current flow information into a magnetic field vector at the confocal spot. Figure D.3D shows an ESR spectrum with the B-field aligned along [111] direction. The group A exhibits the largest Zeeman splitting due to alignment of the spin quantization axis to the applied B-field. The other groups B, C, and D become degenerate due to the same projection angle of the B-field with respect to their crystallographic axes. In Fig. D.3D, the direction of an external B-field is perpendicular to the sample surface, i.e., B $\parallel$ [001], resulting in all the groups A-D having degenerate B-field projection.

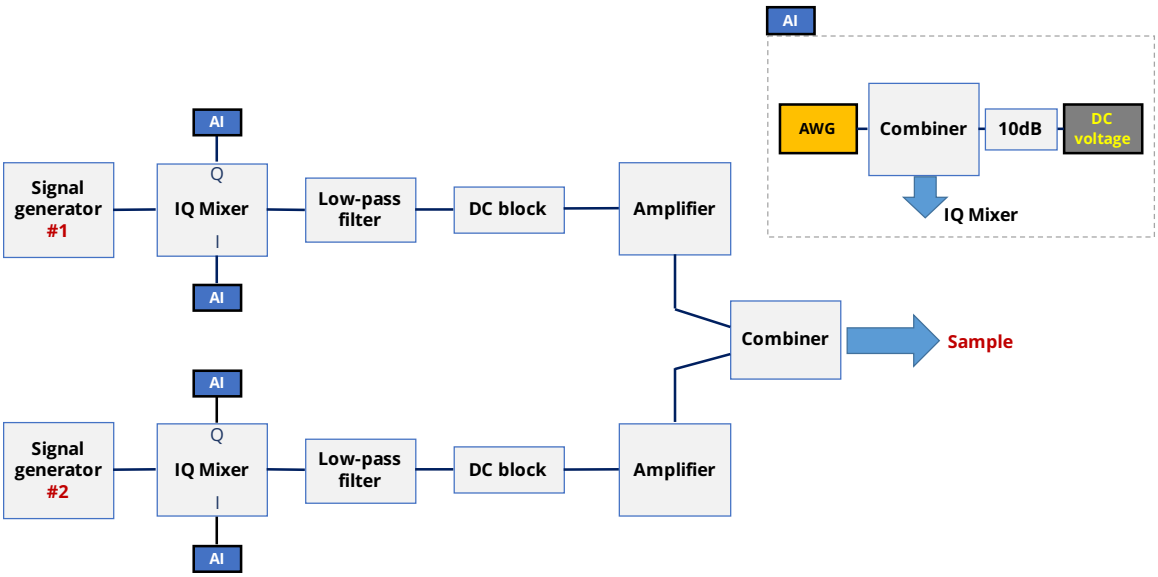

Figure D.2: **Schematic of the Microwave Control Setup.** Two sets of independent microwave circuits are used to achieve full control over two separate groups of NV centers at different transition frequencies. A 3 GHz low-pass filter suppresses unwanted higher-order harmonics. The two microwave paths are separately amplified to avoid saturation and then combined and sent to the diamond sample. In order to precisely control the microwave pulse length as well as phase, each path is sent through an IQ mixer controlled by an arbitrary waveform generator (AWG) output. The inset shows the detailed configuration of analog inputs connected to the IQ mixers used to define microwave pulse length and phase. In order to finely tune the voltage offset of the I and Q port, to achieve high isolation, a DC voltage source is combined with the AWG signal. The addition of an attenuator allows the suppression of unwanted reflections.

D.2 On-site Energy Disorder and Dipole-Dipole Interaction

D.2.1 Characterization of Disorder

The ESR linewidth of an ensemble of NV centers is influenced by multiple factors such as random magnetic fields originating from other lattice spin impurities such as ^{13}C or N, as well as local electric fields and lattice strain. While some of these contributions might

be spatially correlated (such as strain), others such as magnetic spin coupling are relatively short range and therefore act as a quasi random on-site potential disorder for the NV center. To quantify the different contributions to the linewidth, coherence measurements of different basis states can be performed. Since different states can be chosen to be sensitive/insensitive to different physical quantities, such measurements give insight into the diamond environment.

Figure D.4 shows both Ramsey spectroscopy as well as spin echo measurements for five different basis states / initialization configurations. Table D.1 shows how the quantum coherence of different initializations is affected by magnetic and electric noise from their local environment.

Definition	Wavefunction	Rate of dephasing	Noise	$1/T_2^*$
$\|\psi_1\rangle$	$(\|0\rangle + \|1\rangle)/\sqrt{2}$	$\gamma_{NV} B_\parallel$ + $d_\parallel E_\parallel$	$B_\parallel, E_\parallel$	$\pi[\Gamma_{B_\parallel} + \Gamma_{E_\parallel}]$
$\|\psi_2\rangle$	$(\|0\rangle + \|-1\rangle)/\sqrt{2}$	$\gamma_{NV} B_\parallel$ + $d_\parallel E_\parallel$	$B_\parallel, E_\parallel$	$\pi[\Gamma_{B_\parallel} + \Gamma_{E_\parallel}]$
$\|\psi_3\rangle$	$(\|1\rangle + \|-1\rangle)/\sqrt{2}$	$2\gamma_{NV} B_\parallel$	$B_\parallel$	$2\pi\Gamma_{B_\parallel}$
$\|\psi_4\rangle$	$(\|0\rangle + \|D\rangle)/\sqrt{2}$	$d_\parallel E_\parallel$ + $d_\perp E_\perp$	$E_\parallel$, $E_\perp$	$\pi[\Gamma_{E_\parallel} + \Gamma_{E_\perp}]$
$\|\psi_5\rangle$	$(\|0\rangle + \|B\rangle)/\sqrt{2}$	$d_\parallel E_\parallel$ + $d_\perp E_\perp$	$E_\parallel$, $E_\perp$	$\pi[\Gamma_{E_\parallel} + \Gamma_{E_\perp}]$

Table D.1: Five different basis states used for characterizing the local on-site disorder.

The dark ($|D\rangle$) and bright states ($|B\rangle$) are prepared by applying an off-axis magnetic field perpendicular to an NV symmetry axis, where $|D\rangle \equiv (|m_s = 1\rangle - |m_s = -1\rangle)/\sqrt{2}$ and $|B\rangle \equiv (|m_s = 1\rangle + |m_s = -1\rangle)/\sqrt{2}$. $B_\parallel$ ($E_\parallel$) and $B_\perp$ ($E_\perp$) are projected magnetic (electric) noise components, parallel and perpendicular to the NV axis. In addition, γ_{NV} = (2π) 2.8 MHz G^{-1}, $d_\parallel$ = (2π) 0.35 Hz cm V^{-1} and $d_\perp$ = (2π) 17 Hz cm V^{-1} are the gyromagnetic ratio of the NV, axial and perpendicular components of the ground triplet state permanent electric dipole moment of a NV center [125]. In consideration of the rate of

dephasing, we ignore $B_\perp$ to a first approximation because its effect is significantly smaller than $B_\parallel$ by a factor of $\sim \gamma_{NV} B_\perp / \Delta_0$, where Δ_0 = (2π) 2.87 GHz is the zero-field splitting of the NV center. Γ is a noise source-dependent inhomogeneous broadening contributing to the linewidth of the ESR.

As seen in the table D.1, each coherent superposition can effectively probe different types of noise components, enabling us to quantify their relative strengths to determine the on-site potential disorder. In a lifetime-broadened regime, we apply $\Gamma = 1/\pi T_2^*$ to extract a line broadening due to a particular noise source (see last column of Table D.1). Thus, using the measured T_2^* values from different configurations, we can estimate $\Gamma_{B_\parallel}$, $\Gamma_{E_\parallel}$, and $\Gamma_{E_\perp}$. The difference in T_2^* between $|\psi_1\rangle$ and $|\psi_2\rangle$ (as well as $|\psi_4\rangle$ and $|\psi_5\rangle$) in experimental data is presumably due to frequency-dependent field noise. When averaging these results, we can extract the three inhomogeneous broadening factors as $\Gamma_{B_\parallel}$ = 3.78(3) MHz, $\Gamma_{E_\parallel}$ = 2.18(8) MHz and $\Gamma_{E_\perp}$ = 4.30(13) MHz. The measured ESR linewidth $W_{FWHM} = \sqrt{8 \ln 2} W \approx$ 9.4 MHz (see Fig. 4.4) roughly agrees up to a factor of $\sim$1.5 with the calculated $\Gamma_{B_\parallel} + \Gamma_{E_\parallel} \approx$ 6.0 MHz. According to this analysis, the random on-site disorder in our sample seems to result from both electric and magnetic fields with comparable weights. For a spin echo sequence as shown in Fig. D.5C, time traces of $|\psi_{4,5}\rangle$ exhibit a modulation in decay envelope. This can be explained by hyperfine interaction with the ^{14}N nuclear spin [126].

D.2.2 Estimation of NV Density

The NV density-dependent dephasing rate as seen in Fig. 4.7 implies that the ensemble coherence in our sample is predominantly limited by dipolar interactions among NVs. Specifically, the total dephasing rate can be modeled as $\gamma_T = \gamma_b + \nu\gamma_0$, where γ_b and γ_0 are

bare and dipolar interaction-induced dephasing rates, respectively. To estimate the dependence of γ_T on the NV density, ν, we perform a few-spin exact diagonalization calculation. Comparing this result to the data allows us to extract the density of NV spins in our sample.

Fig. D.5 depicts the comparison of spin echo simulation results with the measured data by tuning the number of resonant NV groups (effective density). The simulation is conducted using 12 NV spins based upon an effective spin-1/2 model. The total NV concentrations selected for simulations are 5, 20, 40, 60, 70, 80 and 100 ppm. We averaged over $\sim$500 realizations of positional disorder, resulting in a single smooth coherence curve under the spin echo sequence. We fit the coherence decay with a simple exponential function. As seen in Fig. D.5A, a linear dependence of $1/T_2$ is identified for all the density values, thereby allowing us to extract γ_0 as a function of the NV density. We plot the interaction-related slope, γ_0, in Fig. D.5B. By comparison, the NV density in our sample is estimated to be $\sim$45 ppm. A similar analysis of the DEER data in Fig. 4.6 can be performed and reveals a comparable NV concentration.

D.3 Effective Hamiltonian of a driven System

In this section, we derive the effective Hamiltonian for a driven, dipolar interacting spin ensemble. The main idea is to work in a frame that is rotating along each NV group's quantization axis at corresponding driving frequency (ω_0^A and ω_0^B for group A and B, respectively). If the difference between ω_0^A and ω_0^B is large compared to the interaction strength, one can ignore exchange interactions between spins from different groups (secular approximation). This results in distinct forms of intra- and inter-group interactions. We project the Hamiltonian into effective two-level systems, and derive H_T, used in chapter 4.

We start with the Hamiltonian for dipolar interacting NV centers

$$H = \sum_i H_i^0 + \sum_i H_i^d(t) + \sum_{ij} H_{ij}^{dd} \tag{D.1}$$

where H_i^0 is a single particle Hamiltonian for a spin at site i, $H_i^d(t)$ is time-dependent driving, and H_{ij}^{dd} is the magnetic dipole-dipole interaction between spins at sites i and j. The first term H_i^0 includes Zeeman coupling to an external magnetic field, the zero-field splitting of a NV center, and any other disordered potentials described in chapter 4. In our experiments, dominant contributions for H_i^0 come from the zero-field splitting and Zeeman field projected along the quantization axis (a few hundred MHz), which are two orders of magnitude larger than the rest of the couplings. Setting $\hbar = 1$, we can write

$$H_i^0 \approx (\Delta_0 + \delta_i^0)\left(\hat{c}_i \cdot \vec{S}_i\right)^2 + (\Delta_B(\hat{c}_i) + \delta_i^B)\left(\hat{c}_i \cdot \vec{S}_i\right) \tag{D.2}$$

where $\vec{S}_i$ is the spin vector operator, $\hat{c}_i$ is the unit vector along the quantization axis of the spin, $\Delta_0 = (2\pi)\ 2.87$ GHz is the zero-field splitting, $\Delta_B(\hat{c}_i)$ is the Zeeman splitting along $\hat{c}_i$, and $\delta_{0,i}$ and $\delta_{B,i}$ are on-site disorder potentials. If the external magnetic field $\vec{B}$ is oriented in a way that $\Delta_B(\hat{c}_i)$ for different groups are sufficiently separated (compared to the driving strength), one can effectively address distinct groups independently. Below we assume such a case and consider resonant driving of two groups A and B using microwave frequencies $\omega_0^{A(B)} = \Delta_0 - \Delta_B(\hat{c}_{A(B)})$. The Hamiltonian for driving is given as $H_i^d(t) = \gamma_{NV}\vec{B}_{\text{MW}} \cdot \vec{S}_i \cos(\omega_0 t)$, where γ_{NV} is the gyromagnetic ratio of the NV center, and $\vec{B}_{\text{MW}}$ is the microwave field vector. Now moving into the rotating frame with unitary transformation $U(t) = \exp\left[-i\left(\sum_i \Delta_0(\hat{c}_i \cdot \vec{S}_i)^2 + \Delta_B(\hat{c}_i)(\hat{c}_i \cdot \vec{S}_i)\right)t\right]$ and applying

rotating wave approximations, we obtain the effective single particle Hamiltonian

$$\bar{H}_i = U^\dagger(t)\left[H_i^0 + H_i^d(t)\right]U(t) \tag{D.3}$$

$$= (\delta_{0,i} + \delta_{B,i})\,|1\rangle\langle 1| + (\delta_{0,i} - \delta_{B,i})\,|-1\rangle\langle -1| + \frac{\Omega_i}{2}\left(|-1\rangle\langle 0| + h.c.\right), \tag{D.4}$$

where $\{|1\rangle, |0\rangle, |-1\rangle\}$ is the basis of spin states along its quantization axis and Ω_i is the Rabi frequency of the driving.

The effective interaction among spins can be obtained in a similar way. We start with the dipole-dipole interaction between spin-i and spin-j

$$H_{ij}^{dd} = -\frac{J_0}{r^3}\left(3\left(\vec{S}_i\cdot\hat{r}\right)\left(\vec{S}_j\cdot\hat{r}\right) - \vec{S}_i\cdot\vec{S}_j\right), \tag{D.5}$$

where $J_0 = (2\pi)\ 52\ \text{MHz}\cdot\text{nm}^3$ and $\vec{r}$ is the relative position between two spins. In the rotating frame, we obtain the effective interaction by replace $\vec{S}_i \mapsto U^\dagger(t)\vec{S}_i U(t)$. Since we are interested in the interaction in the basis of each NV's own quantization axis, we first explicitly rewrite $\vec{S}_i$ in terms of (S_i^x, S_i^y, S_i^z) in a coordinate system where $\hat{z}_i$ is parallel to the quantization axis $\hat{c}_i$

$$\bar{H}_{ij}^{dd} = U^\dagger(t)H_{ij}^{dd}U(t) = -J_0/r^3\Big[\left(3\left(\hat{r}\cdot\hat{x}_i\right)\left(\hat{r}\cdot\hat{x}_j\right) - \hat{x}_i\cdot\hat{x}_j\right)S_i^xS_j^x \tag{D.6}$$

$$+\left(3\left(\hat{r}\cdot\hat{y}_i\right)\left(\hat{r}\cdot\hat{y}_j\right) - \hat{y}_i\cdot\hat{y}_j\right)S_i^yS_j^y \tag{D.7}$$

$$+\left(3\left(\hat{r}\cdot\hat{x}_i\right)\left(\hat{r}\cdot\hat{y}_j\right) - \hat{x}_i\cdot\hat{y}_j\right)S_j^xS_j^y \tag{D.8}$$

$$+\left(3\left(\hat{r}\cdot\hat{y}_i\right)\left(\hat{r}\cdot\hat{x}_j\right) - \hat{y}_i\cdot\hat{x}_j\right)S_i^yS_j^x \tag{D.9}$$

$$+\left(3\left(\hat{r}\cdot\hat{z}_i\right)\left(\hat{r}\cdot\hat{z}_j\right) - \hat{z}_i\cdot\hat{z}_j\right)S_i^zS_j^z\Big] \tag{D.10}$$

$$+H_{\text{rest}}, \tag{D.11}$$

where H_{rest} contains all the other terms of the form $S^xS^z, S^yS^z, S^zS^x, S^zS^y$.

We now perform a rotating wave approximation. This is very well justified because the typical strength of the interaction is much weaker than the driving frequency $J_0/r^3 \sim (2\pi)\ 0.4$ MHz $\ll \omega_0^{A,B} \sim (2\pi)\ 2.5$ GHz. First, we note that only S^x and S^y operators are rapidly oscillating in time while S^z remains invariant, $[S_i^z, U(t)] = 0$. Therefore, every term in H_{rest} may be safely ignored. Then, introducing

$$g_{ij}^{+} = \frac{1}{2}\Big[3\,(\hat{r}\cdot\hat{x}_i)\,(\hat{r}\cdot\hat{x}_j) - \hat{x}_i\cdot\hat{x}_j + 3\,(\hat{r}\cdot\hat{y}_i)\,(\hat{r}\cdot\hat{y}_j) - \hat{y}_i\cdot\hat{y}_j\Big] \tag{D.12}$$

$$g_{ij}^{-} = \frac{1}{2}\Big[3\,(\hat{r}\cdot\hat{x}_i)\,(\hat{r}\cdot\hat{x}_j) - \hat{x}_i\cdot\hat{x}_j - 3\,(\hat{r}\cdot\hat{y}_i)\,(\hat{r}\cdot\hat{y}_j) + \hat{y}_i\cdot\hat{y}_j\Big] \tag{D.13}$$

$$h_{ij}^{+} = \frac{1}{2}\Big[3\,(\hat{r}\cdot\hat{x}_i)\,(\hat{r}\cdot\hat{y}_j) - \hat{x}_i\cdot\hat{y}_j + 3\,(\hat{r}\cdot\hat{y}_i)\,(\hat{r}\cdot\hat{x}_j) - \hat{y}_i\cdot\hat{x}_j\Big] \tag{D.14}$$

$$h_{ij}^{-} = \frac{1}{2}\Big[3\,(\hat{r}\cdot\hat{x}_i)\,(\hat{r}\cdot\hat{y}_j) - \hat{x}_i\cdot\hat{y}_j - 3\,(\hat{r}\cdot\hat{y}_i)\,(\hat{r}\cdot\hat{x}_j) + \hat{y}_i\cdot\hat{x}_j\Big] \tag{D.15}$$

$$q_{ij} = 3\,(\hat{r}\cdot\hat{z}_i)\,(\hat{r}\cdot\hat{z}_j) - \hat{z}_i\cdot\hat{z}_j, \tag{D.16}$$

we can simply rewrite

$$\bar{H}_{ij}^{dd} \approx -J_0/r^3\big[g_{ij}^{+}(S_i^xS_j^x + S_i^yS_j^y) + h_{ij}^{-}(S_i^xS_j^y - S_i^yS_j^x) + q_{ij}S_i^zS_j^z \tag{D.17}$$

$$+ g_{ij}^{-}(S_i^xS_j^x - S_i^yS_j^y) + h_{ij}^{+}(S_i^xS_j^y + S_i^yS_j^x)\big]. \tag{D.18}$$

Here, g^+ and h^- terms correspond to "flip-flop" type transitions, exchanging one unit of spin polarization,

$$(S_i^xS_j^x + S_i^yS_j^y) = |{+}0\rangle\langle 0{+}| + |{+}{-}\rangle\langle 00| + |00\rangle\langle -{+}| + |0{-}\rangle\langle -0| + h.c. \tag{D.19}$$

$$(S_i^xS_j^y - S_i^yS_j^x) = i\big(\,|{+}0\rangle\langle 0{+}| + |{+}{-}\rangle\langle 00| + |00\rangle\langle -{+}| + |0{-}\rangle\langle -0|\,\big) + h.c. \tag{D.20}$$

In addition, owing to the strong anharmonic level structure, we may also ignore flip-flop transitions between levels with large energy differences, e.g. terms such as $|{+}{-}\rangle\langle 00|$. Finally, we ignore the terms in Eq. (D.18) as they correspond to double flip-up or flip-down

and rapidly oscillate in time. After these approximations, the effective interaction becomes

$$\bar{H}_{ij}^{dd} \approx -J_0/r^3 \left[\left(g_{ij}^{+} + i h_{ij}^{-} \right) |+0\rangle \langle 0+| + |0-\rangle \langle -0| + h.c. + q_{ij} S_i^z S_j^z \right]. \tag{D.21}$$

Now we divide the discussion into two cases depending on whether spins i and j belong to the same group or to different groups. In the former case, the quantization axes coincide, and we can simplify $h_{ij}^{-} = 0$, $g_{ij}^{+} = \frac{1}{2}(1 - 3\cos^2\theta)$, and $q_{ij} = -(1 - 3\cos^2\theta)$ with $\cos\theta \equiv \hat{z} \cdot \hat{r}$. In the latter case, the flip-flop terms are again rapidly oscillating, and only the Ising interaction $S_i^z S_j^z$ remains, resulting in

$$\bar{H}_{ij}^{dd} \approx \begin{cases} -\frac{J_0 q_{ij}}{r^3} \left(-\frac{|+0\rangle\langle 0+| + |0-\rangle\langle -0| + h.c.}{2} + S_i^z S_j^z \right) & \text{same group} \\ -\frac{J_0 q_{ij}}{r^3} S_i^z S_j^z & \text{different groups} \end{cases}. \tag{D.22}$$

These interactions as well as the single particle terms conserve the total population of spins in $|+\rangle$. Therefore, once the system is initialized into a state with no population in $|+\rangle$, the dynamics remains in the manifold spanned by $|-\rangle$ and $|0\rangle$. Projecting $\sum_i \bar{H}_i + \sum_{ij} \bar{H}_{ij}^{dd}$ into this manifold, we obtain the Hamiltonian for an effective two-level system. Finally, introducing spin-1/2 operators $\vec{\sigma}$ for two levels $|-\rangle$ and $|0\rangle$, we obtain $H_T = H_A + H_B + H_{AB}$ where

$$H_{A(B)} = \sum_{i \in A(B)} \left[(\delta_{0,i} - \delta_{B,i}) \sigma_i^z + \Omega_{A(B)} \sigma_i^x \right] + \sum_{i,j \in A(B)} \frac{J_0 q_{ij}}{r_{ij}^3} \left(\sigma_i^x \sigma_j^x + \sigma_i^y \sigma_j^y - \sigma_i^z \sigma_j^z \right), \tag{D.23}$$

$$H_{AB} = -\sum_{i \in A, j \in B} \frac{J_0 q_{ij}}{r_{ij}^3} \sigma_i^{z_A} \sigma_j^{z_B}, \tag{D.24}$$

up to a constant. This Hamiltonian is of the form presented in chapter 4 with appropriate identifications of $\delta_i \equiv \delta_{0,i} - \delta_{B,i}$ and $J_{ij} \equiv J_0 q_{ij}$.

We remark one particularly interesting aspect of this Hamiltonian in the dressed-state basis. With sufficiently strong driving, σ_i^x becomes a good spin polarization basis, and one

can rewrite the interactions in terms of $\sigma^{\pm} = \sigma^y \pm i\sigma^z$, wherein the intra-group interaction becomes $\sigma_i^x\sigma_j^x + (\sigma_i^+\sigma_j^+ + \sigma_i^-\sigma_j^-)/2$. Here, we find that spin exchange terms $(\sigma_i^+\sigma_j^- + h.c.)$ are missing (and also note that $\sigma_i^+\sigma_j^+ + \sigma_i^-\sigma_k^-$ terms are energetically suppressed). This implies that spin polarization transport within a group is strongly suppressed by the driving.

D.4 Resonance Counting Theory

In this section, we provide a detailed study of the single particle resonance counting theory. We will first focus on the case of quenched on-site potential disorder, deriving the disorder-dependent power-law relaxation presented in chapter 4. Then, we generalize the result to the case when disordered potentials are time-dependent in two different ways: uncorrelated and correlated. For the first case, we consider a model where on-site disorder configurations undergo uncorrelated changes at rate Γ. The result from this model captures most of the features observed in our experiments as presented in chapter 4. For the second case we analyze the situation in which only a fraction of on-site disorder is changing, leading to a correlation in time.

D.4.1 Disorder-dependent power-law decay

As discussed in chapter 4, we estimate the survival probability of a single spin excitation based on a simple counting argument. We consider a dynamical formation of k-resonating clusters; at time t, we compute the probability $\Pr(k;t)$ that the central spin is connected to $k-1$ other spins via a network of resonances defined in chapter 4. Assuming that the population of the excitation is equally shared among a resonating cluster, the survival

probability is given as

$$P(t) \approx \sum_{k=1}^{\infty} \frac{1}{k} \mathrm{Pr}(k;t). \tag{D.25}$$

reducing our problem to the computation of $\mathrm{Pr}(k;t)$. Below we will show that the dominant contributions arise from $k = 1$.

In general, the exact calculation of $\mathrm{Pr}(k;t)$ is difficult. This is because the connectivity of the resonance network is correlated due to the spatial structure (d-dimensional Euclidean space) as well as a given assignment of random on-site potentials: if spin pairs (a, b) and (b, c) are pair-wise resonant, it is likely that the pair (a, c) is also resonant, etc. However, the qualitative behavior of $\mathrm{Pr}(k;t)$ can still be well-understood by ignoring these correlations. In such cases, the resonance network can be viewed as a random graph generated by a so-called Galton-Watson process: starting from the central spin, a spin "reproduces" ℓ "children spins" (the central spin finds ℓ resonant spins). The number of children ℓ is drawn from a probability distribution $p(\ell)$. Each child spin then reproduces its own children, whose number is again independent and identically distributed according to the same $p(\ell)$. This process terminates when no more children spins are produced. In this picture, $\mathrm{Pr}(k;t)$ corresponds to the probability that the central spin generates total $k-1$ descendant and the process terminates. We note that such a process may not terminate, in which case the central excitation becomes delocalized over a macroscopic number of spins.

In order to estimate $\mathrm{Pr}(k;t)$, we first compute $p(\ell)$ as a function of time t. Such $p(\ell;t)$ is the probability of having ℓ *directly* resonating spins at time t. For $\ell = 0$, a spin of interest (spin-i) must not have any resonating spins at any distance from r_{min} to $R(t) \equiv (J_0 t)^{1/3}$, where r_{min} is the short-distance cut-off of spin-spin distances. Hence, $p(0;t)$ is given as a

product of probabilities:

$$p(0;t) = \prod_{r_{\text{min}} \le r < R(t)} \left(1 - 4\pi n r^2 dr \frac{\beta J_0/r^3}{W_{\text{eff}}}\right) \tag{D.26}$$

$$= \exp\left[-\int_{r_{\text{min}}}^{R(t)} \frac{\beta 4\pi n J_0}{W_{\text{eff}}} r^{-1} dr\right] \tag{D.27}$$

where $4\pi n r^2 dr$ is the probability of finding a spin at distance r, and $\beta J_0/(W_{\text{eff}} r^3)$ is the probability that the spin (if it exists) resonates with the spin-i. Defining $\lambda(t) = \frac{\beta 4\pi n J_0}{W_{\text{eff}}} \ln \frac{R(t)}{r_{\text{min}}}$, we obtain $p(0;t) = \exp\left[-\lambda(t)\right]$. Similarly, we can calculate $p(\ell;t)$ for $\ell > 0$, and obtain $p(\ell;t) = \frac{1}{\ell!}\left(\lambda(t)\right)^{\ell} e^{-\lambda(t)}$, which is the Poisson distribution with mean $\lambda(t)$.

One interesting aspect of a Galton-Watson process with a Poisson distribution is that the probability that the process would ever terminate P_{term} may be dominated by the termination at the first step. More specifically, we have the self-consistency equation

$$P_{\text{term}} = e^{-\lambda} + \sum_{\ell=1}^{\infty} \frac{\lambda^{\ell} e^{-\lambda}}{\ell!} \left(P_{\text{term}}\right)^{\ell}, \tag{D.28}$$

where the first term corresponds to the case where the initial spin does not have any resonance up to time t, while the second term implies the termination of each sub-graph generated from ℓ children spins. For sufficiently large λ, P_{term} becomes small, and its contribution is dominated by the first term. In our case, $\lambda(t)$ is a function of time which diverges in the limit $t \to \infty$. As we are interested in the late time dynamics, we may only consider the first term. In terms of $\Pr(k;t)$, this corresponds to approximating $\Pr(k;t) \sim 0$ for $k > 2$. Finally, noting that that $\Pr(k=1;t) = p(0;t)$, we recover the expression in chapter 4.

D.4.2 Time-dependent disorder I: uncorrelated spectral jumps

Now we consider the case of time-dependent disorder. We assume that the on-site disorder configuration $\tilde{\delta}_i$ changes (spectral jumps) at an average rate Γ. Then, the survival

probability is modified and can be written as

$$\overline{P(t)} = \sum_{k=0}^{\infty} \sum_{0<t_1<\cdots<t_k<t} Prob(t_1, t_2, \cdots t_k) P_k(t; t_1, t_2, \cdots t_k) \tag{D.29}$$

where $Prob(t_1, t_2, \cdots, t_k)$ is the probability of having k spectral jumps at times $0 < t_1 < t_2 < \cdots < t_k < t$, and $P_k(t; t_1, t_2, \cdots t_k)$ is the survival probability of the spin excitation, given that disorder configuration changes at times $\{t_i\}$. Assuming a Poisson process, we have

$$Prob(t_1, t_2, \cdots, t_k) = e^{-\Gamma t_1}(\Gamma dt_1) e^{-\Gamma(t_2-t_1)}(\Gamma dt_2) \cdots (\Gamma dt_k) e^{-\Gamma(t-t_k)} \tag{D.30}$$

$$= e^{-\Gamma t} \prod_i \Gamma dt_i. \tag{D.31}$$

If disorder configurations for different time intervals $t_{i+1} - t_i$ are uncorrelated, the survival probability $P_k(t; t_1, t_2, \cdots t_k)$ is simply the product of survival probabilities for each time interval,

$$P_k(t; t_1, t_2, \cdots t_k) = \prod_{i=0}^{k} \left((t_{i+1} - t_i)/t_c\right)^{-\eta}, \tag{D.32}$$

where $\eta = 4\pi n J_0 \beta/(3W_{\text{eff}})$ is the disorder-dependent exponent, $t_0 = 0$, $t_{k+1} = t$, and t_c is short-time cut-off set by interaction strength between a nearest possible spin pair. Combining these two factors and integrating over all possible times for quantum jumps, we obtain

$$\overline{P(t)} = \sum_{k=0}^{\infty} e^{-\Gamma t} (\Gamma t)^k (t/t_c)^{-(k+1)\eta} \int_{0<z_1<\cdots<z_k<1} \prod_{i=0}^{k} (z_{i+1} - z_i)^{-\eta} \prod_{i=1}^{k} dz_i, \tag{D.33}$$

where we introduced $z_i \equiv t_i/t$. Finally, defining $c_k \equiv k! \int_{0<z_1<\cdots<z_k<1} \prod_{i=0}^{k} (z_{i+1} - z_i)^{-\eta} \prod_{i=1}^{k} dz_i$, we obtain the expression presented in chapter 4.

As illustrated in Fig. D.6, the uncorrelated spectral jump model demonstrates an excellent agreement with the experimental data over all time scales. A Monte-Carlo optimization is used to extract the spectral jump rate Γ = 21 $\pm$ 3 kHz with the power-law exponent

η set equal to that obtained from a single particle exact diagonalization simulation (see Fig. 4.16).

D.4.3 Time-dependent disorder II: uncorrelated spectral jumps

The analysis in the previous section assumes that the on-site potentials $\tilde{\delta}_i(t)$ are uncorrelated before and after a spectral jump. That is, if a spectral jump occurs at time t^*,

$$\sigma^2_{\text{corr}} \equiv [\![\tilde{\delta}_i(t^*-\epsilon)\tilde{\delta}_i(t^*+\epsilon)]\!] - [\![\tilde{\delta}_i(t^*-\epsilon)]\!][\![\tilde{\delta}_i(t^*+\epsilon)]\!] = 0, \tag{D.34}$$

where ϵ is a small positive number, and $[\![\ldots]\!]$ indicates averaging over disorder realizations. In general, this need not be the case ($\sigma^2_{\text{corr}} \neq 0$) since the microscopic origin of $\tilde{\delta}_i$ involves both time-dependent (nitrogen spin impurities or NV centers, etc) and time-independent (local strain fields from lattice defects, long-lived nuclear spins, etc) contributions. Here, we provide the analysis of resonance counting when $\sigma^2_{\text{corr}} \neq 0$.

For concreteness, we assume that the on-site potential disorder is given as a sum of a static and a dynamical disorder potential, $\tilde{\delta}_i(t) = \tilde{\delta}^s_i + \tilde{\delta}^d_i(t)$, where the static part $\tilde{\delta}^s_i$ (dynamical part $\tilde{\delta}^d_i(t)$) is random with zero mean and standard deviation W_s (W_d). While $\tilde{\delta}^s_i$ is time-independent, the dynamical component $\tilde{\delta}^d_i(t)$ changes over time by uncorrelated jumps at a rate Γ'. The long time correlation σ^2_{corr} is controlled by W_s, and the correlation time is set by $1/\Gamma'$. Here, we focus on an experimentally relevant regime, where $W_s > W_d \gtrsim nJ \gg \Gamma'$.

When disorder configurations are correlated, the survival probability cannot be factorized as in Eq. (D.32). Hence, the approach used in the previous section is not very useful. Instead, we include the time-dependent nature of $\tilde{\delta}_i(t)$ by modifying resonance criteria as follows. Two spins at sites i and j are on resonance at time t if: (1) *at any point*

in time $t' < t$, their energy mismatch is smaller than their dipolar interaction strength, $|\tilde{\delta}_i(t') - \tilde{\delta}_j(t')| < \beta J_{ij}/r_{ij}^3$, and (2) the interaction occurs within the time-scale t, $J_{ij}/r_{ij}^3 > 1/t$. While the second part of the condition is unchanged, the first part now captures that a pair may be brought into resonance by spectral jumps. Under the hierarchy of $W_s > W_d \gtrsim nJ \gg \Gamma'$, the condition (1) can be approximated by two independent events: (a) the static energy mismatch is close enough, $|\tilde{\delta}_i^s - \tilde{\delta}_j^s| < W_d$, and (b) the dynamical energy mismatch is smaller than the coupling strength, $|\tilde{\delta}_i^d(t') - \tilde{\delta}_j^d(t')| < \beta J_{ij}/r_{ij}^3$, at some time $t' < t$. In combination, the condition (1) is satisfied with the probability

$$P_{\text{res}}(r,t) \approx \frac{W_d}{W_s}\left(1 - e^{-\frac{\beta J_0/r^3}{W_d}\Gamma' t}\left(1 - \frac{\beta J_0/r^3}{W_d}\right)\right)$$

which is the product of probabilities for conditions (a) and (b). For the condition (b), we used the probabilities that the initial configuration is off-resonant $1 - \frac{\beta J_0/r^3}{W_d}$ and that none of subsequent spectral jumps brings them into resonance $e^{-\frac{\beta J_0/r^3}{W_d}\Gamma' t}$. Finally, the survival probability is obtained by requiring no resonance at every distance r up to $R(t) = (J_0 t)^{1/3}$

$$\overline{P(t)} = \exp\left[-\int_{r=r_0}^{R(t)} 4\pi n r^2 P_{\text{res}}(r,t) dr\right] \tag{D.35}$$

We note that in the limit of $\Gamma' \to 0$ the Eq. (D.35) correctly reduces to the disorder-dependent power-law decay.

In Fig. D.6, the correlated spectral jump model of Eq. (D.35) is plotted at different Rabi frequencies to be compared with the experimental data as well as the previously described uncorrelated model. Based on a Monte-Carlo simulation, we extract the parameters W_d/W_s, β, and Γ'. Here the spectral jump rate Γ' is estimated to be 16 $\pm$ 1 kHz which is smaller than Γ = 21 $\pm$ 3 kHz. As seen in Fig. D.6, both theoretical models of the uncorrelated and the correlated time-dependent disorders exhibit a reasonable agreement with the experimental observation.

To estimate the timescale of the microscopic processes leading to a time dependence of disorder, we note previous work, that investigated the spin-diffusion of implanted nitrogen (P1) centers in diamond [107]. At 6 ppm of P1 center concentration, they measured an average flip-flop time of nitrogen electronics spins, $\overline{T}_{ff} = 210\ \mu s$ [107]. For a low fractional concentration of such paramagnetic spins, the flip-flop time scale is inversely proportional to the density of dipolar spins [127, 128]. Thus, we expect $\overline{T}_{ff} \sim 70\ \mu s$ at a P1 density of 20 ppm in our sample. We also note that the measured depolarization time, T_1, of NV centers in our sample is $\sim 50\ \mu s$. The extracted $1/\Gamma,\ 1/\Gamma' \sim (50 - 60)\mu s$ are indeed consistent with the spin-diffusion time of P1 centers $\overline{T}_{ff} \sim 70\ \mu s$ and the measured NV depolarization time $T_1 \sim 50\ \mu s$.

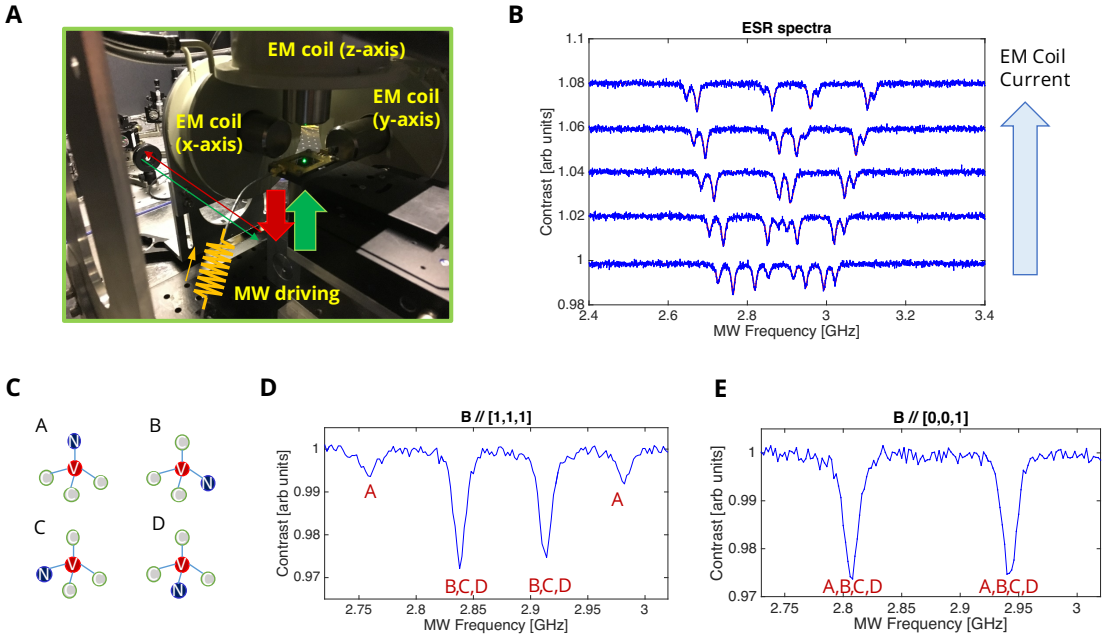

Figure D.3: **Magnetic Field Calibration and Control. (A)** Three electromagnetic (EM) coils are located in the vicinity of the diamond sample in order to provide an external magnetic field (B-field) in an arbitrary direction with an amplitude up to ∼300 Gauss. **(B)** To calibrate the coil's magnetic field, electron spin resonance (ESR) spectra are recorded for different values of coil currents. **(C)** The diamond lattice allows for four different crystallographic orientations of NV centers. The different groups A, B, C, and D of NV centers are characterized by their N-V axis orientations, i.e., A = [111], B = $[\bar{1}\bar{1}1]$, C = $[1\bar{1}\bar{1}]$, and D = $[\bar{1}1\bar{1}]$. **(D)** Measured ESR spectrum for the B-field aligned along the [111] direction. Group A exhibits the largest Zeeman splitting (highest projected $B_{||}$) because the spin quantization axis of group A is parallel to the chosen B-field. **(E)** Measured ESR spectrum for the B-field aligned along the [001] direction. Due to the [100] cutting direction of the diamond, all 4 NV groups form the same angle to the surface. With the external B-field being perpendicular to the sample surface, this leads to groups A-D having degenerate B field projections.

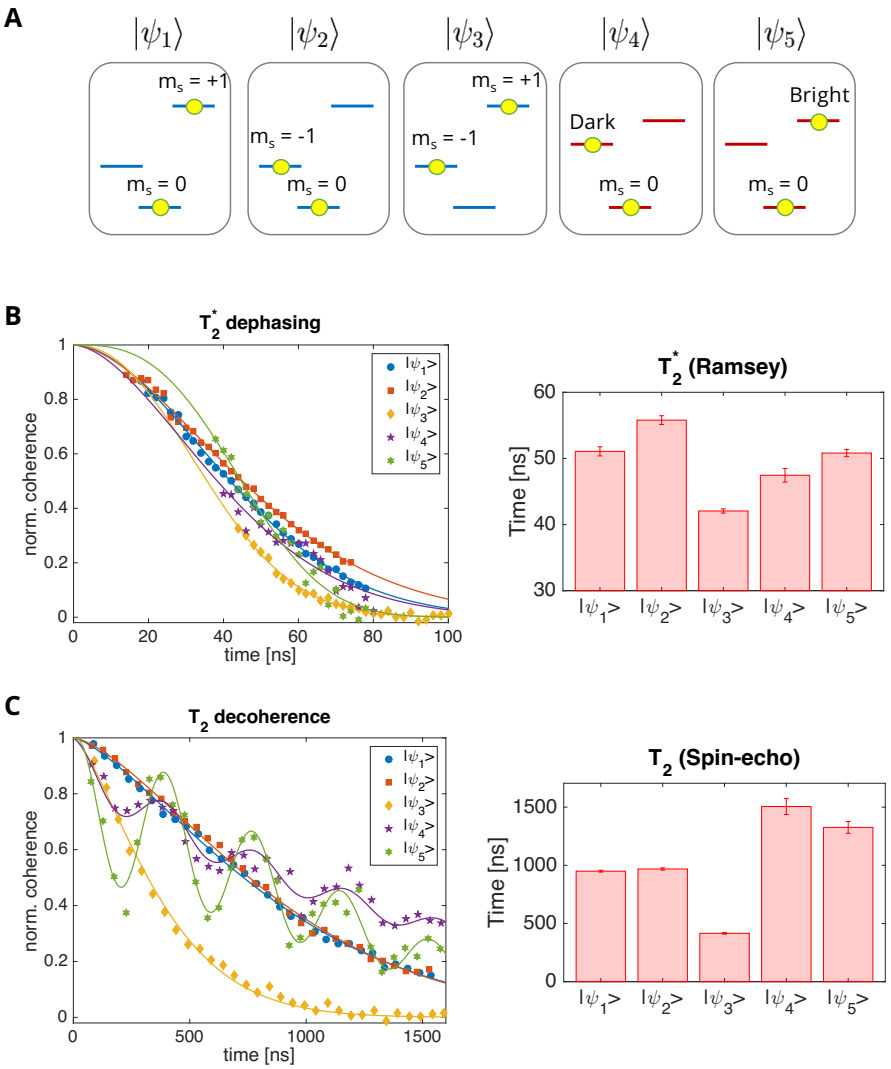

Figure D.4: T_2^* **and** T_2 **Measurements of different Basis States.** **(A)** Different initial conditions used for coherence measurements. By aligning the magnetic field parallel (perpendicular) to the NV axis, the eigenbasis for the spin state of NV centers becomes $\{|m_s = 0\rangle, |m_s = +1\rangle, |m_s = -1\rangle\}$ ($\{|m_s = 0\rangle, |Dark\rangle, |Bright\rangle\}$), where Bright and Dark states are defined as even and odd combination of the original bare spin states $|m_s = -1\rangle$ and $|m_s = +1\rangle$. **(B)** Ramsey spectroscopy data and extracted decay timescale for different initial states. **(C)** Coherence time measurements extracted via a spin-echo sequence.

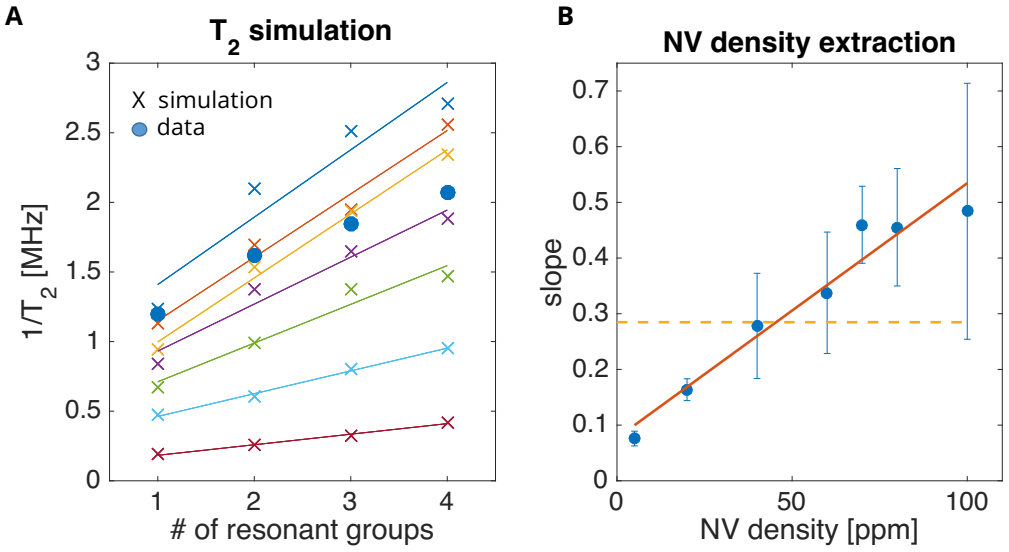

Figure D.5: **NV Density Extraction via Spin Echo Simulation.** **(A)** Comparison of the spin echo simulation results at different concentrations (crosses) to the measured data (circles). The total NV concentrations selected for the simulation are 5, 20, 40, 60, 70, 80 and 100 ppm. Solid lines are linear fits to the simulation to extract both γ_b and γ_0. **(B)** The NV concentration can be extracted by comparing the slopes (γ_0) taken from the numerical simulations to the extracted slope of the experiment data (orange dashed line).

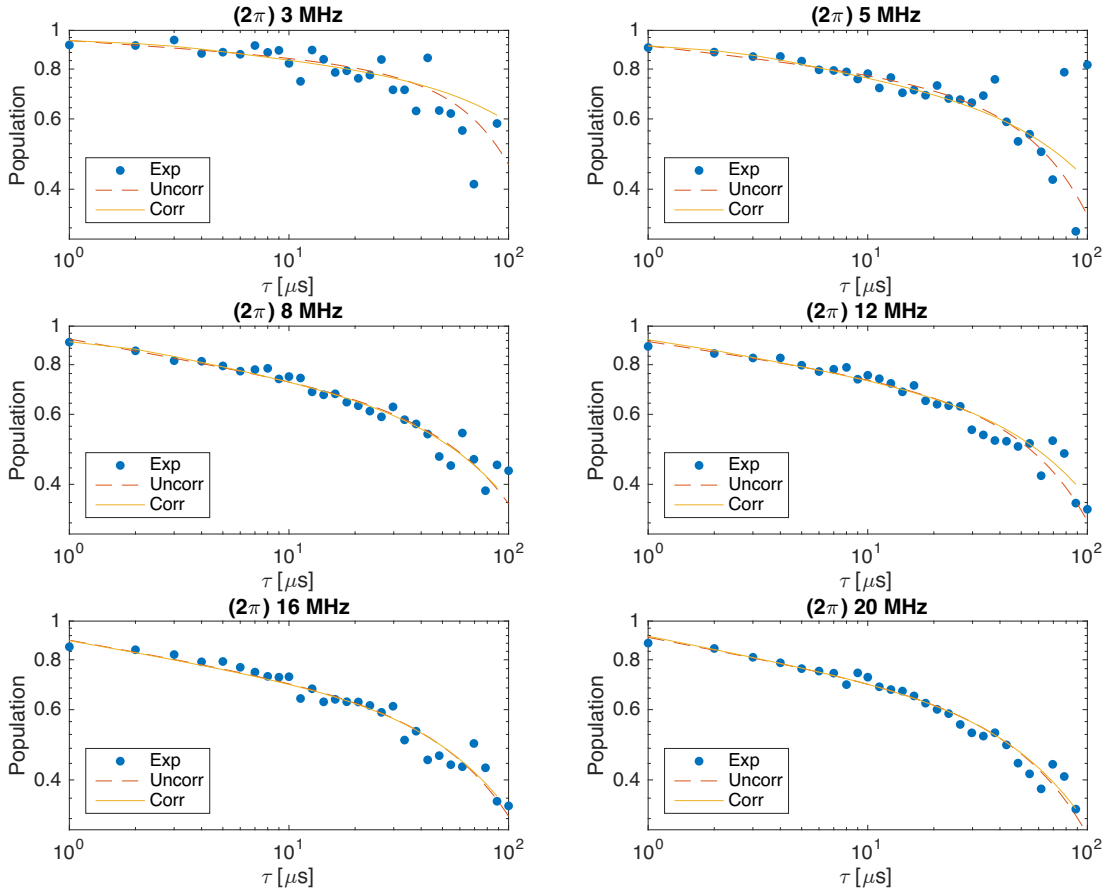

Figure D.6: **NV polarization decay under Hartmann-Hahn conditions** Dashed (red) and solid (orange) lines are Monte-Carlo fits based upon uncorrelated and correlated spectral jump model, respectively.

Bibliography

[1] H. Casimir. The historical development of quantum theory. *Contemporary Physics*, 24(6):631–634, 1983.

[2] D. Kielpinski, C. Monroe, and D. J. Wineland. Architecture for a large-scale ion-trap quantum computer. *Nature*, 417(6890):709–711, 2002.

[3] M. Greiner, O. Mandel, T. Esslinger, T. W. Hänsch, and I. Bloch. Quantum phase transition from a superfluid to a mott insulator in a gas of ultracold atoms. *nature*, 415(6867):39–44, 2002.

[4] T. D. Ladd, F. Jelezko, R. Laflamme, Y. Nakamura, C. Monroe, and J. L. OBrien. Quantum computers. *Nature*, 464(7285):45–53, 2010.

[5] C. Langer, R. Ozeri, J. D. Jost, J. Chiaverini, B. DeMarco, A. Ben-Kish, R. Blakestad, J. Britton, D. Hume, W. Itano, et al. Long-lived qubit memory using atomic ions. *Physical review letters*, 95(6):060502, 2005.

[6] A. Wallraff, D. I. Schuster, A. Blais, L. Frunzio, R.-S. Huang, J. Majer, S. Kumar, S. M. Girvin, and R. J. Schoelkopf. Strong coupling of a single photon to a superconducting qubit using circuit quantum electrodynamics. *Nature*, 431(7005):162–167, 2004.

[7] G. Balasubramanian, P. Neumann, D. Twitchen, M. Markham, R. Kolesov, N. Mizuochi, J. Isoya, J. Achard, J. Beck, J. Tissler, et al. Ultralong spin coherence time in isotopically engineered diamond. *Nature materials*, 8(5):383–387, 2009.

[8] A. M. Tyryshkin, S. Tojo, J. J. Morton, H. Riemann, N. V. Abrosimov, P. Becker, H.-J. Pohl, T. Schenkel, M. L. Thewalt, K. M. Itoh, et al. Electron spin coherence exceeding seconds in high-purity silicon. *Nature materials*, 11(2):143–147, 2012.

[9] M. Steger, K. Saeedi, M. Thewalt, J. Morton, H. Riemann, N. Abrosimov, P. Becker, and H.-J. Pohl. Quantum information storage for over 180 s using donor spins in a 28si semiconductor vacuum. *Science*, 336(6086):1280–1283, 2012.

[10] V. Giovannetti, S. Lloyd, and L. Maccone. Quantum metrology. *Physical review letters*, 96(1):010401, 2006.

[11] V. Giovannetti, S. Lloyd, and L. Maccone. Advances in quantum metrology. *Nature Photonics*, 5(4):222–229, 2011.

[12] P. Maletinsky, S. Hong, M. S. Grinolds, B. Hausmann, M. D. Lukin, R. L. Walsworth, M. Loncar, and A. Yacoby. A robust scanning diamond sensor for nanoscale imaging with single nitrogen-vacancy centres. *Nature nanotechnology*, 7(5):320–324, 2012.

[13] D. Le Sage, K. Arai, D. Glenn, S. DeVience, L. Pham, L. Rahn-Lee, M. Lukin, A. Yacoby, A. Komeili, and R. Walsworth. Optical magnetic imaging of living cells. *Nature*, 496(7446):486–489, 2013.

[14] G. Kucsko, P. Maurer, N. Y. Yao, M. Kubo, H. Noh, P. Lo, H. Park, and M. D. Lukin. Nanometre-scale thermometry in a living cell. *Nature*, 500(7460):54–58, 2013.

[15] G. A. Álvarez, D. Suter, and R. Kaiser. Localization-delocalization transition in the dynamics of dipolar-coupled nuclear spins. *Science*, 349(6250):846–848, 2015.

[16] G. Waldherr, J. Beck, M. Steiner, P. Neumann, A. Gali, T. Frauenheim, F. Jelezko, and J. Wrachtrup. Dark states of single nitrogen-vacancy centers in diamond unraveled by single shot nmr. *Physical Review Letters*, 106(15):157601, 2011.

[17] A. Gruber, A. Dräbenstedt, C. Tietz, L. Fleury, J. Wrachtrup, and C. Von Borczyskowski. Scanning confocal optical microscopy and magnetic resonance on single defect centers. *Science*, 276(5321):2012–2014, 1997.

[18] F. Jelezko and J. Wrachtrup. Single defect centres in diamond: A review. *physica status solidi (a)*, 203(13):3207–3225, 2006.

[19] S. Kolkowitz, A. Safira, A. High, R. Devlin, S. Choi, Q. Unterreithmeier, D. Patterson, A. Zibrov, V. Manucharyan, H. Park, et al. Probing johnson noise and ballistic transport in normal metals with a single-spin qubit. *Science*, 347(6226):1129–1132, 2015.

[20] J. Loubser and J. van Wyk. Electron spin resonance in the study of diamond. *Reports on Progress in Physics*, 41(8):1201, 1978.

[21] P. Neumann, J. Beck, M. Steiner, F. Rempp, H. Fedder, P. R. Hemmer, J. Wrachtrup, and F. Jelezko. Single-shot readout of a single nuclear spin. *Science*, 329(5991):542–544, 2010.

[22] M. G. Dutt, L. Childress, L. Jiang, E. Togan, J. Maze, F. Jelezko, A. Zibrov, P. Hemmer, and M. Lukin. Quantum register based on individual electronic and nuclear spin qubits in diamond. *Science*, 316(5829):1312–1316, 2007.

[23] T. H. Taminiau, J. Cramer, T. van der Sar, V. V. Dobrovitski, and R. Hanson. Universal control and error correction in multi-qubit spin registers in diamond. *Nature nanotechnology*, 9(3):171–176, 2014.

[24] E. Togan, Y. Chu, A. Trifonov, L. Jiang, J. Maze, L. Childress, M. G. Dutt, A. S. Sørensen, P. Hemmer, A. Zibrov, et al. Quantum entanglement between an optical photon and a solid-state spin qubit. *Nature*, 466(7307):730–734, 2010.

[25] H. Bernien, B. Hensen, W. Pfaff, G. Koolstra, M. Blok, L. Robledo, T. Taminiau, M. Markham, D. Twitchen, L. Childress, et al. Heralded entanglement between solid-state qubits separated by three metres. *Nature*, 497(7447):86–90, 2013.

[26] B. Hensen, H. Bernien, A. Dréau, A. Reiserer, N. Kalb, M. Blok, J. Ruitenberg, R. Vermeulen, R. Schouten, C. Abellán, et al. Loophole-free bell inequality violation using electron spins separated by 1.3 kilometres. *Nature*, 526(7575):682–686, 2015.

[27] J. Maze, P. Stanwix, J. Hodges, S. Hong, J. Taylor, P. Cappellaro, L. Jiang, M. G. Dutt, E. Togan, A. Zibrov, et al. Nanoscale magnetic sensing with an individual electronic spin in diamond. *Nature*, 455(7213):644–647, 2008.

[28] A. Sushkov, I. Lovchinsky, N. Chisholm, R. L. Walsworth, H. Park, and M. D. Lukin. Magnetic resonance detection of individual proton spins using quantum reporters. *Physical review letters*, 113(19):197601, 2014.

[29] I. Lovchinsky, A. Sushkov, E. Urbach, N. de Leon, S. Choi, K. De Greve, R. Evans, R. Gertner, E. Bersin, C. Müller, et al. Nuclear magnetic resonance detection and spectroscopy of single proteins using quantum logic. *Science*, 351(6275):836–841, 2016.

[30] F. Dolde, H. Fedder, M. Doherty, T. Nöbauer, F. Rempp, G. Balasubramanian, T. Wolf, F. Reinhard, L. Hollenberg, F. Jelezko, et al. Electric-field sensing using single diamond spins. *Nature Physics*, 7(6):459–463, 2011.

[31] L.-M. Duan and C. Monroe. Quantum networks with trapped ions. *Rev. Mod. Phys.*, 82:1209–1224, Apr 2010.

[32] C. Langer, R. Ozeri, J. D. Jost, J. Chiaverini, B. DeMarco, A. Ben-Kish, R. B. Blakestad, J. Britton, D. B. Hume, W. M. Itano, D. Leibfried, R. Reichle, T. Rosenband, T. Schaetz, P. O. Schmidt, and D. J. Wineland. Long-lived qubit memory using atomic ions. *Phys. Rev. Lett.*, 95:060502, Aug 2005.

[33] T. D. Ladd, D. Maryenko, Y. Yamamoto, E. Abe, and K. M. Itoh. Coherence time of decoupled nuclear spins in silicon. *Phys. Rev. B*, 71:014401, Jan 2005.

[34] M. V. Balabas, T. Karaulanov, M. P. Ledbetter, and D. Budker. Polarized alkali-metal vapor with minute-long transverse spin-relaxation time. *Phys. Rev. Lett.*, 105:070801, Aug 2010.

[35] A. Morello, J. J. Pla, F. A. Zwanenburg, K. W. Chan, K. Y. Tan, H. Huebl, M. Möttönen, C. D. Nugroho, C. Yang, J. A. van Donkelaar, et al. Single-shot readout of an electron spin in silicon. *Nature*, 467(7316):687–691, 2010.

[36] T. Van der Sar, Z. Wang, M. Blok, H. Bernien, T. Taminiau, D. Toyli, D. Lidar, D. Awschalom, R. Hanson, and V. Dobrovitski. Decoherence-protected quantum gates for a hybrid solid-state spin register. *Nature*, 484(7392):82–86, 2012.

[37] G. De Lange, Z. Wang, D. Riste, V. Dobrovitski, and R. Hanson. Universal dynamical decoupling of a single solid-state spin from a spin bath. *Science*, 330(6000):60–63, 2010.

[38] J. T. Barreiro, M. Müller, P. Schindler, D. Nigg, T. Monz, M. Chwalla, M. Hennrich, C. F. Roos, P. Zoller, and R. Blatt. An open-system quantum simulator with trapped ions. *Nature*, 470(7335):486–491, 2011.

[39] H. Krauter, C. A. Muschik, K. Jensen, W. Wasilewski, J. M. Petersen, J. I. Cirac, and E. S. Polzik. Entanglement generated by dissipation and steady state entanglement of two macroscopic objects. *Physical review letters*, 107(8):080503, 2011.

[40] A. Burrell, D. Szwer, S. Webster, and D. Lucas. Scalable simultaneous multiqubit readout with 99. 99% single-shot fidelity. *Physical Review A*, 81(4):040302, 2010.

[41] L. Jiang, J. Hodges, J. Maze, P. Maurer, J. Taylor, D. Cory, P. Hemmer, R. Walsworth, A. Yacoby, A. Zibrov, et al. Repetitive readout of a single electronic spin via quantum logic with nuclear spin ancillae. *Science*, 326(5950):267–272, 2009.

[42] L. Jiang, M. V. G. Dutt, E. Togan, L. Childress, P. Cappellaro, J. M. Taylor, and M. D. Lukin. Coherence of an optically illuminated single nuclear spin qubit. *Phys. Rev. Lett.*, 100:073001, Feb 2008.

[43] P. Neumann, N. Mizuochi, F. Rempp, P. Hemmer, H. Watanabe, S. Yamasaki, V. Jacques, T. Gaebel, F. Jelezko, and J. Wrachtrup. Multipartite entanglement among single spins in diamond. *science*, 320(5881):1326–1329, 2008.

[44] G. Waldherr, J. Beck, M. Steiner, P. Neumann, A. Gali, T. Frauenheim, F. Jelezko, and J. Wrachtrup. Dark states of single nitrogen-vacancy centers in diamond unraveled by single shot nmr. *Phys. Rev. Lett.*, 106:157601, Apr 2011.

[45] V. M. Acosta, E. Bauch, M. P. Ledbetter, A. Waxman, L.-S. Bouchard, and D. Budker. Temperature dependence of the nitrogen-vacancy magnetic resonance in diamond. *Phys. Rev. Lett.*, 104:070801, Feb 2010.

[46] N. Khaneja, R. Brockett, and S. J. Glaser. Time optimal control in spin systems. *Phys. Rev. A*, 63:032308, Feb 2001.

[47] C. J. Terblanche, E. C. Reynhardt, and J. A. van Wyk. C13 spin–lattice relaxation in natural diamond: Zeeman relaxation at 4.7 t and 300 k due to fixed paramagnetic nitrogen defects. *Solid state nuclear magnetic resonance*, 20(1):1–22, 2001.

[48] S. Wiesner. Conjugate coding. *ACM Sigact News*, 15(1):78–88, 1983.

[49] F. Pastawski, N. Y. Yao, L. Jiang, M. D. Lukin, and J. I. Cirac. Unforgeable noise-tolerant quantum tokens. *Proceedings of the National Academy of Sciences*, 109(40):16079–16082, 2012.

[50] D. M. Toyli, C. D. Weis, G. D. Fuchs, T. Schenkel, and D. D. Awschalom. Chip-scale nanofabrication of single spins and spin arrays in diamond. *Nano letters*, 10(8):3168–3172, 2010.

[51] P. Spinicelli, A. Dréau, L. Rondin, F. Silva, J. Achard, S. Xavier, S. Bansropun, T. Debuisschert, S. Pezzagna, J. Meijer, et al. Engineered arrays of nitrogen-vacancy color centers in diamond based on implantation of cn- molecules through nanoapertures. *New Journal of Physics*, 13(2):025014, 2011.

[52] P. Neumann, R. Kolesov, B. Naydenov, J. Beck, F. Rempp, M. Steiner, V. Jacques, G. Balasubramanian, M. Markham, D. Twitchen, et al. Quantum register based on coupled electron spins in a room-temperature solid. *Nature Physics*, 6(4):249–253, 2010.

[53] N. Y. Yao, L. Jiang, A. V. Gorshkov, P. C. Maurer, G. Giedke, J. I. Cirac, and M. D. Lukin. Scalable architecture for a room temperature solid-state quantum information processor. *Nature communications*, 3:800, 2012.

[54] Y. Yue and X. Wang. Nanoscale thermal probing. *Nano reviews*, 3, 2012.

[55] E. Lucchetta, J. Lee, L. Fu, N. Patel, and R. Ismagilov. Dynamics of drosophila embryonic patterning network perturbed in space and time using microfluidics. *Nature*, 434(7037):1134–1138, 2005.

[56] S. V. Kumar and P. A. Wigge. H2a. z-containing nucleosomes mediate the thermosensory response in arabidopsis. *Cell*, 140(1):136–147, 2010.

[57] V. M. Lauschke, C. D. Tsiairis, P. François, and A. Aulehla. Scaling of embryonic patterning based on phase-gradient encoding. *Nature*, 493(7430):101–105, 2012.

[58] Y. Kamei, M. Suzuki, K. Watanabe, K. Fujimori, T. Kawasaki, T. Deguchi, Y. Yoneda, T. Todo, S. Takagi, T. Funatsu, et al. Infrared laser–mediated gene induction in targeted single cells in vivo. *Nature methods*, 6(1):79–81, 2008.

[59] A. Schroeder, D. A. Heller, M. M. Winslow, J. E. Dahlman, G. W. Pratt, R. Langer, T. Jacks, and D. G. Anderson. Treating metastatic cancer with nanotechnology. *Nature Reviews Cancer*, 12(1):39–50, 2011.

[60] J.-H. Lee, J.-t. Jang, J.-s. Choi, S. H. Moon, S.-h. Noh, J.-w. Kim, J.-G. Kim, I.-S. Kim, K. I. Park, and J. Cheon. Exchange-coupled magnetic nanoparticles for efficient heat induction. *Nature Nanotechnology*, 6(7):418–422, 2011.

[61] D. P. O'Neal, L. R. Hirsch, N. J. Halas, J. D. Payne, and J. L. West. Photo-thermal tumor ablation in mice using near infrared-absorbing nanoparticles. *Cancer letters*, 209(2):171–176, 2004.

[62] T. Vreugdenburg, C. Willis, L. Mundy, and J. Hiller. A systematic review of elastography, electrical impedance scanning, and digital infrared thermography for breast cancer screening and diagnosis. *Breast Cancer Research and Treatment*, 137:665–676, 2013.

[63] A. Majumdar. Scanning thermal microscopy. *Annual review of materials science*, 29(1):505–585, 1999.

[64] S. H. Kim, J. Noh, M. K. Jeon, K. W. Kim, L. P. Lee, and S. I. Woo. Micro-raman thermometry for measuring the temperature distribution inside the microchannel of a polymerase chain reaction chip. *Journal of Micromechanics and Microengineering*, 16(3):526, 2006.

[65] J. Yang, H. Yang, and L. Lin. Quantum dot nano thermometers reveal heterogeneous local thermogenesis in living cells. *ACS nano*, 5(6):5067–5071, 2011.

[66] F. Vetrone, R. Naccache, A. Zamarrn, A. Juarranz de la Fuente, F. Sanz-Rodrguez, L. Martinez Maestro, E. Martn Rodriguez, D. Jaque, J. Garca Sol, and J. A. Capobianco. Temperature sensing using fluorescent nanothermometers. *ACS nano*, 4(6):3254–3258, 2010.

[67] K. Okabe, N. Inada, C. Gota, Y. Harada, T. Funatsu, and S. Uchiyama. Intracellular temperature mapping with a fluorescent polymeric thermometer and fluorescence lifetime imaging microscopy. *Nature communications*, 3:705, 2012.

[68] J. Donner, S. Thompson, M. Kreuzer, G. Baffou, and R. Quidant. Mapping intracellular temperature using green fluorescent protein. *Nano letters*, 12(4):2107–2111, 2012.

[69] V. Acosta, E. Bauch, M. Ledbetter, A. Waxman, L. Bouchard, and D. Budker. Temperature dependence of the nitrogen-vacancy magnetic resonance in diamond. *Physical Review Letters*, 104(7):70801, 2010.

[70] D. Toyli, D. Christle, A. Alkauskas, B. Buckley, C. Van de Walle, and D. Awschalom. Measurement and control of single nitrogen-vacancy center spins above 600 k. *Physical Review X*, 2(3):031001, 2012.

[71] X.-D. Chen, C.-H. Dong, F.-W. Sun, C.-L. Zou, J.-M. Cui, Z.-F. Han, and G.-C. Guo. Temperature dependent energy level shifts of nitrogen-vacancy centers in diamond. *Applied Physics Letters*, 99(16):161903–161903, 2011.

[72] J. Taylor, P. Cappellaro, L. Childress, L. Jiang, D. Budker, P. Hemmer, A. Yacoby, R. Walsworth, and M. Lukin. High-sensitivity diamond magnetometer with nanoscale resolution. *Nature Physics*, 4(10):810–816, 2008.

[73] G. Balasubramanian, I. Chan, R. Kolesov, M. Al-Hmoud, J. Tisler, C. Shin, C. Kim, A. Wojcik, P. R. Hemmer, A. Krueger, et al. Nanoscale imaging magnetometry with diamond spins under ambient conditions. *Nature*, 455(7213):648–651, 2008.

[74] J. Hodges and D. Englund. Time-keeping with electron spin states in diamond. *arXiv preprint arXiv:1109.3241*, 2011.

[75] A. K. Shalek, J. T. Robinson, E. S. Karp, J. S. Lee, D.-R. Ahn, M.-H. Yoon, A. Sutton, M. Jorgolli, R. S. Gertner, T. S. Gujral, et al. Vertical silicon nanowires as a universal platform for delivering biomolecules into living cells. *Proceedings of the National Academy of Sciences*, 107(5):1870–1875, 2010.

[76] A. K. Shalek et al. Nanowire-mediated delivery enables functional interrogation of primary immune cells: Application to the analysis of chronic lymphocytic leukemia. *Nano Letters*, 12(12):6498–6504, 2012.

[77] C. M. Pitsillides, E. K. Joe, X. Wei, R. Anderson, and C. P. Lin. Selective cell targeting with light-absorbing microparticles and nanoparticles. *Biophysical journal*, 84(6):4023–4032, 2003.

[78] P. Maurer, J. Maze, P. Stanwix, L. Jiang, A. Gorshkov, A. A. Zibrov, B. Harke, J. Hodges, A. S. Zibrov, A. Yacoby, et al. Far-field optical imaging and manipulation of individual spins with nanoscale resolution. *Nature Physics*, 6(11):912–918, 2010.

[79] G. Xu, S. M. Stevens, F. Kobiessy, H. Brown, S. McClung, M. S. Gold, and D. R. Borchelt. Identification of proteins sensitive to thermal stress in human neuroblastoma and glioma cell lines. *PloS one*, 7(11):e49021, 2012.

[80] C. Jin, Z. Li, R. Williams, K. Lee, and I. Park. Localized temperature and chemical reaction control in nanoscale space by nanowire array. *Nano letters*, 11(11):4818–4825, 2011.

[81] F. Helmchen and W. Denk. Deep tissue two-photon microscopy. *Nature methods*, 2(12):932–940, 2005.

[82] T.-L. Wee, Y.-K. Tzeng, C.-C. Han, H.-C. Chang, W. Fann, J.-H. Hsu, K.-M. Chen, and Y.-C. Yu. Two-photon excited fluorescence of nitrogen-vacancy centers in proton-irradiated type ib diamond. *The Journal of Physical Chemistry A*, 111(38):9379–9386, 2007.

[83] M. Tsoli, M. Moore, D. Burg, A. Painter, R. Taylor, S. H. Lockie, N. Turner, A. Warren, G. Cooney, B. Oldfield, et al. Activation of thermogenesis in brown adipose tissue and dysregulated lipid metabolism associated with cancer cachexia in mice. *Cancer Research*, 72(17):4372–4382, 2012.

[84] P. W. Anderson. Absence of diffusion in certain random lattices. *Physical review*, 109(5):1492, 1958.

[85] R. Weaver. Anderson localization of ultrasound. *Wave motion*, 12(2):129–142, 1990.

[86] D. S. Wiersma, P. Bartolini, A. Lagendijk, and R. Righini. Localization of light in a disordered medium. *Nature*, 390(6661):671–673, 1997.

[87] T. Schwartz, G. Bartal, S. Fishman, and M. Segev. Transport and anderson localization in disordered two-dimensional photonic lattices. *Nature*, 446(7131):52–55, 2007.

[88] G. Roati, C. DErrico, L. Fallani, M. Fattori, C. Fort, M. Zaccanti, G. Modugno, M. Modugno, and M. Inguscio. Anderson localization of a non-interacting bose–einstein condensate. *Nature*, 453(7197):895–898, 2008.

[89] J. Billy, V. Josse, Z. Zuo, A. Bernard, B. Hambrecht, P. Lugan, D. Clément, L. Sanchez-Palencia, P. Bouyer, and A. Aspect. Direct observation of anderson localization of matter waves in a controlled disorder. *Nature*, 453(7197):891–894, 2008.

[90] D. Basko, I. Aleiner, and B. Altshuler. Metal–insulator transition in a weakly interacting many-electron system with localized single-particle states. *Annals of physics*, 321(5):1126–1205, 2006.

[91] V. Oganesyan and D. A. Huse. Localization of interacting fermions at high temperature. *Physical review b*, 75(15):155111, 2007.

[92] A. Pal and D. A. Huse. Many-body localization phase transition. *Physical review b*, 82(17):174411, 2010.

[93] M. Schreiber, S. S. Hodgman, P. Bordia, H. P. Lüschen, M. H. Fischer, R. Vosk, E. Altman, U. Schneider, and I. Bloch. Observation of many-body localization of interacting fermions in a quasirandom optical lattice. *Science*, 349(6250):842–845, 2015.

[94] J.-y. Choi, S. Hild, J. Zeiher, P. Schauß, A. Rubio-Abadal, T. Yefsah, V. Khemani, D. A. Huse, I. Bloch, and C. Gross. Exploring the many-body localization transition in two dimensions. *arXiv preprint arXiv:1604.04178*, 2016.

[95] N. Y. Yao, C. R. Laumann, S. Gopalakrishnan, M. Knap, M. Mueller, E. A. Demler, and M. D. Lukin. Many-body localization in dipolar systems. *Physical review letters*, 113(24):243002, 2014.

[96] L. Levitov. Absence of localization of vibrational modes due to dipole-dipole interaction. *EPL (Europhysics Letters)*, 9(1):83, 1989.

[97] L. Levitov. Delocalization of vibrational modes caused by electric dipole interaction. *Physical review letters*, 64(5):547, 1990.

[98] A. D. Mirlin, Y. V. Fyodorov, F.-M. Dittes, J. Quezada, and T. H. Seligman. Transition from localized to extended eigenstates in the ensemble of power-law random banded matrices. *Physical Review E*, 54(4):3221, 1996.

[99] D. Parshin and H. Schober. Multifractal structure of eigenstates in the anderson model with long-range off-diagonal disorder. *Physical Review B*, 57(17):10232, 1998.

[100] L. Levitov. Critical hamiltonians with long range hopping. *arXiv preprint cond-mat/9908178*, 1999.

[101] V. Kravtsov, O. Yevtushenko, P. Snajberk, and E. Cuevas. Lévy flights and multifractality in quantum critical diffusion and in classical random walks on fractals. *Physical Review E*, 86(2):021136, 2012.

[102] Materials and methods are available as supporting material on science online.

[103] S. Hartmann and E. Hahn. Nuclear double resonance in the rotating frame. *Physical Review*, 128(5):2042, 1962.

[104] C. Belthangady, N. Bar-Gill, L. M. Pham, K. Arai, D. Le Sage, P. Cappellaro, and R. L. Walsworth. Dressed-state resonant coupling between bright and dark spins in diamond. *Physical review letters*, 110(15):157601, 2013.

[105] P. London, J. Scheuer, J.-M. Cai, I. Schwarz, A. Retzker, M. Plenio, M. Katagiri, T. Teraji, S. Koizumi, J. Isoya, et al. Detecting and polarizing nuclear spins with double resonance on a single electron spin. *Physical review letters*, 111(6):067601, 2013.

[106] Manuscript in preparation.

[107] J. Cardellino, N. Scozzaro, M. Herman, A. J. Berger, C. Zhang, K. C. Fong, C. Jayaprakash, D. V. Pelekhov, and P. C. Hammel. The effect of spin transport on spin lifetime in nanoscale systems. *Nature nanotechnology*, 9(5):343–347, 2014.

[108] M. J. Burek, N. P. de Leon, B. J. Shields, B. J. Hausmann, Y. Chu, Q. Quan, A. S. Zibrov, H. Park, M. D. Lukin, and M. Loncar. Free-standing mechanical and photonic nanostructures in single-crystal diamond. *Nano letters*, 12(12):6084–6089, 2012.

[109] M.-A. Félix and C. Braendle. The natural history of caenorhabditis elegans. *Current Biology*, 20(22):R965–R969, 2010.

[110] N. Mohan, C.-S. Chen, H.-H. Hsieh, Y.-C. Wu, and H.-C. Chang. In vivo imaging and toxicity assessments of fluorescent nanodiamonds in caenorhabditis elegans. *Nano letters*, 10(9):3692–3699, 2010.

[111] G. Fuchs, V. Dobrovitski, D. Toyli, F. Heremans, and D. Awschalom. Gigahertz dynamics of a strongly driven single quantum spin. *Science*, 326(5959):1520–1522, 2009.

[112] H. Lee, E. Sun, D. Ham, and R. Weissleder. Chip–nmr biosensor for detection and molecular analysis of cells. *Nature medicine*, 14(8):869–874, 2008.

[113] V. Jacques, P. Neumann, J. Beck, M. Markham, D. Twitchen, J. Meijer, F. Kaiser, G. Balasubramanian, F. Jelezko, and J. Wrachtrup. Dynamic polarization of single nuclear spins by optical pumping of nitrogen-vacancy color centers in diamond at room temperature. *Physical review letters*, 102(5):057403, 2009.

[114] R. Schoelkopf, A. Clerk, S. Girvin, K. Lehnert, and M. Devoret. Qubits as spectrometers of quantum noise. In *Quantum noise in mesoscopic physics*, pages 175–203. Springer, 2003.

[115] W. M. Itano, D. J. Heinzen, J. Bollinger, and D. Wineland. Quantum zeno effect. *Physical Review A*, 41(5):2295, 1990.

[116] N. B. Manson, J. P. Harrison, and M. J. Sellars. Nitrogen-vacancy center in diamond: Model of the electronic structure and associated dynamics. *Phys. Rev. B*, 74:104303, Sep 2006.

[117] A. Gali, M. Fyta, and E. Kaxiras. Ab initio supercell calculations on nitrogen-vacancy center in diamond: Electronic structure and hyperfine tensors. *Phys. Rev. B*, 77:155206, Apr 2008.

[118] M. Mehring. High resolution nmr in solids, 2008.

[119] M. A. Nielsen and I. L. Chuang. *Quantum computation and quantum information*. Cambridge university press, 2010.

[120] J. L. O'Brien, G. Pryde, A. Gilchrist, D. James, N. Langford, T. Ralph, and A. White. Quantum process tomography of a controlled-not gate. *Physical review letters*, 93(8):080502, 2004.

[121] D. F. James, P. G. Kwiat, W. J. Munro, and A. G. White. Measurement of qubits. *Physical Review A*, 64(5):052312, 2001.

[122] S. Haroche and J.-M. Raimond. *Exploring the quantum: atoms, cavities, and photons (oxford graduate texts)*. Oxford University Press, USA, 2013.

[123] M. A. Nielsen. A simple formula for the average gate fidelity of a quantum dynamical operation. *Physics Letters A*, 303(4):249–252, 2002.

[124] A. Akimov, A. Mukherjee, C. Yu, D. Chang, A. Zibrov, P. Hemmer, H. Park, and M. Lukin. Generation of single optical plasmons in metallic nanowires coupled to quantum dots. *Nature*, 450(7168):402–406, 2007.

[125] E. Van Oort and M. Glasbeek. Electric-field-induced modulation of spin echoes of nv centers in diamond. *Chemical Physics Letters*, 168(6):529–532, 1990.

[126] C. S. Shin, M. C. Butler, H.-J. Wang, C. E. Avalos, S. J. Seltzer, R.-B. Liu, A. Pines, and V. S. Bajaj. Optically detected nuclear quadrupolar interaction of n 14 in nitrogen-vacancy centers in diamond. *Physical Review B*, 89(20):205202, 2014.

[127] C. Kittel and E. Abrahams. Dipolar broadening of magnetic resonance lines in magnetically diluted crystals. *Physical Review*, 90(2):238, 1953.

[128] J. Van Vleck. The dipolar broadening of magnetic resonance lines in crystals. *Physical Review*, 74(9):1168, 1948.